

Quantum imaging and polarimetry with two-color photon pairs



**FRIEDRICH-SCHILLER-
UNIVERSITÄT
JENA**

Dissertation
zur Erlangung des akademischen Grades
doctor rerum naturalium (Dr. rer. nat.)

**vorgelegt dem Rat der Physikalisch-Astronomischen Fakultät
der Friedrich-Schiller-Universität Jena**

von M. Sc. Andres Ricardo Vega Perez
geboren am 03.02.1989 in Quito, Ecuador

1. Gutachter: PD Dr. Frank Setzpfandt
2. Gutachter: Prof. Dr. Milena D'Angelo
3. Gutachter: Prof. Dr. Georg von Freymann

Tag der Disputation: 09.05.2023

Contents

1. Introduction	3
1.1. Quantum imaging and sensing: beginnings and state of the art	3
1.2. Aim and structure of this thesis	10
1.3. Collaborations	11
2. Basics of the two-photon quantum state	12
2.1. Electric field operator	13
2.2. Spontaneous parametric down-conversion	15
2.3. Abstract and publication	22
3. Fundamental resolution limit of two-color quantum imaging	23
3.1. Quantum imaging with undetected photons	23
3.2. Quantum ghost imaging	41
3.3. Abstract and publication	46
4. Lensless quantum ghost imaging	48
4.1. Quantum ghost diffraction	49
4.2. Pinhole quantum ghost imaging	54
4.3. Abstract and publication	66
5. Metasurface-assisted quantum ghost polarimetry	68
5.1. Quantum ghost polarimetry	68
5.2. Discrimination of polarization-sensitive objects	76
5.3. Metasurface as a versatile platform	79
5.4. Entanglement versus classical correlations	84
5.5. Abstract and publication	90
6. Summary and outlook	91
A. References	96
B. List of own contributions	113
C. List of abbreviations	115
D. Acknowledgement	116

E. Zusammenfassung	117
F. Ehrenwörtliche Erklärung	118

1. Introduction

1.1. Quantum imaging and sensing: beginnings and state of the art

Basic principles of quantum mechanics, such as entanglement, lie at the heart of emerging quantum technologies. The purpose of advancing these novel quantum techniques is to find improved solutions to particular tasks, which outperform the performance of state-of-the-art technology based solely on classical physics. The thought experiment of Einstein, Podolsky and Rosen [1] discussed the essence of an entangled state [2]. Particles of a system are said to be entangled when they are generated together or interacted with one another, and their states cannot be independently described even if the particles are later spatially separated. In other words, entangled particles share quantum correlations. Importantly, such correlations are exploited within the field of quantum optics to achieve, for example, imaging and sensing with entangled photons, as will be discussed at length in this thesis.

Photon pairs that are entangled, e.g., in wavelength, polarization, and/or transverse momentum, have been used to experimentally test fundamental theoretical predictions of quantum mechanics. The experimental pioneers of quantum technologies and quantum information theory, Aspect [3], Clauser [4], and Zeilinger [5], received the Nobel Prize in Physics 2022 for their extensive work using entangled photons. A pair of entangled photons can be obtained from the process of spontaneous parametric down-conversion (SPDC), as was first experimentally shown by Burnham et al. using coincidence-counting measurements [6]. A few years later, Hong and Mandel put forward a general theory of down-converted fields [7], which will serve as the basis for investigating SPDC in this thesis¹.

Several entanglement-based quantum effects were demonstrated using photon pairs, including the quantum eraser, quantum teleportation, and entanglement swapping. The quantum eraser was proposed by Scully et al. [10] and was later demonstrated

¹ Processes like spontaneous Raman scattering in atomic systems [8] and spontaneous four-wave mixing [9] can also be used to generate entangled photon pairs; however, only pairs produced by SPDC are discussed in this thesis.

by Kwiat et al. [11], Kim et al. [12] and Walborn et al. [13]. In this experiment, a double slit is illuminated with single photons, where if it is possible to know through which slit a photon passes, then the measured pattern does not show any interference. In contrast, if the slit through which the photon passes is unknown, then an interference pattern appears. Consequently, ‘erasing’ the information of the path taken by the photon results in the photon interfering with itself. Furthermore, quantum teleportation is another prominent quantum effect that was first proposed by Bennet et al. [14] and then experimentally realized by Boschi et al. [15] and Bouwmeester et al. [16]. Here, the information of a state can be transferred from a sender to a distant receiver by means of an entangled state. Additionally, entanglement swapping is a quantum effect put forward by Żukowski et al. [17] and later experimentally shown in Refs. [18–22], where two photons from independent photon-pair sources become entangled.

Quantum light can be used to test fundamental quantum effects, as just mentioned, but has also become the basis of emerging applications such as quantum computing [23], quantum communication [24] and quantum metrology [25–30]. Several quantum-enhanced imaging [31] and spectroscopy [32] protocols have been proposed in the last few years. Some relevant related technologies will be mentioned next. Quantum-enhanced imaging schemes with photon pairs have been demonstrated, as is the case of differential interference contrast microscopy with a NOON state [33] of $N = 2$ [34], subshot-noise wide-field microscopy [35], and scanning heralded microscopy for fast and single-mode imaging [36], quantum-secured imaging [37], and quantum plenoptic imaging [38–40]. It is also worth mentioning that, beyond the use of only photon pairs, there is quantum-enhanced coherent Raman microscopy [41], quantum-enhanced noise radar [42] and Lidar [43], resolution-enhanced quantum imaging using multiphoton interference [44, 45], single-photon emitters [46, 47], and incoherent light [48, 49]. Additionally, the subfield of quantum lithography aims to deliver a resolution enhancement of $\lambda/(2N)$, with N being the entangled photons that pass through the mask [50–53]. There have also been quantum-enhanced applications beyond imaging, as is the case with spectroscopy. Spectroscopy with two-color photon pairs has been implemented in several proof-of-principle experiments, e.g., spectroscopy at a long wavelength like infrared or terahertz, while measuring shorter-wavelength photons in, e.g., the visible range [54–59]. There have been reports on absorption spectroscopy at the quantum limit using single photons [60] and quantum advantage on absorption [61].

Numerous quantum technologies have been made possible due to the advancement in the design and fabrication of photon-pair sources and also due to the progress of

engineering more efficient single-photon detectors. The first experiments to test quantum effects were performed using bulk nonlinear crystals as sources of photon pairs with degenerate wavelengths. Among the most common materials used for SPDC are KDP (potassium dihydrogen phosphate) [62–66], BBO (beta barium borate) [67–72], KTP (potassium titanyl phosphate) [73–77], and LiNbO_3 (lithium niobate) [78–81]. Quantum imaging and sensing can benefit from sources of photon pairs with highly non-degenerate wavelengths, where the choice of a material’s transmission, linear and nonlinear response are important when generating photon pairs with wavelengths that are very far apart; see, e.g., Ref. [82]. Moreover, the geometry of a photon-pair source greatly influences the properties of pair generation. In recent years, materials such as lithium niobate have been used for the first time to fabricate thin sources [83, 84]. Integrated optical and quantum optical devices can be relevant for compact quantum applications, for example, in the form of waveguides [81, 85] or metasurfaces [86–88].

In this thesis, two quantum technologies that lie in the intersection of fundamental and applied physics and use entangled photons generated by SPDC will be thoroughly examined: quantum ghost imaging/polarimetry and quantum imaging with undetected photons.

1.1.1. Quantum ghost imaging

In 1995, Strekalov et al. and Pittman et al., from the group led by Shih, introduced two pioneering works: quantum ghost diffraction (QGD) [89] and quantum ghost imaging (QGI) [90], respectively. The design of the schemes was influenced by the work of Klyshko [91]. A QGI scheme, illustrated in Fig. 1.1, uses a source of correlated photon pairs; each pair is composed of the commonly called signal and idler photons that share both momentum and position correlations. After creation, the two photons are separated into two different paths, and only one of them interacts with an object, e.g., the idler photon. Then, this idler photon is measured by a detector without spatial resolution commonly called ‘bucket’ detector, which simply collects all incoming photons, whereas the signal photon that never interacts with the object is measured by another detector with spatial resolution. Although none of the detectors alone can recover the image of the object, remarkably, the image can be recovered by correlating the two measurements using coincidence measurements [92, 93]. In QGD, the diffraction pattern of the object can be obtained in a similar manner, with one of the differences being that it requires a point-like detector instead of a bucket detector.

QGI and QGD inspired researchers at the fundamental level, e.g., by using both

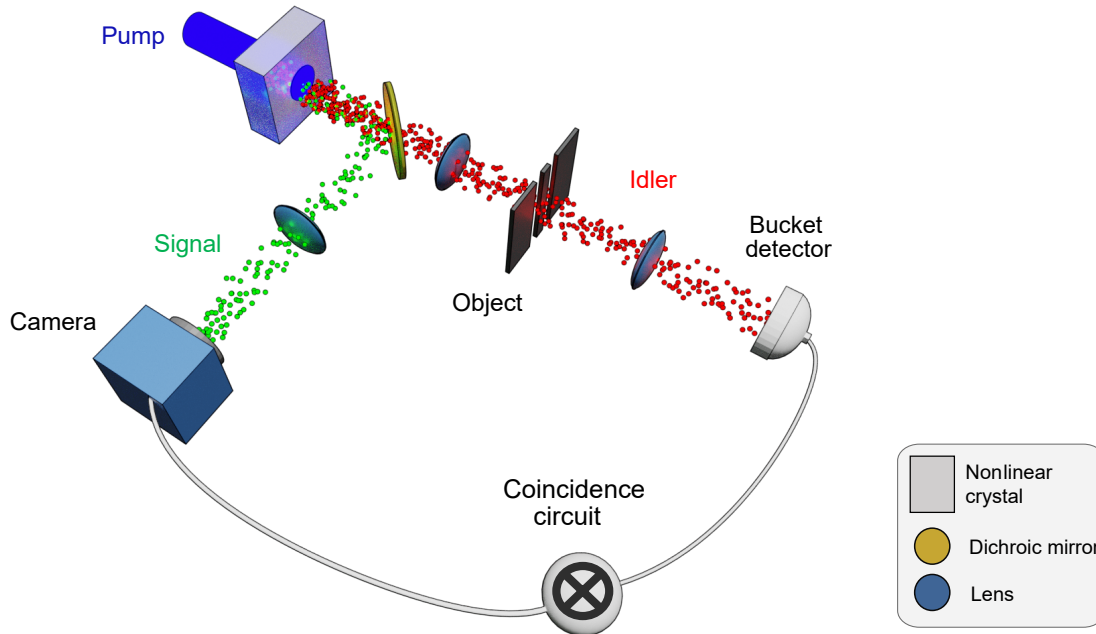


Figure 1.1. Sketch of a quantum ghost imaging (QGI) scheme with two-color photon pairs. The idler photons with lower energy illuminate the sample and are measured by a spatially non-resolving detector, while the non-interacting signal photons are measured by a camera. The image of the object can be retrieved from the coincidence measurements between signal and idler photons.

schemes to quantify the degree of entanglement between signal and idler photons [94], but more importantly, by triggering a long discussion [95–97] on whether they worked only due to entanglement. This discussion was closed a few years after QGI and QGD were proposed, as it was proven that a ghost imaging scheme that uses light with classical correlations mimics most of the characteristics of entangled photons [98–104]. The main difference between the quantum and the classical scheme resides in the signal-to-noise ratio (SNR) [105–107]. The thermal (classical) ghost image always resides on top of a larger background, where the fluctuations in this background constitute an intrinsic noise source. In contrast, there is a smaller intrinsic background when a source of quantum light is used to generate a quantum ghost image.

However, the QGI technique offers tremendous potential for applications over its classical counterpart, especially for biosensing, where sensitive samples prone to radiation damage are probed. That is, QGI has two main practical advantages: First, as already mentioned, very low numbers of photons can be used to illuminate the sensitive sample and obtain a better SNR compared to imaging with classical light. Second, QGI with two-color photon pairs can overcome limitations due to inaccessible wavelength ranges for illumination and detection [108–110]. A sensitive sample can be illuminated with a low-energetic photon, while a resolving detector measures the more energetic photon in a wavelength range where sensors are highly efficient, e.g., in the visible range.

The technology to transform QGI into an applicable device is still in its infancy, but is advancing at a fast pace. Efficient single-photon detectors, namely CCD cameras [111, 112], single-photon-avalanche-diode (SPAD) arrays [113–118] and superconducting nanowire detectors [119], and bright sources of highly entangled photons, as mentioned before, are currently under study and development.

Literature gap: It is of considerable practical interest to develop lensless ghost imaging schemes, as high-quality lenses are less available in wavelength ranges where the signal and idler can be generated [120], e.g., in the terahertz range, which is of interest for biology, medicine, and material science [121–124]. A quantum ghost image can be formed using lenses in the paths of the down-converted photons [90, 106, 107], as shown in Fig. 1.1. Pittman et al. also demonstrated an alternative to achieve imaging without any lenses in the paths of the signal and idler photons, namely by using a pump beam with a curved phase-front inside the nonlinear crystal [125]. However, the lensless configuration mentioned in [125] exploits *only* the shape of the pump phase front. Then, a natural question arises: Can novel lensless QGI schemes emerge from engineering other degrees of freedom of the scheme, e.g., the transverse profile of the pump beam? The answer to this question has not yet been thoroughly addressed in the literature.

1.1.2. Quantum ghost polarimetry

Optical sensing of polarization properties provides a wealth of information that is otherwise hidden, with applications ranging from microscopy [126] to monitoring from satellites [127]. Although polarization manipulation and measurement are conveniently performed using bulk optical elements [128], nanostructured metasurfaces allow more flexible parallel polarization transformations for single-shot measurements [129], real-time imaging with a camera [130], quantum light manipulation, and characterization [87, 131–134]. Fundamental and applied interest in polarization detection at low-light illumination and across broad spectral regions, for example, for biosensing, motivated the development of ghost polarimetry, which was first proposed from a classical perspective [135]. However, there remains a fundamental limitation of the proposed classical ghost polarimetry approaches due to the need for multiple reconfigurable elements such as rotating waveplates [136–143].

Literature gap: A comprehensive treatment of quantum ghost polarimetry (QGP) is lacking from the literature. The polarization entanglement between signal and idler photons is used in QGP, which is a simpler form of a scheme compared to QGI, as two polarization modes are used instead of a continuum of position/momentum modes. QGP draws on the underlying principle originally developed for QGI, where the pho-

tons passing through an object are registered with a simple non-resolving detector [90, 144], while their quantum pairs can be conveniently measured at a different wavelength selected for efficient high-resolution detection [108–110]. Then a polarization-sensitive object can be characterized by multiple coincidence measurements [145]. Moreover, the unique capabilities of polarization control with metasurfaces towards potential single-shot quantum ghost configurations have remained largely untapped; some metasurfaces have been used in this context only for hologram generation [146]. Therefore, an extensive treatment of QGP that benefits from metasurfaces is of great interest to the community.

1.1.3. Quantum imaging with undetected photons

The first experimental demonstration of quantum imaging with undetected photons (QIUP) was performed by Lemos et al. in 2014 [147, 148]. A sketch of the scheme is shown in Fig. 1.2. QIUP relies on the quantum effect of induced coherence without induced emission [149, 150], which was demonstrated using a setup composed of two nonlinear crystals in the low-gain regime, here named A and B, producing down-converted photon pairs, which are superimposed. Importantly, only the idler photons of source A interact with the object, and then the path of these idler photons is aligned with the path of the idler photons of source B. At the same time, the signal photons do not interact with the object but interfere at a beamsplitter. One of the outputs of this beamsplitter is measured by a single-photon detector. The major result of the scheme is that the *sole* measurement of the non-interacting signal photons carries information of the transmission of the object, namely, the image of the object probed by idler photons can be obtained measuring only signal photons. Importantly, this utmost unintuitive effect relies on the alignment of the idler photons. The sole overlap of idler modes, without the necessity of the idlers of source A inducing photon emission on source B, introduces interference to the state of the system, since it is no longer possible to distinguish which source generated the idler photon coming out of crystal B. Additionally, since the signal photons are measured after the beamsplitter, the source of a signal photon cannot be distinguished.

The most prominent advantage of QIUP over QGI is the fact that coincidence measurements are not required to retrieve an image. Thus, if two-color photon pairs are used (one less energetic photon to probe the object and its pair in the visible range that is measured), then only one single-photon detector with high efficiency in the visible range is needed. Since the image of the object is directly obtained in the signal photons, the less energetic probing idler photons can remain undetected. This poses a major practical advantage, which has motivated several works, e.g., Refs. [151–

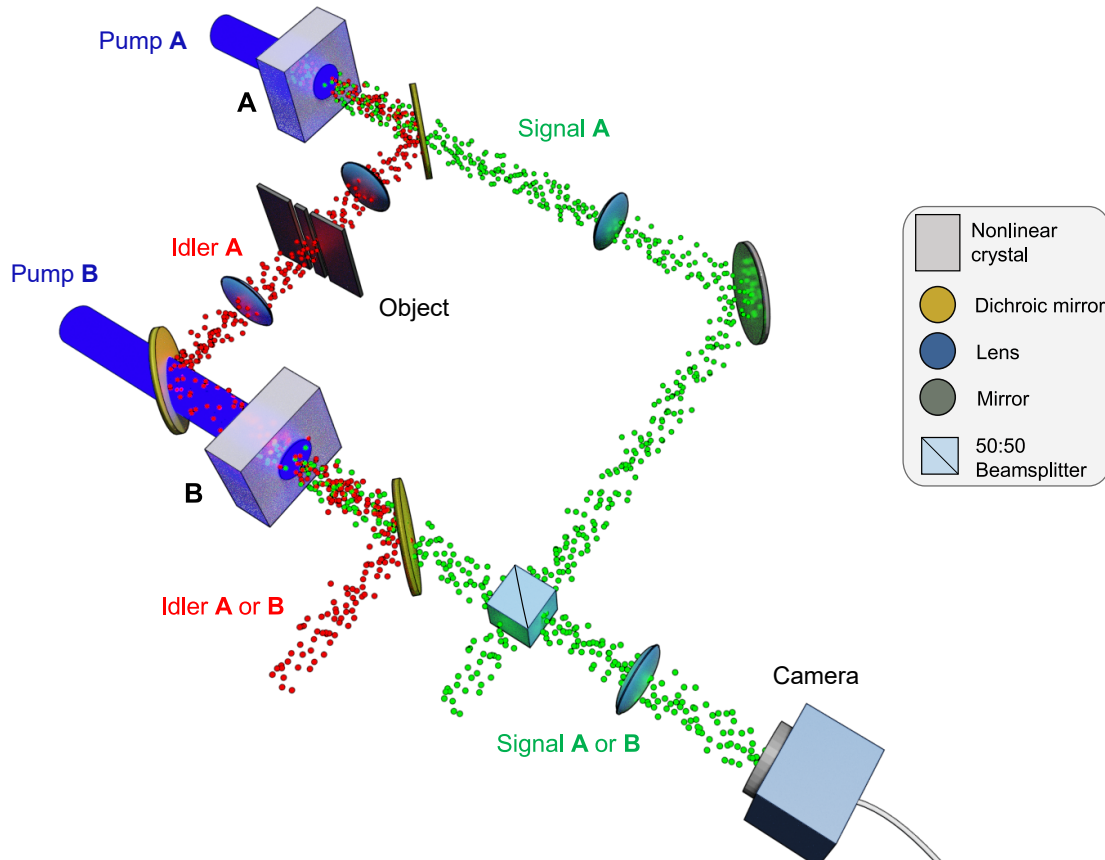


Figure 1.2. Sketch of quantum imaging with undetected photons (QIUP) with two-color photon pairs. The scheme consists of two sources of photon pairs; the idlers of source A interact with the object and are later superimposed with the idlers of source B. Signal photons also interfere and are measured by a camera. QIUP allows us to retrieve the image of the object, illuminated by idler photons, by measuring only signal photons.

155], since there is no need for a highly efficient single-photon detector for long wavelengths, as is the case of QGI.

Literature gap: It is well known that the fundamental resolution of a diffraction-limited classical imaging scheme depends on the wavelength λ of the particle that interacts with the object [156–158]. Assuming that the optical elements have a numerical aperture $NA=1$, the resolution is $\approx \lambda/2$. For that reason, electron microscopy delivers higher resolution than a conventional light microscope using visible light [159]. As mentioned before, quantum imaging protocols can be implemented with signal and idler photons of different wavelengths, so it is natural to ask oneself: Which wavelength defines the fundamental resolution of QIUP and QGI? Although several works have discussed the resolution of quantum imaging [108, 151, 160–165], they have treated this question only within the paraxial regime. This fits very well with most experiments that rely on commercially available nonlinear crystals, whose typical thickness is much larger than the wavelengths of the down-converted photons.

These thick crystals generate signal and idler photons only within a small range of transverse momenta. However, the recent advent of thinner nonlinear materials as photon-pair sources [83, 84, 86] opens up the possibility of having photons in a momentum range beyond the paraxial regime. These ultra-thin crystals can have a thickness smaller than the wavelengths of signal and idler. The fundamental resolution limit of QIUP and QGI based on two-color photon pairs generated beyond the paraxial regime remains an open problem.

1.2. Aim and structure of this thesis

1.2.1. Aim

The general aim of this thesis is to advance the state-of-the-art knowledge of quantum imaging and polarimetry with two-color photon pairs by bridging three gaps in the literature. These have already been mentioned above and will be addressed in the following order. First, since the beginning of QGI and QIUP, a formal proof of their fundamental transverse resolution limit is lacking from the theory (see sections 1.1.1 and 1.1.3). Second, the influence of the pump beam profile used in QGI has not yet been exhaustively studied in the literature (see section 1.1.1). Third, even though QGI was initiated almost 30 years ago, a thorough theoretical development of QGP is missing (see section 1.1.2).

1.2.2. Structure

The quantum state of the photon pairs lies at the heart of the quantum imaging and polarimetry schemes presented in this thesis. Therefore, we start this thesis by presenting a mathematical derivation of the two-photon quantum state in chapter 2. In that chapter, the electric field operator is derived and then used to describe pair generation by the SPDC process. At the end of the chapter, the two-photon quantum state is simplified for schemes presented in subsequent chapters, namely, a photon-pair source with transverse-momentum entanglement and a source with exclusively polarization entanglement.

The fundamental resolution of QIUP and QGI with two-color photon pairs is presented in chapter 3 using the two-photon state with transverse-momentum entanglement derived in the previous chapter. In chapter 3, the dependence of the transverse resolution on the wavelengths of the signal and idler photons is discussed by deriving a more general description of the resolution suitable in the non-paraxial regime. The

chapter begins with the QIUP scheme based on position correlations; then its fundamental resolution limit is derived. Moreover, a similar analysis of the resolution is carried out for QGI based on position correlations.

Chapter 4 discusses a novel lensless imaging scheme that we named ‘pinhole quantum ghost imaging’. Chapter 4 begins with the QGD scheme, which was already briefly mentioned in this chapter, and then we explain how it can be modified to produce ghost images avoiding the need of lenses in the down-converted arms. At the end of the chapter, the resolution within the paraxial regime of the proposed scheme is derived.

Lastly, chapter 5 contains our proposal of a QGP scheme, which uses a two-photon source with polarization entanglement. The discussion in this chapter concentrates on the discrimination of polarization-sensitive objects. In addition, we use this scheme to discuss the role of entanglement at the end of the chapter.

1.3. Collaborations

The following work was developed by me, Andres Ricardo Vega Perez, under the direct supervision of Dr. Frank Setzpfandt in the Nano & Quantum optics group of Prof. Thomas Pertsch (Institute of Applied Physics, Abbe Center of Photonics, Friedrich Schiller University Jena). However, it is important to mention that the experiments regarding QIUP of Marta Gilaberte Basset and Jorge Fuenzalida from the group of Prof. Markus Gräfe (Fraunhofer IOF - TU Darmstadt) sparked our work to derive the fundamental resolution limit of this scheme discussed in chapter 3. Furthermore, the non-paraxial derivation of the two-photon state, presented within chapter 2, was done by my colleague Elkin A. Santos and it is presented in this thesis since our joint contribution led to the resolution analysis in chapter 3. Last but not least, the initiative to use metasurfaces within the QGP scheme, shown in chapter 5, was from Prof. Andrey Sukhorukov (Nonlinear and quantum photonics group, Australian National University).

2. Basics of the two-photon quantum state

The backbone of the imaging and polarimetry schemes investigated in this thesis are photon pairs produced from the process of spontaneous parametric down-conversion (SPDC). Photon pairs obtained from SPDC using birefringent crystals with high second-order nonlinearity have been widely used to test quantum experiments, as mentioned in chapter 1. In the SPDC process, pump photons impinge onto a nonlinear crystal, and only a few of these photons are spontaneously down-converted into pairs of photons of lower energy, called signal and idler; see Fig. 2.1. The nature of the down-conversion process is probabilistic and most of the photons of the pump do not produce photon pairs and are simply transmitted through the crystal. The (unnormalized) output state of the process is [7, 166, 167]

$$|\psi\rangle_{\text{SPDC}} = |0, 0\rangle + |\psi\rangle, \quad (2.1)$$

where $|0, 0\rangle$ is the vacuum state and $|\psi\rangle$, with a much lower probability, is the two-photon state that contains information on the produced signal and idler. Most significantly, the produced down-converted photons show entanglement because of conservation of energy and momentum.

It is important to mention that an increased probability of producing states with a

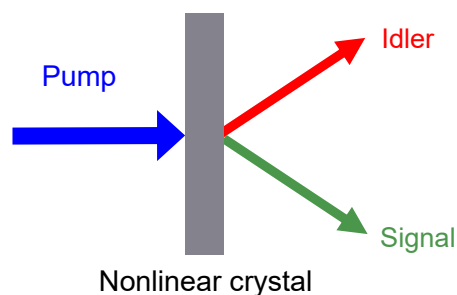


Figure 2.1. Schematic of the spontaneous parametric down-conversion process, where a pump beam impinges a nonlinear crystal producing a pair of photons with lower energy called signal and idler.

large number of photons per mode can be achieved by strongly pumping a nonlinear crystal [168, 169]. Such high-gain parametric down-conversion results in multiphoton states; however, in this thesis we only consider the low-gain regime where states with only two photons per mode are produced.

In this chapter, a theoretical framework for the description of SPDC is presented, which is needed to model the photon-pair sources used in quantum imaging and polarimetry.

2.1. Electric field operator

We begin by considering the electric field operator to later model the signal and idler photons within SPDC. The positive-frequency part of the electric field operator is given by [170]

$$\hat{\mathbf{E}}^{(+)}(\mathbf{r}, t) = \frac{i}{(2\pi)^{3/2}} \sum_l \int d\mathbf{k} \left(\frac{\hbar\omega}{2\epsilon_0} \right)^{1/2} \hat{a}(\mathbf{k}, l) \mathbf{e}(\mathbf{k}, l) \exp[i(\mathbf{k} \cdot \mathbf{r} - \omega t)], \quad (2.2)$$

where \mathbf{k} is the wave-vector and its integral is $\int d\mathbf{k} = \int_{-\infty}^{+\infty} dk_z \int_{-\infty}^{+\infty} dk_y \int_{-\infty}^{+\infty} dk_x$. Additionally, $l \in \{1, 2\}$ models the two possible polarizations perpendicular to each wave-vector \mathbf{k} , \mathbf{e} is the unit-vector of the polarization l of the wave-vector \mathbf{k} , $\omega = c|\mathbf{k}| = c\sqrt{k_x^2 + k_y^2 + k_z^2}$ is the angular frequency, ϵ_0 is the vacuum permittivity, c is the speed of light in vacuum, \hbar is the reduced Planck's constant, and \hat{a} is the annihilation operator. The commutation relations of the annihilation and creation operators are

$$[\hat{a}(\mathbf{k}, l), \hat{a}^\dagger(\mathbf{k}', l')] = \delta(\mathbf{k} - \mathbf{k}') \delta_{ll'}. \quad (2.3)$$

The process of pair generation relies on conservation of energy, therefore, it is useful to make frequency dependencies explicit in our description. To this end, the z-component of the wave-vector k_z is written in terms of ω , since the energy of a photon equals $\hbar\omega$, leading to $k_z = +\sqrt{(\omega/c)^2 - k_x^2 - k_y^2}$. Notice that we consider only the positive k_z which is relevant for the schemes of the next chapters, as photons propagate only in the forward direction. Moreover, its corresponding integral is then limited to $\int_0^{+\infty} dk_z$. Consequently, dk_z can be written as

$$dk_z = d \left[\left(\frac{\omega}{c} \right)^2 - k_x^2 - k_y^2 \right]^{1/2} = \frac{\omega}{c^2 k_z} d\omega, \quad (2.4)$$

2 Basics of the two-photon quantum state

and the integral then has the following form

$$\int d\mathbf{k} \longrightarrow \int_0^{+\infty} d\omega \int_{-\omega/c}^{+\omega/c} dk_x \int_{-\sqrt{\frac{\omega^2}{c^2}-k_x^2}}^{+\sqrt{\frac{\omega^2}{c^2}-k_x^2}} dk_y \frac{\omega}{c^2 k_z}. \quad (2.5)$$

Importantly, the integrals k_x, k_y are restricted to the region

$$k_x^2 + k_y^2 \leq \frac{\omega^2}{c^2}, \quad (2.6)$$

since we deal only with propagating waves. This means that the near-field effects produced by evanescent waves are not taken into account. Moreover, the change of variable affects also the commutation relations,

$$\begin{aligned} [\hat{a}(\mathbf{k}, l), \hat{a}^\dagger(\mathbf{k}', l')] &= \delta(k_x - k'_x) \delta(k_y - k'_y) \delta(k_z - k'_z) \delta_{ll'} \\ &= \delta(k_x - k'_x) \delta(k_y - k'_y) \delta(\omega - \omega') \delta_{ll'} \frac{c^2 k_z}{\omega}. \end{aligned} \quad (2.7)$$

The annihilation operator can be newly defined as

$$\hat{a}(k_x, k_y, \omega, l) = \left(\frac{\omega}{c^2 k_z} \right)^{1/2} \hat{a}(k_x, k_y, k_z, l), \quad (2.8)$$

which results in the commutation relations

$$[\hat{a}(k_x, k_y, \omega, l), \hat{a}^\dagger(k'_x, k'_y, \omega', l')] = \delta(k_x - k'_x) \delta(k_y - k'_y) \delta(\omega - \omega') \delta_{ll'}. \quad (2.9)$$

For simplicity, without compromising the underlying physics of SPDC, we simplify the model to only one transverse dimension k_x . In this simplification, we take into account only photons with $k_y \approx 0$, therefore, the range of k_x will be given by $k_x^2 \leq \omega^2/c^2$, as defined by the range of propagating waves of Eq. (2.6). The variable k_x will be denoted as q from now on and x will be its corresponding transverse position dimension. Following the treatment of Ref. [170], to do this reduction in dimension formally, we use the substitution $\int dk_y \rightarrow 2\pi/L_y$, where L_y is a normalization length scale in the y -direction. Therefore, the annihilation operator is redefined as

$$\hat{a}(k_x, k_y, \omega, l) \rightarrow \hat{a}(q, \omega, l) \sqrt{\frac{L_y}{2\pi}}, \quad (2.10)$$

which satisfies the commutation relations

$$[\hat{a}(q, \omega, l), \hat{a}^\dagger(q', \omega', l')] = \delta(q - q') \delta(\omega - \omega') \delta_{ll'}. \quad (2.11)$$

Finally, the simplified form of the electric field operator is then

$$\hat{\mathbf{E}}^{(+)}(\mathbf{r}, t) = \int_0^{+\infty} d\omega \hat{\mathbf{E}}^{(+)}(\mathbf{r}, \omega) \exp(-i\omega t), \quad (2.12)$$

where

$$\begin{aligned} \hat{\mathbf{E}}^{(+)}(x, z, \omega) = & i \left[\left(\frac{\hbar}{16c^2 \pi^3 \epsilon_0} \right) \left(\frac{2\pi}{L_y} \right) \right]^{1/2} \\ & \times \sum_l \int_{-\omega/c}^{+\omega/c} dq \left[\frac{\omega}{k_z^{1/2}} \hat{a}(q, \omega, l) \mathbf{e}(q, \omega, l) \exp(iqx + ik_z z) \right]. \end{aligned} \quad (2.13)$$

It is important to note that the term $k_z^{-1/2}$ in Eq. (2.13) tends to infinity as the transverse momentum $|q|$ increases towards ω/c and consequently k_z tends to 0. This diverging term becomes irrelevant if the treatment is reduced to the paraxial regime where all transverse momenta are small, i.e., $q^2 \ll \omega^2/c^2$, because $k_z^{-1/2}$ can be taken to be approximately independent of q [170]. The paraxial regime will suffice in the study of pinhole quantum ghost imaging in chapter 4 and quantum ghost polarimetry in chapter 5, while the full non-paraxial treatment will be needed to fully investigate the limit in resolution in chapter 3. The treatment of the diverging term $k_z^{-1/2}$ will be explained later in this chapter.

2.2. Spontaneous parametric down-conversion

Once the electric field operator has been derived, we proceed to calculate the quantum state produced by SPDC. As mentioned before in Eq. (2.1), the SPDC state contains the vacuum state $|0, 0\rangle$ and the two-photon state $|\psi\rangle$, where the latter contains the photon-pair information. The two-photon state has the form [7, 167]

$$|\psi\rangle = C_\psi \int dt \int d\mathbf{r} \sum_{\alpha, \beta, \gamma} \left[\chi_{\alpha\beta\gamma}^{(2)}(\mathbf{r}) E_{p,\gamma}(\mathbf{r}, t) \hat{E}_\alpha^{(-)}(\mathbf{r}, t) \hat{E}_\beta^{(-)}(\mathbf{r}, t) |0, 0\rangle \right], \quad (2.14)$$

where C_ψ is a constant, $\chi^{(2)}$ is the second-order nonlinear susceptibility of the crystal, the time integral $\int dt$ considers the interaction time and the spatial integral $\int d\mathbf{r}$ covers the volume of the nonlinear crystal where the interaction occurs. The coefficients γ, α, β refer to the polarization direction of the pump, signal, and idler fields, respectively. Additionally, we take the positive frequency part of the pump (P) in the

2 Basics of the two-photon quantum state

undepleted pump approximation, treating it as a classical field defined as

$$\mathbf{E}_p(\mathbf{r}, t) = \int_0^{+\infty} d\omega_p \mathbf{E}_p(\mathbf{r}, \omega_p) \exp(-i\omega_p t), \quad (2.15)$$

where its transverse spatial components can be expanded into plane waves,

$$\mathbf{E}_p(x, z) = \int_{-\infty}^{+\infty} dq_p \mathbf{E}_p(q_p; z=0) \exp(iq_p x + ik_{zP} z). \quad (2.16)$$

Here, we similarly consider only modes that propagate in the positive z -direction and in the x - z plane. Therefore, the introduction of the pump field and the electric field operator of Eq. (2.13) for the down-converted signal (S) and idler photons (I) into the two-photon state results in

$$\begin{aligned} |\psi\rangle &= C'_\psi \\ &\times \int_{-\infty}^{+\infty} dt \int_{-\infty}^{+\infty} dx \int_{-L/2}^{+L/2} dz \sum_{\alpha, \beta, \gamma} \chi_{\alpha\beta\gamma}^{(2)}(x, z) \\ &\times \int_0^{+\infty} d\omega_p \int_{-\infty}^{+\infty} dq_p E_{p,\gamma}(q_p, \omega_p) \exp[-i(\omega_p t - q_p x - k_{zP} z)] \\ &\times \int_0^{+\infty} d\omega_s \sum_{l_s} \int_{-\omega_s/c}^{+\omega_s/c} dq_s \frac{\omega_s}{k_{zS}^{1/2}} \hat{a}^\dagger(q_s, \omega_s, l_s) e_\alpha(q_s, \omega_s, l_s) \exp[i(\omega_s t - q_s x - k_{zS} z)] \\ &\times \int_0^{+\infty} d\omega_I \sum_{l_I} \int_{-\omega_I/c}^{+\omega_I/c} dq_I \frac{\omega_I}{k_{zI}^{1/2}} \hat{a}^\dagger(q_I, \omega_I, l_I) e_\beta(q_I, \omega_I, l_I) \exp[i(\omega_I t - q_I x - k_{zI} z)] |0, 0\rangle. \end{aligned} \quad (2.17)$$

Solving the spatial and time integrals results in

$$\int_{-\infty}^{+\infty} dt \exp[-i(\omega_p + \omega_s + \omega_I)t] = 2\pi \delta(\omega_p - \omega_s - \omega_I) \quad (2.18a)$$

$$\int_{-L/2}^{+L/2} dz \exp[i(k_{zP} - k_{zS} - k_{zI})z] = L \operatorname{sinc}\left(\frac{\Delta k_z L}{2}\right), \quad (2.18b)$$

$$\int_{-\infty}^{+\infty} dx \exp[i(q_p - q_s - q_I)x] = 2\pi \delta(q_p - q_s - q_I), \quad (2.18c)$$

where the interaction time is taken to be infinite since we consider the pump beam to be a continuous-wave laser with frequency ω_p throughout this thesis. This results in energy conservation $\hbar\omega_p = \hbar\omega_s + \hbar\omega_I$. Additionally, we take a nonlinear crystal that has a finite thickness L in the z -direction, with $\Delta k_z = k_{zP} - k_{zS} - k_{zI}$, and $k_z = [(2\pi/\lambda)^2 - q^2]^{1/2}$, where the pump, signal, and idler wavelengths are $\lambda_p, \lambda_s, \lambda_I$, respectively. In contrast, it is assumed that the crystal is much larger than the extent

of the pump beam in the transverse direction x , leading to the conservation of transverse momentum $\hbar q_p = \hbar q_s + \hbar q_I$. Moreover, we have considered the crystal to have a homogeneous susceptibility $\chi^{(2)}$.

In an experimental setting, narrowband spectral filters with central frequency ω are usually used before the signal and idler detectors to measure only specific photon frequencies. Consequently, according to energy conservation, the idler photon frequency is $\omega_I = \omega_p - \omega_s$ for a given signal frequency ω_s . These assumptions allow us to remove the $\int_0^{+\infty} d\omega$ integrals over the pump, signal, and idler frequencies in Eq. (2.17). Thus, resulting in the two-photon state

$$\begin{aligned}
 |\psi\rangle = & C''_{\psi} \sum_{\alpha,\beta,\gamma} \chi_{\alpha\beta\gamma}^{(2)} \sum_{l_s,l_I} \int_{-\omega_s/c}^{+\omega_s/c} dq_s \int_{-\omega_I/c}^{+\omega_I/c} dq_I \left\{ E_{p,\gamma}(q_s + q_I, \omega_s + \omega_I) \right. \\
 & \times \text{sinc}\left(\frac{\Delta k_z L}{2}\right) [k_{zs}(q_s)k_{zI}(q_I)]^{-1/2} \hat{a}^\dagger(q_s, \omega_s, l_s) e_\alpha(q_s, \omega_s, l_s) \\
 & \left. \times \hat{a}^\dagger(q_I, \omega_I, l_I) e_\beta(q_I, \omega_I, l_I) \right\} |0, 0\rangle. \quad (2.19)
 \end{aligned}$$

The state of Eq. (2.19) is the basis to describe the two-photon sources for the different schemes presented in this thesis. Each of these schemes uses a specific source that is based on different simplifications of the two-photon state of Eq. (2.19), as will be explained next.

2.2.1. Photon pairs entangled in momentum/angle

The schemes of quantum ghost imaging and quantum imaging with undetected photons reported in chapters 3 and 4, rely on the momentum and spatial correlations between the signal and idler photons. The information about the polarization is not used in our investigation of these schemes; therefore, to simplify the two-photon state of Eq. (2.19), we assume a crystal with a dominant nonlinear component $\chi_{yyy}^{(2)}$. The reason behind this decision is that we can fix one of the two polarization directions for any transverse wave-vector q of our model where we look at photons with $k_y \approx 0$. In detail, we can choose, e.g., $l = 1$ to be always along the y -direction and $l = 2$ to be orthogonal to it. Therefore, the choice to use the nonlinear component χ_{yyy} indicates that the generated signal and idler photons and the pump beam can be taken to be y -polarized. Consequently, a scalar formulation of the quantum state can be used, dropping the sums over l_s and l_I .

Using this simplification, the two-photon state is reduced to

$$|\psi\rangle = C'''_{\psi} \iint_{-\infty}^{+\infty} dq_s dq_I \phi(q_s, \omega_s; q_I, \omega_I) \hat{a}^\dagger(q_s, \omega_s) \hat{a}^\dagger(q_I, \omega_I) |0, 0\rangle, \quad (2.20)$$

with the joint transverse momentum amplitude

$$\begin{aligned} \phi(q_S, q_I) = E_P(q_S + q_I) \operatorname{sinc}\left(\Delta k_z \frac{L}{2}\right) [k_{zS}(q_S)k_{zI}(q_I)]^{-1/2} \\ \times \operatorname{rect}\left(|q_S| \leq \frac{\omega_S}{c}\right) \operatorname{rect}\left(|q_I| \leq \frac{\omega_I}{c}\right). \end{aligned} \quad (2.21)$$

To aid in understanding the upcoming analysis, the limits of the integral over the transverse momenta q have been rewritten in an alternative form. That is, the limits of the integral now denote the range $\pm\infty$ and now rectangular functions $\operatorname{rect}(\cdot)$, added to the argument of the integral, model the limited range of propagating waves. The rectangular function is equal to one wherever its argument is true, and zero otherwise. These functions explicitly show that the transverse momenta of both signal and idler are restricted by their corresponding wavelengths $|q| \leq \omega/c$. This means that modes with larger values of $|q|$ do not propagate since those correspond to evanescent modes, which are not considered throughout this thesis. The use of evanescent waves within the context of SPDC has been treated in other works [171, 172].

As mentioned before in Eq. (2.13) of the electric field operator, the term $(k_z)^{-1/2}$ in the joint transverse momentum amplitude in Eq. (2.21) diverges with q_S approaching ω_S/c or q_I approaching ω_I/c in the non-paraxial region. Therefore, this term introduces difficulties in the physical comprehension of the photon emission in terms of the transverse momenta. In the following, we analyze this peculiarity and prove that the singularity does not lead to an unphysical result. The strategy to accomplish this is to change the reference frame, namely to angular coordinates instead of spatial frequencies q . As we will show, the singularity is removed in the angular representation, leading to physical sound results that can be comfortably treated numerically. Hence, the angular representation can be used to find the probability of emitting a photon pair at a particular angle for signal and idler. The insight to treat the two-photon state from the angular representation was given by my colleague Elkin A. Santos.

The change of coordinates is based on the angle θ formed by the k vector and the z axis. The change of variables is performed first on the electric field operator, and then the two-photon state is found once again. The integrals are changed to the angular representation by defining $k_z = k \cos \theta$ and $q = k \sin \theta$, which gives $dq = d\theta k \cos \theta$. Moreover, the corresponding redefinition of the annihilation operator is $\hat{a}(q, \omega, l) = (k \cos \theta)^{-1/2} \hat{a}(\theta, \omega, l)$, which satisfies the commutation relations

$$[\hat{a}(\theta, \omega, l), \hat{a}^\dagger(\theta', \omega', l')] = \delta(\theta - \theta')\delta(\omega - \omega')\delta_{ll'}. \quad (2.22)$$

Therefore, the electric field operator of Eq. (2.13) in the angular representation is

$$\hat{\mathbf{E}}^{(+)}(x, z, \omega) = C_\theta \sum_l \int_{-\pi/2}^{\pi/2} d\theta \omega \hat{a}(\theta, \omega, l) \mathbf{e}(\theta, \omega, l) \exp(iqx + ik_z z), \quad (2.23)$$

with C_θ absorbing all the constant terms. It is noteworthy that the diverging term is absent, and the description already includes only the modes that are non-evanescent. Hence, the non-paraxial limit is described by higher values of θ with angle emissions $\theta \rightarrow \pm\pi/2$ and not by large values of $|q|$ approaching ω/c .

Next, in the same fashion as before, we introduce the angular electric field operator of Eq. (2.23) in the two-photon state of Eq. (2.14). As a result, using the same assumptions for the polarization, we obtain the two-photon state in the angular domain

$$|\psi\rangle = C_\psi''' \iint_{-\pi/2}^{\pi/2} d\theta_S d\theta_I \varphi(\theta_S, \omega_S; \theta_I, \omega_I) \hat{a}^\dagger(\theta_S, \omega_S) \hat{a}^\dagger(\theta_I, \omega_I) |0, 0\rangle, \quad (2.24)$$

where the joint angular amplitude is

$$\varphi(\theta_S, \omega_S; \theta_I, \omega_I) = E_p \left(\frac{\omega_S}{c} \sin(\theta_S) + \frac{\omega_I}{c} \sin(\theta_I), \omega_S + \omega_I \right) \text{sinc} \left(\frac{\Delta k_z L}{2} \right). \quad (2.25)$$

Consequently, Eqs. (2.24) and (2.25) describe the two-photon state by assuming a nonlinear crystal of thickness L that generates photon pairs in the angular modes $|\theta_S, \theta_I\rangle$.

The joint angular amplitude $\varphi(\theta_S, \theta_I)$ can be plotted to illustrate the angular entanglement between signal and idler photons. It is important to mention that throughout this thesis, we take the refractive index of free space $n = 1$ to describe the interaction of all the waves in the nonlinear crystal. This means that $\omega/c = 2\pi/\lambda$ for pump, signal and idler. The reason behind this decision is to have the largest range of generated transverse wave-vectors that can be produced by an ideal nonlinear crystal, since our aim is to study the fundamentals of the schemes and not be constrained to a specific case. Depending on the specific refractive indices of a nonlinear crystal, total internal reflection and multiple reflections that occur at the end facets between the crystal and the outside free space can hinder the transmission of some photons generated within the crystal to the outside medium [173–176]. Therefore, carrying out our analysis under this condition of refractive index $n = 1$ does not affect the main physics of our problem and we focus on all propagating waves that have a transverse wave-vector smaller than the wave-vector in free space.

We show examples of $\varphi(\theta_S, \theta_I)$ in Fig. 2.2 with a pump beam that has a transverse

2 Basics of the two-photon quantum state

Gaussian profile of width $10\mu\text{m}$ and a wavelength of $\lambda_p = 500\text{nm}$. In these numerical examples, we portray φ for the case of a thick crystal ($L = 20\mu\text{m}$) in Figs. 2.2(a,b) and for an ultra-thin source ($L = 3\text{nm}$) in Figs. 2.2(c, d), each for two cases: First, signal and idler with degenerate wavelengths [Figs. 2.2(a,c)], here $\lambda_s/\lambda_i = 1$ with $\lambda_s = \lambda_i = 1\mu\text{m}$. Second, signal and idler with non-degenerate wavelengths [Figs. 2.2(b,d)] with $\lambda_s/\lambda_i = 0.8$, where $\lambda_s = 900\text{nm}$ and $\lambda_i = 1.125\mu\text{m}$. Lastly, the inset of Fig. 2.2(a) shows a sketch of the angle θ that the k -vector makes with the z axis in the $x - z$ plane.

We observe in Figs. 2.2(a, b) that the generation for both signal and idler photons can be found only within a small range of angles for the case of a thicker crystal ($L = 20\mu\text{m}$) in the degenerate and non-degenerate scenarios. The reason for the generation in a small angular range is caused by the longitudinal phase-matching effect embedded in the sinc function of Eq. (2.25). Moreover, the shape of the joint angular amplitude changes slightly with non-degenerate wavelengths displaying a tilt

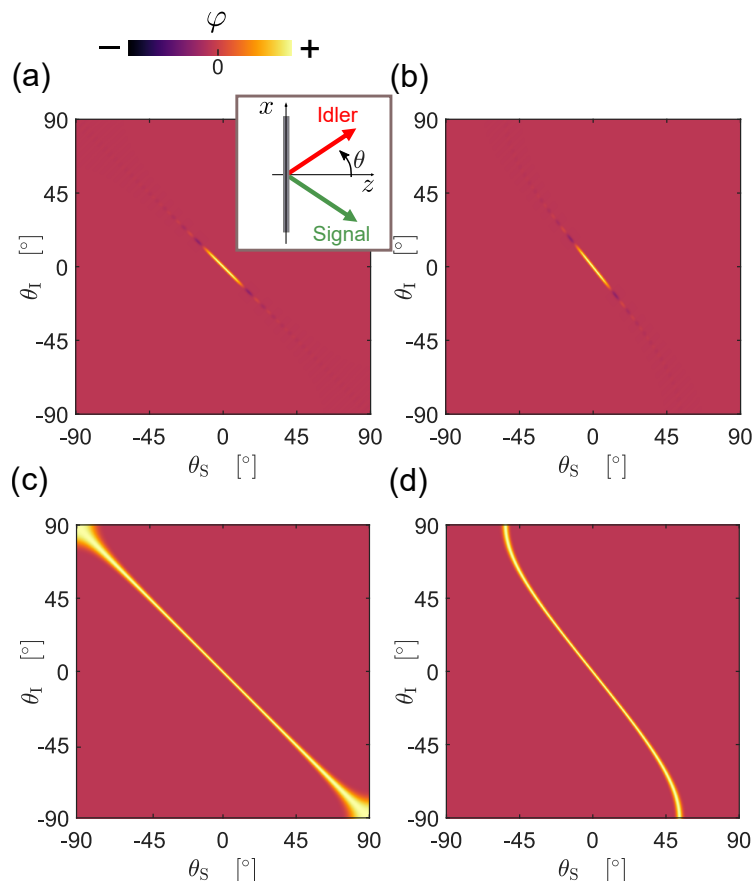


Figure 2.2. Joint angular amplitude $\varphi(\theta_s, \theta_i)$ within $|\theta_{s,i}| \leq 90^\circ$ for signal/idler wavelengths of (a, c) $\lambda_s/\lambda_i = 1$ and (b, d) $\lambda_s/\lambda_i = 0.8$. The pump beam has a width of $10\mu\text{m}$. The crystal thickness L is in (a, b) larger than the pump, signal and idler wavelengths ($L = 20\mu\text{m}$), while in (c, d) L is much smaller than any of the three wavelengths ($L = 3\text{nm}$). The inset shows a sketch of the angle θ that the k -vector makes with the z axis in the $x - z$ plane.

of the higher-amplitude region. Such an effect is more noticeable for the ultra-thin crystal shown in Figs. 2.2(c, d). For an ultra-thin source, namely $L \rightarrow 0$, the sinc-function in Eq. (2.25) approaches one for all angles, therefore the term that defines the joint angular amplitude is the pump term

$$E_p [q_p = (\omega_s/c) \sin(\theta_s) + (\omega_I/c) \sin(\theta_I)]. \quad (2.26)$$

Consequently, in the thin-source limit, there is no limitation on the range of the generated signal and idler angles, as long as they can satisfy the transverse phase-matching condition. Figure 2.2(c) shows $\varphi(\theta_s, \theta_I)$ for the degenerate case with $\lambda_s = \lambda_I$, where it is clear that both photons can be generated in the whole range of $|\theta_{s,I}| \leq 90^\circ$. In the non-degenerate case with $\lambda_s/\lambda_I < 1$, see Fig. 2.2(d), we observe that the idler photons with a longer wavelength are generated in the whole range of $|\theta_I| \leq 90^\circ$, while the signal photons can only be generated within a restricted range. This limited range is given by the transverse phase-matching condition as follows: Consider the simple case where the pump is almost a plane wave with $q_p = 0$ impinging normally on the nonlinear crystal. Then, the resulting transverse phase-matching condition is $(\omega_s/c) \sin(\theta_s) + (\omega_I/c) \sin(\theta_I) = 0$ for the signal and idler photons, or written otherwise $\sin(\theta_s) = -(\lambda_s/\lambda_I) \sin(\theta_I)$. It is clear from this expression that, for degeneracy factors $\lambda_s/\lambda_I < 1$, the possible angular generation range of signal photons with shorter wavelength will be confined to

$$\theta_s^{\max} = |\sin^{-1}[(\lambda_s/\lambda_I) \sin(\theta_I = 90^\circ)]| = |\sin^{-1}(\lambda_s/\lambda_I)|. \quad (2.27)$$

Intuitively, this is due to the fact that the magnitude of the wave vector for the longer-wavelength idler photons is smaller than that of the shorter-wavelength signal, and cannot satisfy the transverse phase-matching condition $q_s = -q_I$ with the signal photon after θ_s^{\max} , therefore, no signal photons will be generated after that angle. Importantly, this physical effect will play a key role in setting the fundamental resolution limit of quantum imaging as discussed in chapter 3.

2.2.2. Photon pairs entangled in polarization

Quantum ghost polarimetry, presented in chapter 5, relies on a source with signal and idler photons entangled exclusively in polarization. To theoretically describe such photon-pair source, the spatial distribution of the down-converted photons can be approximated to just one plane wave propagating in a certain direction. Consequently,

the integrals over q of the two-photon state of Eq. (2.19) can be dropped,

$$|\psi\rangle = C_\phi'''' \sum_{\alpha,\beta,\gamma} \chi_{\alpha\beta\gamma}^{(2)} \sum_{l_s,l_I} \hat{a}^\dagger(l_s) e_\alpha(l_s) \hat{a}^\dagger(l_I) e_\beta(l_I) |0,0\rangle. \quad (2.28)$$

From this state, an entangled state in polarization can be obtained by an appropriate choice of the nonlinear coefficient $\chi^{(2)}$ so that the two-photon state includes both polarizations l_1 and l_2 and results in one of the following four forms

$$|\psi\rangle_\pm = [C_1 \hat{a}^\dagger(l_{1,s}) \hat{a}^\dagger(l_{1,I}) \pm C_2 \hat{a}^\dagger(l_{2,s}) \hat{a}^\dagger(l_{2,I})] |0,0\rangle, \quad (2.29a)$$

$$|\psi'\rangle_\pm = [C'_1 \hat{a}^\dagger(l_{1,s}) \hat{a}^\dagger(l_{2,I}) \pm C'_2 \hat{a}^\dagger(l_{2,s}) \hat{a}^\dagger(l_{1,I})] |0,0\rangle. \quad (2.29b)$$

The constants $C_{1,2}$ and $C'_{1,2}$ of Eq. (2.29) contain the nonlinear coefficient $\chi^{(2)}$ and are in general complex numbers, since a phase difference between the two terms of $|\psi\rangle$ can exist due to dispersion and/or path-length difference. To achieve in practice one of such states of Eq. (2.29), experiments are built with, e.g., a single crystal with type-II phase matching [67], or two cascaded down-conversion crystals with type-I phase matching [68], or one crystal in a Sagnac loop [177, 178]. It is worth mentioning that the two-level states of Eq. (2.29) correspond to the Bell states [179].

In this thesis, we will assume the simple case where the two-photon state is $|\psi\rangle = |\psi\rangle_+$ and $C_1 = C_2 = C$, which is sufficient to discuss the quantum ghost polarimetry scheme in chapter 5 without losing generality. Additionally, we take therein that l_1 corresponds to the horizontal (H) polarization and l_2 to the vertical (V) polarization, leading to the final form of the two-photon state entangled in polarization that will be used in chapter 5,

$$|\psi\rangle = C [\hat{a}^\dagger(H_s) \hat{a}^\dagger(H_I) + \hat{a}^\dagger(V_s) \hat{a}^\dagger(V_I)] |0,0\rangle. \quad (2.30)$$

2.3. Abstract and publication

A theoretical formalism of photon-pair generation was presented and constitutes the basis for the schemes featured in the next chapters. Quantum ghost imaging and quantum imaging with undetected photons (chapters 3 and 4) use transverse-momentum entanglement, whereas quantum ghost polarimetry (chapter 5) is based on the source with signal and idler photons entangled in polarization. In particular, the two-photon quantum state with momentum entanglement beyond the paraxial regime was published as a section of the publication [180], in which the fundamental resolution of quantum imaging is derived.

3. Fundamental resolution limit of two-color quantum imaging

Quantum imaging with undetected photons (QIUP) and quantum ghost imaging (QGI) are the schemes with two-color photon pairs studied in this thesis. As described in chapter 1, QIUP allows us to obtain images based on the effect of induced coherence without induced emission, and, unlike QGI, coincidence measurements are not needed. This means that although the idler photons that interact with the object are never measured, the measurement of only signal photons suffices to obtain the image of the object. QIUP and QGI can work with non-degenerate photon pairs to ease limitations in detection and measurement, which is advantageous in biosensing. In this chapter, the dependence of the resolution of QIUP and QGI on the wavelengths of the photon pair beyond the paraxial regime is presented.

We begin by theoretically describing a scheme of QIUP that is enabled by the position correlations of signal and idler photons using the formalism of chapter 2. Furthermore, we study the fundamental resolution of QIUP by using two slits of infinitesimal width and find the minimum resolvable distance between them. Additionally, in a similar fashion, we derive the fundamental resolution limit of QGI based on position correlations. Lastly, based on our analysis and results, we discuss about the resolution of other QIUP and QGI configurations.

3.1. Quantum imaging with undetected photons

The first realization of an imaging scheme based on induced coherence without induced emission was published in 2014 by Lemos et al. [147] together with a detailed theoretical description of the scheme within the paraxial regime given in Ref. [148]. The scheme is designed so that imaging is achieved by using the *momentum* correlations of the signal and idler photons. However, the QIUP configuration that will be discussed here, see Fig. 3.1, relies on the *position* correlations of the down-converted photons. The scheme consists of two photon-pair sources A and B that form a non-linear interferometer [181]. Each crystal produces a two-photon state with entangle-

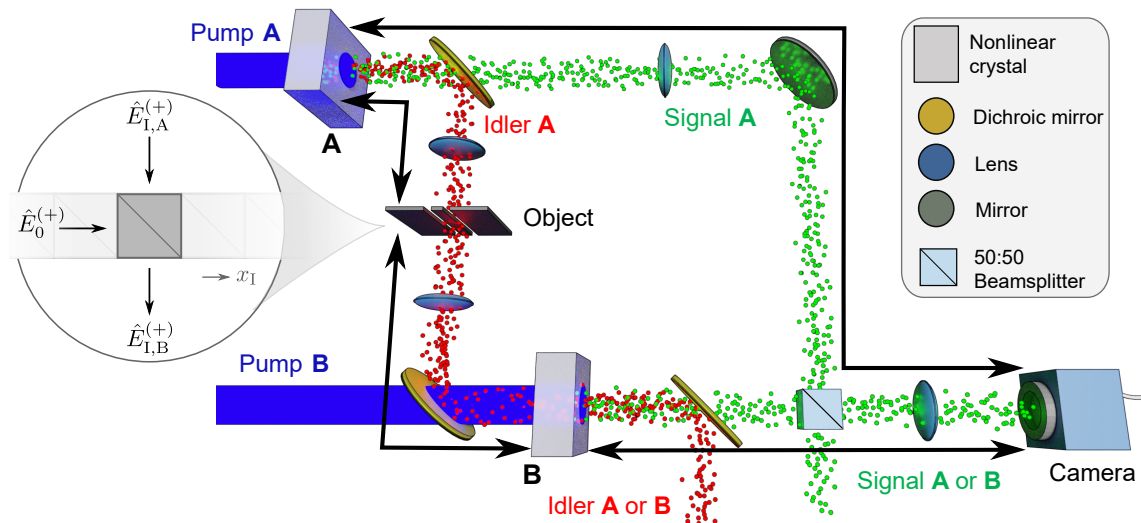


Figure 3.1. Sketch of quantum imaging with undetected photons (QIUP) based on position correlations. In the idler arm, the central plane of crystal A is imaged onto the object by an optical system with magnification one (represented by the arrow). The object is then imaged on the central plane of crystal B. In the signal arm, the central planes of both crystals are imaged onto the camera. Inset: model of the object composed of a beamsplitter at each x_I position.

ment in transverse momentum, as was presented in section 2.2.1. Additionally, since the signal and idler photons of a pair are created at the same position, they are also spatially correlated [167]. In the idler arm, the central plane of source A is imaged on the object using an imaging system with magnification equal to one, represented by a black arrow. In the same manner, the object plane is imaged on the central plane of source B. In the signal arm, the central planes of both sources are imaged onto the camera. The signal photons of both sources that never interact with the object interfere at the beamsplitter and are measured by the camera revealing the object, while the idler photons remain undetected.

In this section, we derive the expression of the photon-counting rate at the camera in a similar fashion as Ref. [182]. The difference lies in the fact that our analysis is not restricted to photon pairs propagating only in the paraxial regime. Since the range of angular propagation of the photons defines the transverse resolution, as will be shown, this proposed model of QIUP beyond the paraxial regime can be used to evaluate the fundamental resolution of QIUP. As we will demonstrate, the fundamental resolution can be achieved by using thin sources and in a strongly non-paraxial regime of operation. It should be mentioned that the derivation of the expression of the image will be performed in the transverse-momentum representation because of the simple form of the expressions. However, we convert to the angular domain for numerical evaluations and interpretation of the physics since these expressions are singularity-free, as shown in section 2.2.1.

The quantum state of the system $|\psi\rangle_{\text{SPDC,AB}}$, composed of sources A and B, can be written as the superposition of their respective SPDC states [see Eq. (2.1)], therefore,

$$\begin{aligned} |\psi\rangle_{\text{SPDC,AB}} &= |\psi\rangle_{\text{SPDC,A}} + |\psi\rangle_{\text{SPDC,B}} \\ &= |0, 0\rangle_{\text{A}} + |0, 0\rangle_{\text{B}} + |\psi\rangle_{\text{AB}} \end{aligned} \quad (3.1)$$

with the two-photon state of the system of two sources $|\psi\rangle_{\text{AB}} = |\psi\rangle_{\text{A}} + |\psi\rangle_{\text{B}}$, where $|\psi\rangle_{\text{A(B)}}$ is the two-photon quantum state of source A (B) derived in chapter 2, namely, shown in Eqs. (2.20) and (2.21). Consequently,

$$\begin{aligned} |\psi\rangle_{\text{AB}} &= |\psi\rangle_{\text{A}} + |\psi\rangle_{\text{B}} \\ &= C'''_{\psi,\text{A}} \iint dq_{\text{S,A}} dq_{\text{I,A}} \phi_{\text{A}}(q_{\text{S,A}}; q_{\text{I,A}}) \hat{a}_{\text{A}}^{\dagger}(q_{\text{S,A}}) \hat{a}_{\text{A}}^{\dagger}(q_{\text{I,A}}) |0, 0\rangle_{\text{A}} \\ &\quad + C'''_{\psi,\text{B}} \iint dq_{\text{S,B}} dq_{\text{I,B}} \phi_{\text{B}}(q_{\text{S,B}}; q_{\text{I,B}}) \hat{a}_{\text{B}}^{\dagger}(q_{\text{S,B}}) \hat{a}_{\text{B}}^{\dagger}(q_{\text{I,B}}) |0, 0\rangle_{\text{B}}. \end{aligned} \quad (3.2)$$

The low-gain regime of photon-pair generation is considered throughout this work, and hence at most one pair at a time is present in the QIUP system [183].

As a next step, the presence of the object in the idler arm of source A can be included in the state of the system as a lossless element to preserve the probability $\langle\psi|_{\text{AB}}|\psi\rangle_{\text{AB}}$. Namely, as portrayed in the inset of Fig. 3.1, each transverse position x_{I} of the object is modeled by a beamsplitter with transmission $T(x_{\text{I}})$ and reflection $R(x_{\text{I}})$. Since the beamsplitter is a lossless element [184], then $T(x)T^*(x) + R(x)R^*(x) = 1$. Here, the electric field at one of the inputs of the beamsplitter is $\hat{E}_{\text{I,A}}^{(+)}(x_{\text{I}})$ and the other is the vacuum $\hat{E}_0^{(+)}(x_{\text{I}})$. The collinear output with $\hat{E}_{\text{I,A}}^{(+)}(x_{\text{I}})$ that is directed towards source B can be written in terms of the inputs as

$$\hat{E}_{\text{I,B}}^{(+)}(x_{\text{I}}) = T(x_{\text{I}})\hat{E}_{\text{I,A}}^{(+)}(x_{\text{I}}) + R(x_{\text{I}})\hat{E}_0^{(+)}(x_{\text{I}}). \quad (3.3)$$

Given that the idler arms of the two crystals are aligned to introduce indistinguishability by the imaging conditions described above, each position output mode of the beamsplitter coincides with the position modes of the idler of source B [149, 182]. Next, we use the electric field operator presented in chapter 2 in Eq. (2.13) and simplify it using the assumption that the field has a fixed polarization along the y -direction as a result of assuming a crystal with a dominant nonlinear component $\chi_{yyy}^{(2)}$. Therefore, Eq. (2.13) becomes

$$\hat{E}_{\text{I,j}}^{(+)}(x_{\text{I}}) = C \int dq_{\text{I}} \exp(iq_{\text{I}}x_{\text{I}})(k_{z\text{I}})^{-1/2} \text{rect}\left(|q_{\text{I}}| \leq \frac{2\pi}{\lambda_{\text{I}}}\right) \hat{a}_{\text{j}}(q_{\text{I}}) \quad (3.4)$$

with $j \in \{A, B, 0\}$ and C is a constant. For ease of reading, the limits of any integral are $\pm\infty$ unless otherwise noted. By putting Eq. (3.4) into Eq. (3.3) and using the inverse Fourier transform of the transmission and reflection

$$T(x_I) = \frac{1}{2\pi} \int dx_I \tilde{T}(q_I) \exp(iq_I x_I), \quad (3.5a)$$

$$R(x_I) = \frac{1}{2\pi} \int dx_I \tilde{R}(q_I) \exp(iq_I x_I), \quad (3.5b)$$

we can find the relation between the idler annihilation operators of source B in the q -domain with respect to the object's \tilde{T} and \tilde{R} . That is,

$$\begin{aligned} & \hat{a}_B(q_I) (k_{zI})^{-1/2} \text{rect}\left(|q_I| \leq \frac{2\pi}{\lambda_I}\right) \\ &= \frac{1}{2\pi} \int dq'_I \left[\tilde{T}(q_I - q'_I) \hat{a}_A(q'_I) + \tilde{R}(q_I - q'_I) \hat{a}_0(q'_I) \right] (k'_{zI})^{-1/2} \text{rect}\left(|q'_I| \leq \frac{2\pi}{\lambda_I}\right), \end{aligned} \quad (3.6)$$

where on the right-hand side we combined the integrals $T(x_I) \hat{E}_{I,A}^{(+)}(x_I)$ and $R(x_I) \hat{E}_0^{(+)}(x_I)$ in the following manner,

$$\begin{aligned} T(x_I) \hat{E}_{I,A}^{(+)}(x_I) &= \frac{1}{2\pi} C \\ &\times \iint d\tilde{q}_I dq'_I \tilde{T}(\tilde{q}_I) \hat{a}_A(q'_I) (k'_{zI})^{-1/2} \text{rect}\left(|q'_I| \leq \frac{2\pi}{\lambda_I}\right) \exp[i(\tilde{q}_I + q'_I)x_I] \end{aligned} \quad (3.7)$$

along with $q_I = \tilde{q}_I + q'_I$ and $dq_I = d\tilde{q}_I$. The integrals of the term $R(x_I) \hat{E}_0^{(+)}(x_I)$ were similarly combined.

It is important to note that the rectangular function ensures that only propagating modes of the idler are taken into account. Inserting Eq. (3.6) into the quantum state of the system and taking into account that signal photons of both sources interfere in a common path, i.e., $q_{S,A} = q_{S,B} = q_S$, then

$$\begin{aligned} |\psi\rangle_{AB} &= C'''_{\psi,A} \iint dq_S dq_I \phi_A(q_S; q_I) \hat{a}_A^\dagger(q_S) \hat{a}_A^\dagger(q_I) |0, 0\rangle \\ &+ \frac{1}{2\pi} C'''_{\psi,B} \iint dq_S dq_I \left\{ \phi_B(q_S; q_I) (k_{zI})^{1/2} \right. \\ &\quad \times \left[\int dq'_I \tilde{T}^*(q_I - q'_I) (k'_{zI})^{-1/2} \text{rect}\left(|q'_I| \leq \frac{2\pi}{\lambda_I}\right) \hat{a}_A^\dagger(q'_I) \right] \hat{a}_B^\dagger(q_S) |0, 0\rangle \left. \right\} \\ &+ \frac{1}{2\pi} C'''_{\psi,B} \iint dq_S dq_I \left\{ \phi_B(q_S; q_I) (k_{zI})^{1/2} \right. \\ &\quad \times \left[\int dq'_I \tilde{R}^*(q_I - q'_I) (k'_{zI})^{-1/2} \text{rect}\left(|q'_I| \leq \frac{2\pi}{\lambda_I}\right) \hat{a}_0^\dagger(q'_I) \right] \hat{a}_B^\dagger(q_S) |0, 0\rangle \left. \right\}. \end{aligned} \quad (3.8)$$

By reorganizing the integrals of q_I and q'_I in the second and third terms, we have

$$\begin{aligned}
 |\psi\rangle_{AB} &= C'''_{\psi,A} \iint dq_S dq_I \phi_A(q_S; q_I) \hat{a}_A^\dagger(q_S) \hat{a}_A^\dagger(q_I) |0, 0\rangle \\
 &+ \frac{1}{2\pi} C'''_{\psi,B} \iint dq_S dq'_I \left\{ (k'_{zI})^{-1/2} \left[\int dq_I (k_{zI})^{1/2} \phi_B(q_S; q_I) \tilde{T}^*(q_I - q'_I) \right] \right. \\
 &\quad \left. \times \text{rect} \left(|q'_I| \leq \frac{2\pi}{\lambda_1} \right) \hat{a}_A^\dagger(q'_I) \hat{a}_B^\dagger(q_S) |0, 0\rangle \right\} \\
 &+ \frac{1}{2\pi} C'''_{\psi,B} \iint dq_S dq'_I \left\{ (k'_{zI})^{-1/2} \left[\int dq_I (k_{zI})^{1/2} \phi_B(q_S; q_I) \tilde{R}^*(q_I - q'_I) \right] \right. \\
 &\quad \left. \times \text{rect} \left(|q'_I| \leq \frac{2\pi}{\lambda_1} \right) \hat{a}_0^\dagger(q'_I) \hat{a}_B^\dagger(q_S) |0, 0\rangle \right\}.
 \end{aligned} \tag{3.9}$$

The terms within the square brackets can be written as convolutions along q'_I to simplify the notation, which will be indicated by \otimes , and bearing in mind that $\widetilde{(T^*)}(q'_I) = \tilde{T}^*(-q'_I)$,

$$\int dq_I (k_{zI})^{1/2} \phi_B(q_S; q_I) \tilde{T}^*(q_I - q'_I) = [(k'_{zI})^{1/2} \phi_B(q_S, q'_I)] \otimes \widetilde{(T^*)}(q'_I), \tag{3.10a}$$

$$\int dq_I (k_{zI})^{1/2} \phi_B(q_S; q_I) \tilde{R}^*(q_I - q'_I) = [(k'_{zI})^{1/2} \phi_B(q_S, q'_I)] \otimes \widetilde{(R^*)}(q'_I). \tag{3.10b}$$

To harness the position correlations to achieve imaging, signal photons interfere in a 50 : 50 beamsplitter and are then measured by a camera located in the image plane of both sources. The electric field operator that describes the measurement performed by the camera is

$$\hat{E}_{\text{cam}}^{(+)} = C \int dq_S \exp(iq_S x_S) k_{zS}^{-1/2} \text{rect} \left(|q_S| \leq \frac{2\pi}{\lambda_S} \right) [\hat{a}_A(q_S) + i \exp(i\eta) \hat{a}_B(q_S)], \tag{3.11}$$

where η is the accumulated phase difference between the two signal arms.

Ultimately, the photon counting rate at the camera is found by [185]

$$\mathcal{R}(x_S) \propto \langle \psi |_{\text{SPDC,AB}} \hat{E}_{\text{cam}}^{(-)} \hat{E}_{\text{cam}}^{(+)} | \psi \rangle_{\text{SPDC,AB}}, \tag{3.12}$$

using the SPDC state of the system $|\psi\rangle_{\text{SPDC,AB}}$ of Eq. (3.1) and the electric field operator at the camera $\hat{E}_{\text{cam}}^{(+)}$ of Eq. (3.11). Furthermore, it is relevant for the derivation of $\mathcal{R}(x_S)$ to consider the orthogonality relations

$$\langle 0, 0 | \hat{a}_p(q'_I) \hat{a}_l^\dagger(q_I) | 0, 0 \rangle = \begin{cases} \delta(q' - q) = \frac{1}{2\pi} \int dx_I \exp[-i(q' - q)x_I], & \text{if } p = l \\ 0, & \text{if } p \neq l \end{cases} \tag{3.13}$$

with $p, l \in \{A, 0\}$. To find \mathcal{R} , it is also important to consider that the mentioned relation of the transmission and reflection of a lossless beamsplitter $T(x)T^*(x) + R(x)R^*(x) = 1$ expressed in q -domain is $\tilde{T}(q)\tilde{T}^*(q') + \tilde{R}(q)\tilde{R}^*(q') = (2\pi)^2\delta(q)\delta(q')$. Finally, after a long but straightforward calculation, the photon counting rate at the camera is found to be

$$\mathcal{R}(x_S) = \int dx_I \left[C_A |\Phi_A|^2 + C_B |\Phi_B|^2 + C_{AB} \text{Re}(\Phi_A^* \Phi_{B\tilde{T}}) \right], \quad (3.14)$$

with C absorbing all the respective constants and

$$\Phi_A(x_S, x_I) = \iint dq_I dq_S \exp(iq_S x_S + iq_I x_I) (k_{zS})^{-1/2} \phi_A(q_S, q_I), \quad (3.15a)$$

$$\Phi_B(x_S, x_I) = \iint dq_I dq_S \exp(iq_S x_S + iq_I x_I) (k_{zS})^{-1/2} \phi_B(q_S, q_I), \quad (3.15b)$$

$$\begin{aligned} \Phi_{B\tilde{T}}(x_S, x_I) = & \iint dq_I dq_S \left[\exp(iq_S x_S + iq_I x_I) (k_{zS} k_{zI})^{-1/2} \right. \\ & \left. \times \text{conv}(q_S, q_I) \text{rect}\left(|q_I| \leq \frac{2\pi}{\lambda_I}\right) \right]. \end{aligned} \quad (3.15c)$$

Here, $\text{conv}(q_S, q_I)$ denotes the following convolution \otimes along q_I

$$\begin{aligned} \text{conv}(q_S, q_I) = & \left[(k_{zI})^{1/2} \phi_B(q_S, q_I) \right] \otimes (\widetilde{T^*})(q_I) \\ = & \int dq'_I (k'_{zI})^{1/2} \phi_B(q_S, q'_I) \tilde{T}^*(q'_I - q_I). \end{aligned} \quad (3.16)$$

For convenience, the phase difference between the signals in the third term of \mathcal{R} is taken $\eta = -\pi/2$ to have constructive interference in the arm of the camera, i.e., $C_{AB} > 0$, while the second output of the 50 : 50 beamsplitter would then lead to destructive interference.

On the one hand, we observe that $\int dx_I (C_A |\Phi_A|^2 + C_B |\Phi_B|^2)$ of the photon counting rate at the camera of Eq. (3.14), are proportional to the photon counting rate of the signal photons of each source as if the other source were absent. Importantly, these two terms do not carry information about the object and therefore constitute the background counts. On the other hand, the interference term contains the transmission of the object within $\text{conv}(q_S, q_I)$, we will refer to this interference term as the image term,

$$\mathcal{I}_{\text{QIUP}}(x_S) = C_{AB} \int dx_I \text{Re}(\Phi_A^* \Phi_{B\tilde{T}}). \quad (3.17)$$

This image term corresponds to the joint response of the sources and contains infor-

mation of the object due to the phenomenon of induced coherence without induced emission, as occurs similarly in QIUP that uses momentum correlations [148]. Therefore, this image term is relevant to study the resolution of QIUP. Additionally, the background contribution can be removed to reveal the image $\mathcal{I}_{\text{QIUP}}$ by exploiting the phase difference of both output ports of the beamsplitter and subtracting one image from the other [147]. From here on, we will take into account only the image term that contains the transmission of the object to discuss the resolution limit.

3.1.1. Fundamental transverse resolution limit

The resolution of a conventional imaging system depends on the illumination wavelength and also on the numerical aperture of the optical elements [158]. In this section, we focus on evaluating the resolution of QIUP at its fundamental limit; consequently, we assume that the optical elements in Fig. 3.1 have a numerical aperture equal to one and we concentrate on the dependence of the transverse resolution on the signal and idler wavelengths $\lambda_{\text{S,I}}$. In particular, we evaluate the fundamental resolution of QIUP, based on the non-paraxial expressions found in the previous section 3.1 using a double slit as the object. First, we simplify the found analytical expression of the image to investigate the resolution. Later, we investigate numerically the difference in resolution between a QIUP system with thick and ultra-thin SPDC sources in a highly non-degenerate scenario. Lastly, we find the QIUP resolution as a function of the thickness of the SPDC sources, demonstrating that the fundamental resolution is reached for sources approximately thinner than $\max(\lambda_{\text{S}}, \lambda_{\text{I}})$, with the fundamental resolution being approximately $\max(\lambda_{\text{S}}, \lambda_{\text{I}})/2$.

Image of a double slit

We simplify here the derived analytical expressions to find the image with the purpose of obtaining the resolution. To this end, we use Rayleigh's criterion [158] and assume that the object consists of two infinitely thin slits that are separated by a distance d , namely with a transmission

$$T(x_I) = \delta\left(x_I - \frac{d}{2}\right) + \delta\left(x_I + \frac{d}{2}\right), \quad (3.18)$$

and we find their image using Eq. (3.17). The resolution will be given by the minimum resolvable distance d_{min} between the two slits. We model the transverse profile of the pump beam with a Gaussian profile of width σ_p to analyze realistic experimental scenarios where the degree of entanglement in momentum of signal and idler is

3 Fundamental resolution limit of two-color quantum imaging

degraded [186], that is, $E_p(q_p) = \exp(-\sigma_p^2 q_p^2/2)$. Incorporating these considerations into the joint transverse momentum amplitude of the quantum state [see Eq. (2.21)], then the convolution term of Eq. (3.16), which carries the information of the transmission of the object in the image term $\mathcal{I}_{\text{QIUP}}$, becomes

$$\begin{aligned} \text{conv}(q_S, q_I) &= (k_{zS})^{-1/2} \text{rect}\left(|q_S| \leq \frac{2\pi}{\lambda_S}\right) \text{Re}\left\{ \exp\left(i\frac{d}{2}q_I\right) \int dq'_I \exp\left(-i\frac{d}{2}q'_I\right) \right. \\ &\quad \left. \times \text{sinc}\left[\frac{\Delta k_z(q_S, q'_I)L_B}{2}\right] \exp\left[-\frac{\sigma_p^2}{2}(q_S + q'_I)^2\right] \text{rect}\left(|q'_I| \leq \frac{2\pi}{\lambda_I}\right) \right\}. \end{aligned} \quad (3.19)$$

It is worth analyzing the limit where signal and idler have the strongest possible correlation to find the fundamental limitation of the resolution, i.e., using a plane wave pump where $\sigma_p \rightarrow \infty$. In this extreme case of perfect correlation, the convolution term simplifies to

$$\begin{aligned} \text{conv}(q_S, q_I) &= (k_{zS})^{-1/2} \cos\left[\frac{d}{2}(q_S + q_I)\right] \\ &\quad \times \text{sinc}\left\{\frac{L_B}{2}\left[\frac{2\pi}{\lambda_p} - k_{zS} - \kappa\right]\right\} \text{rect}\left[|q_S| \leq 2\pi \min\left(\frac{1}{\lambda_S}, \frac{1}{\lambda_I}\right)\right] \end{aligned} \quad (3.20)$$

with $\kappa := [(2\pi/\lambda_I)^2 - q_S^2]^{1/2}$ and most importantly

$$\text{rect}\left(|q_S| \leq \frac{2\pi}{\lambda_S}\right) \text{rect}\left(|q_S| \leq \frac{2\pi}{\lambda_I}\right) = \text{rect}\left[|q_S| \leq 2\pi \min\left(\frac{1}{\lambda_S}, \frac{1}{\lambda_I}\right)\right]. \quad (3.21)$$

The cosine term of Eq. (3.20) carries the information on the distance between the slits d ; the closer the slits, the larger the period of the cosine in the q -domain. If the cosine were the only term defining the term $\text{conv}(q_S, q_I)$, infinitely close slits can be resolved in the image, since the cosine spreads infinitely over all possible transverse-momentum modes that carry the information of any distance d between the slits. However, as was shown in the chapter 2, a photon pair source can only generate modes with a restricted range of transverse momentum, where the limit is set by the thickness of the source and fundamentally by the diffraction limit set by the wavelengths of the signal and idler photons. Consequently, the resolution will be restricted by this limited range of transverse wave-vectors. This limit of the transverse momenta is modeled by the sinc and rectangular functions appearing in Eq. (3.20). In this equation, the hard limit for the range of available transverse wave-vectors for the measured signal photons is

$$2\pi \min\left(\frac{1}{\lambda_S}, \frac{1}{\lambda_I}\right), \quad (3.22)$$

which means that the limit is set by the larger of the signal and idler wavelengths. Therefore, resolving the slit distance carried in the cosine term of Eq. (3.20) will be restricted by the diffraction-limit of the larger wavelength between signal and idler, which is given by the limit of the propagating waves. This fact is the main physical finding of this chapter. We proceed to verify this result with numerical calculations of the image of the two slits.

For our numerical calculations, we resort to the angular representation, since the singularity terms that appear in the q -domain are then avoided. The functions Φ_A and $\Phi_{B\tilde{T}}$ can be expressed in angular coordinates, as discussed in section 2.2.1. To this end, we take $q = (2\pi/\lambda)\sin(\theta)$, $k_z = (2\pi/\lambda)\cos(\theta)$ and $dq = k_z d\theta$, leading to

$$\Phi_A(x_S, x_I) = \iint_{-\pi/2}^{+\pi/2} d\theta_I d\theta_S \varphi_A(\theta_S, \theta_I) \exp\left[i\frac{2\pi}{\lambda_S}\sin(\theta_S)x_S + i\frac{2\pi}{\lambda_I}\sin(\theta_I)x_I\right], \quad (3.23a)$$

$$\Phi_{B\tilde{T}}(x_S, x_I) = \iint_{-\pi/2}^{+\pi/2} d\theta_I d\theta_S \varphi_{B\tilde{T}}(\theta_S, \theta_I) \exp\left[i\frac{2\pi}{\lambda_S}\sin(\theta_S)x_S + i\frac{2\pi}{\lambda_I}\sin(\theta_I)x_I\right], \quad (3.23b)$$

where

$$\varphi_A(\theta_S, \theta_I) = \left[\frac{2\pi}{\lambda_I}\cos(\theta_I)\right]^{1/2} E_P(\theta_S, \theta_I) \Pi(\theta_S, \theta_I, L_A), \quad (3.24a)$$

$$\varphi_{B\tilde{T}}(\theta_S, \theta_I) = \left[\frac{2\pi}{\lambda_I}\cos(\theta_I)\right]^{1/2} \text{conv}_\theta(\theta_S, \theta_I), \quad (3.24b)$$

with

$$E_P(\theta_S, \theta_I) = \exp\left(-\frac{\sigma_P^2}{2}\left[\frac{2\pi}{\lambda_S}\sin(\theta_S) + \frac{2\pi}{\lambda_I}\sin(\theta_I)\right]^2\right), \quad (3.25a)$$

$$\Pi(\theta_S, \theta_I, L) = \text{sinc}\left\{\frac{L}{2}\left[k_{zP}(\theta_S, \theta_I) - \frac{2\pi}{\lambda_S}\cos(\theta_S) - \frac{2\pi}{\lambda_I}\cos(\theta_I)\right]\right\}, \quad (3.25b)$$

$$k_{zP}(\theta_S, \theta_I) = \left\{\left(\frac{2\pi}{\lambda_P}\right)^2 - \left[\frac{2\pi}{\lambda_S}\sin(\theta_S) + \frac{2\pi}{\lambda_I}\sin(\theta_I)\right]^2\right\}^{1/2}, \quad (3.25c)$$

$$\begin{aligned} \text{conv}_\theta(\theta_S, \theta_I) = & \text{Re}\left\{\exp\left(i\frac{d}{2}\left[\frac{2\pi}{\lambda_I}\sin(\theta_I)\right]\right)\right. \\ & \times \int_{-\pi/2}^{+\pi/2} d\theta'_I \left[\frac{2\pi}{\lambda_I}\cos(\theta'_I) \exp\left(-i\frac{d}{2}\left[\frac{2\pi}{\lambda_I}\sin(\theta'_I)\right]\right)\right. \\ & \left.\left.\times E_P(\theta_S, \theta'_I) \Pi(\theta_S, \theta'_I, L_B)\right]\right\}. \end{aligned} \quad (3.25d)$$

To reduce the computational effort of numerically solving five integrals to find the image, an alternative expression of the image term is derived by inserting Φ_A and $\Phi_{B\tilde{T}}$ of Eq. (3.23) into the image expression of Eq. (3.17). Thus,

$$\begin{aligned} \int dx_I \Phi_A^* \Phi_{B\tilde{T}} &= 2\pi \iint_{-\pi/2}^{+\pi/2} d\theta_S d\theta_I \iint_{-\pi/2}^{+\pi/2} d\theta'_S d\theta'_I \varphi_A^*(\theta'_S, \theta'_I) \varphi_{B\tilde{T}}(\theta_S, \theta_I) \\ &\times \exp\left(i \left[\frac{2\pi}{\lambda_S} \sin(\theta_S) - \frac{2\pi}{\lambda_S} \sin(\theta'_S) \right] x_S\right) \\ &\times \delta\left(\frac{2\pi}{\lambda_I} \sin(\theta_I) - \frac{2\pi}{\lambda_I} \sin(\theta'_I)\right), \end{aligned} \quad (3.26)$$

where we used

$$\int dx_I \exp\left(i \left[\frac{2\pi}{\lambda_I} \sin(\theta_I) - \frac{2\pi}{\lambda_I} \sin(\theta'_I) \right] x_I\right) = 2\pi \delta\left(\frac{2\pi}{\lambda_I} \sin(\theta_I) - \frac{2\pi}{\lambda_I} \sin(\theta'_I)\right). \quad (3.27)$$

The Dirac delta can be used to analytically solve the integral $\int_{-\pi/2}^{+\pi/2} d\theta'_I$ by noting that

$$\delta\left(\frac{2\pi}{\lambda_I} \sin(\theta_I) - \frac{2\pi}{\lambda_I} \sin(\theta'_I)\right) = \left| \frac{2\pi}{\lambda_I} \cos(\theta_I) \right|^{-1} \delta(\theta'_I - \theta_I). \quad (3.28)$$

Consequently, a compact expression for the image is found, where only three integrals need to be solved numerically,

$$\begin{aligned} \mathcal{I}_{\text{QIUP}}(x_S) &= C'_{\text{AB}} \iint_{-\pi/2}^{+\pi/2} d\theta_S d\theta_I \text{Re} \left\{ \left| \frac{2\pi}{\lambda_I} \cos(\theta_I) \right|^{-1} \varphi_{B\tilde{T}}(\theta_S, \theta_I) \exp\left[i \frac{2\pi}{\lambda_S} \sin(\theta_S) x_S\right] \right. \\ &\quad \left. \times \int_{-\pi/2}^{+\pi/2} d\theta'_S \varphi_A^*(\theta'_S, \theta_I) \exp\left[-i \frac{2\pi}{\lambda_S} \sin(\theta'_S) x_S\right] \right\}. \end{aligned} \quad (3.29)$$

Ultimately, the expressions in the angular domain do not contain any diverging singularities [notice that the term $|(2\pi/\lambda_I) \cos(\theta_I)|^{-1}$ in Eq. (3.29) cancels out with the two $[(2\pi/\lambda_I) \cos(\theta_I)]^{1/2}$ terms in φ_A and $\varphi_{B\tilde{T}}$ of Eq. (3.24)]. The aforementioned expressions are the main analytical findings and will be used in a subsequent section to numerically determine the fundamental resolution of QIUP. Additionally, we study the role of the pump width on the resolution which is essential for experimental implementations.

QIUP with thick and ultra-thin crystals

We present here a numerical example, which is portrayed in Fig. 3.2, to demonstrate the influence of the crystal thickness on the resolution, here both crystals have identical thicknesses $L_A = L_B = L$. The object under study has two slits separated by a distance of $d = 4.5\mu\text{m}$. In this example, the object is illuminated with idler photons of wavelength $\lambda_I = 10\mu\text{m}$ and its image is detected by measuring signal photons of shorter wavelength $\lambda_S = 530\text{nm}$. Therefore, based on energy conservation, the pump has a wavelength of $\lambda_P \approx 503\text{nm}$.

In Fig. 3.2, we showcase two situations: a thick source with $L = 100\mu\text{m}$, which is longer than both signal and idler wavelengths, and an ultra-thin source with $L = 100\text{nm}$, much shorter than the wavelengths. Not only the resulting image $\mathcal{I}_{\text{QIUP}}(x_S)$ is displayed, but also the correlation functions $\varphi_{B\bar{T}}(\theta_S, \theta_I)$, $\Phi_{B\bar{T}}(x_S, x_I)$, $\Phi_A(x_S, x_I)$ that lead to it. Figure 3.2(a) depicts the obtained angular correlation $\varphi_{B\bar{T}}(\theta_S, \theta_I)$ carrying the transmission of the object for sources with thick crystals. We observe that the signal photons cover the range $|\theta_S| \lesssim 1.5^\circ$ and the idler photons $|\theta_I| \lesssim 45^\circ$. Additionally, their correlation is concentrated in a single lobe. In contrast, Fig. 3.2(b) shows that as a result of the use of an ultra-thin crystal, the signal photons are generated within $|\theta_S| \lesssim 3^\circ$ and the idler photons $|\theta_I| \lesssim 90^\circ$. Here, the correlations are found in a central lobe and also in two side lobes.

As mentioned in the previous section, the observed range of signal photons in $\varphi_{B\bar{T}}$ is restricted by two factors: The longitudinal phase matching due to the thickness of the crystal and the maximum range of propagating waves, as presented in section 2.2.1. In particular, we observe that the angular extent of the signal in Fig. 3.2(a) is mainly restricted by the effect of the thick crystal. In contrast, Fig. 3.2(b) shows that as a result of the use of an ultra-thin crystal, where there is a lack of restriction from the longitudinal phase matching, the angular range of signal photons is set by the limit of propagating waves, resulting in $|q_S| \leq 2\pi \min(1/\lambda_S, 1/\lambda_I) \rightarrow |\sin(\theta_S)| \leq \min(1, \lambda_S/\lambda_I) = 530\text{nm}/10\mu\text{m}$, which gives the displayed $\theta_S^{\text{max}} \approx 3^\circ$. Importantly, thanks to the increased signal angular range with the ultra-thin crystal, side lobes appear in the corners of the correlation function in Fig. 3.2(b), which carry information about the distance of the two slits from the probing idler photons to the measured signal photons.

Moreover, Figs. 3.2(c, d) illustrate the corresponding spatial correlation $\Phi_{B\bar{T}}(x_S, x_I)$, where the fact that the object is composed of two slits becomes evident only by using an ultra-thin crystal in Fig. 3.2(d), as two notorious spots appear only in this plot. Furthermore, $\Phi_A(x_S, x_I)$ is shown in Figs. 3.2(e, f), which corresponds to the joint spatial correlation of source A, as it is needed for the calculation of the image. It should be

3 Fundamental resolution limit of two-color quantum imaging

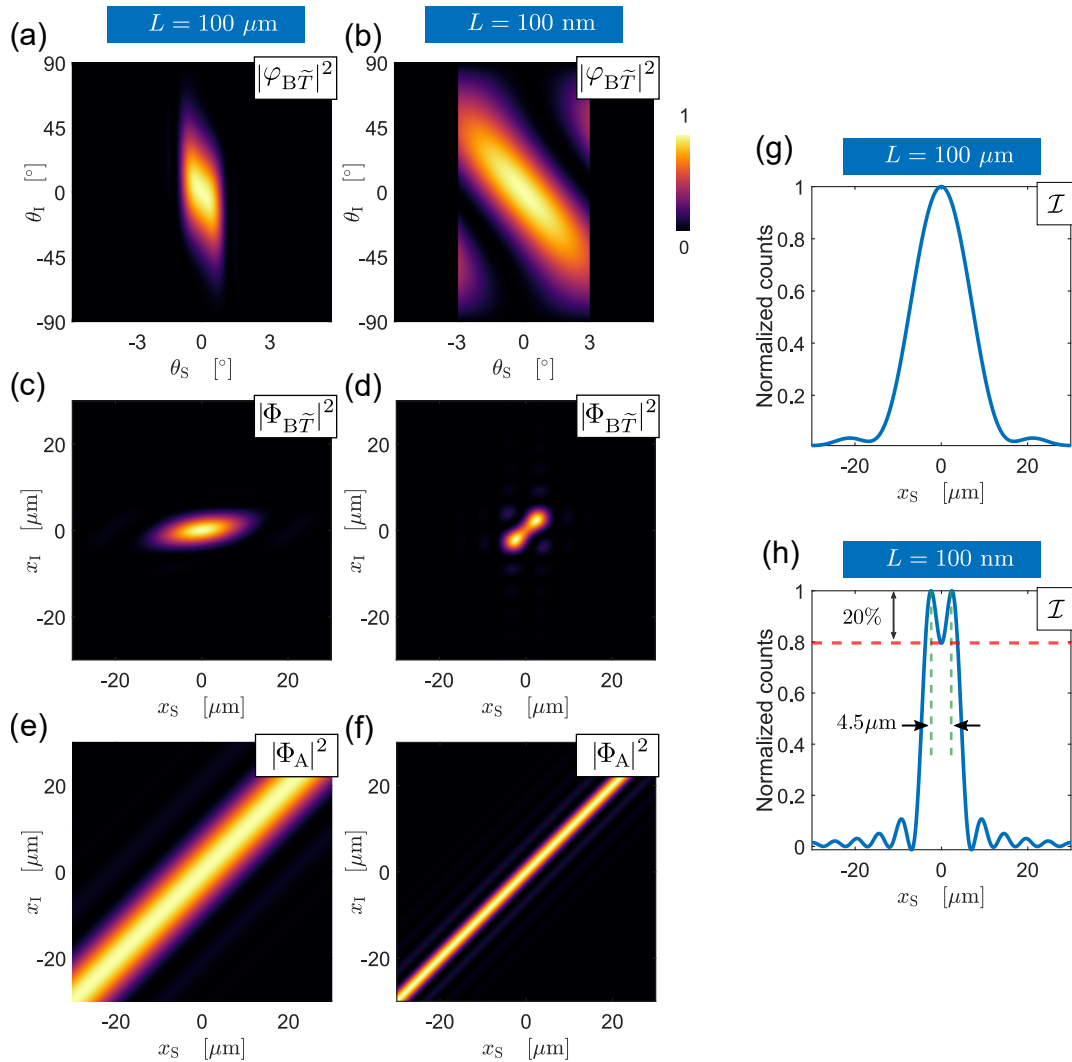


Figure 3.2. (a, b) Angular correlation $|\varphi_{B\tilde{T}}|^2$, (c-f) spatial correlations $|\Phi_{B\tilde{T}}|^2$, $|\Phi_A|^2$ and (g, h) image $\mathcal{I}_{\text{QIUP}}$, using $\lambda_l = 10\mu\text{m}$, $\lambda_s = 530\text{nm}$, plane wave pump, and slits distance $d = 4.5\mu\text{m}$. Crystal thicknesses: (a,c,e,g) $L = 100\mu\text{m}$ and (b,d,f,h) $L = 100\text{nm}$.

mentioned that the plane-wave pump has been approximated with a Gaussian function of 1m width, which allows its numerical implementation.

Finally, the image is found according to Eq. (3.17) by overlapping the position modes $\text{Re}(\Phi_A^* \Phi_{B\tilde{T}})$ and then integrating over x_1 . Figures 3.2(g, h) portray the ensuing image $\mathcal{I}_{\text{QIUP}}(x_s)$. As shown in Fig. 3.2(h), QIUP with ultra-thin SPDC sources is able to resolve such a small distance between the slits, whereas the image of Fig. 3.2(g) produced using thick crystals does not due to the restriction imposed by the longitudinal phase matching.

Fundamental resolution limit of QIUP

The result of the presented numerical example motivates us to find a more precise dependence of the achievable resolution of QIUP on the thickness of the sources of photon pairs. Hence, we follow Rayleigh's criterion and consider that two slits are resolved if their image shows a dip that is at least 20% of the maxima [158]. As a matter of fact, the example presented in Fig. 3.2(h) of two slits separated by $d = 4.5\mu\text{m}$ is exactly at this resolution limit. Therefore, the minimum resolvable distance of the slits with photon-pair wavelengths of $\lambda_I = 10\mu\text{m}$ and $\lambda_S = 530\text{nm}$ is $d_{\min} = 4.5\mu\text{m}$.

In the following analysis, we resort to the derived expression of Eq. (3.29) of the image. As mentioned in the previous section, the use of this expression is computationally less expensive than finding the image using the steps in the numerical example shown before, which were nonetheless useful to illustrate the involved angular and spatial correlations of signal and idler that lead to the image being detected measuring only signal photons. In Fig. 3.3, we depict the minimum resolvable distance d_{\min} that was found numerically for various crystal thicknesses $L = L_A = L_B$, where we consider identical SPDC sources. To find d_{\min} numerically, the distance d between the slits was changed until the image $\mathcal{I}_{\text{QIUP}}$ displayed a 20% dip between the maxima. The blue stars correspond to the case of the example of Fig. 3.2, where the object is illuminated with the longer wavelength of $\lambda_I = 10\mu\text{m}$ and the camera measures signal photons of shorter wavelength $\lambda_S = 530\text{nm}$. The red squares show the situation with

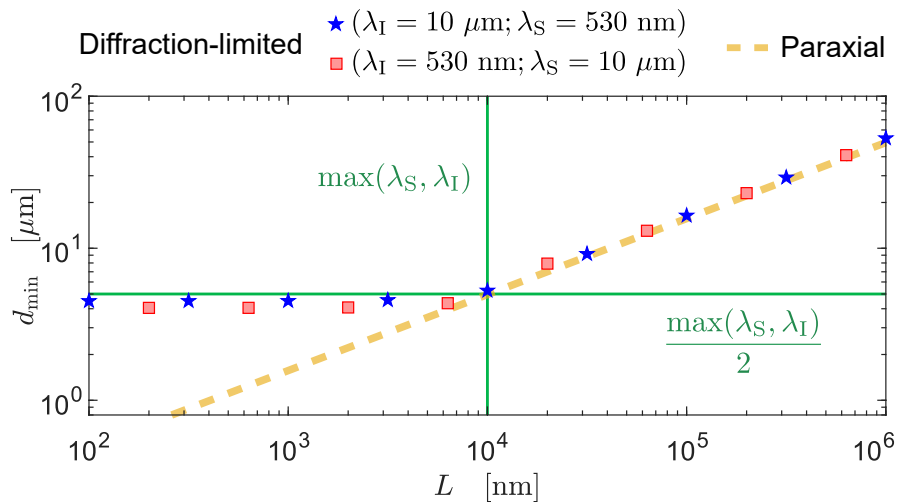


Figure 3.3. Minimum resolvable distance d_{\min} with respect to the crystal thickness $L = L_A = L_B$. The diffraction-limited model, which contemplates all the possible propagating modes, is represented with blue stars and red squares; for the former, the idler wavelength is $\lambda_I = 10\mu\text{m}$ and the signal is $\lambda_S = 530\text{nm}$, for the latter, the wavelengths are reversed. The paraxial estimate of d_{\min} according to Eq. (3.33) is displayed with the yellow dashed line. The green lines are used for comparison; the vertical one marks $\max(\lambda_S, \lambda_I)$ and the horizontal one $\max(\lambda_S, \lambda_I)/2 = 5\mu\text{m}$.

the wavelengths interchanged, $\lambda_I = 530\text{nm}$ for object illumination and $\lambda_S = 10\mu\text{m}$ for detection. Vertical and horizontal green lines are also included as references of the dimensions, one line is at the crystal length of $\max(\lambda_S, \lambda_I)$ and the other is at a minimum resolvable distance of $\max(\lambda_S, \lambda_I)/2 = 5\mu\text{m}$, respectively. Importantly, we can see that the minimum resolvable distance d_{\min} becomes independent of the crystal thickness for $L \lesssim \max(\lambda_S, \lambda_I)$. The reason for this is that the longitudinal phase matching, given by the term $\Pi(\theta_S, \theta_I, L)$ in Eq. (3.25), becomes relaxed by choosing a thinner crystal, i.e., the sinc function within Π tends to a constant. We find here that the only limitation to the resolution is given by the limit of propagating waves when L is smaller than the longer wavelength of the signal and idler photons. Consequently, it is not necessary to use an extremely thin crystal to achieve the fundamental resolution, which has the disadvantage of low generation efficiency, but rather a thicker crystal that has an overall higher efficiency of the SPDC process and still allows us to obtain an image with diffraction-limited resolution.

An ideal plane-wave pump beam cannot be implemented experimentally; hence, we now turn our analysis of the resolution to a more realistic scenario where the pump has a finite width that gives an imperfect signal and idler correlation. We show in Fig. 3.4 the dependence of the minimum resolvable distance d_{\min} on the pump width σ_P while having an ultra-thin crystal of $L = 100\text{nm}$. Remarkably, the resolution remains constant with respect to the pump width. The cause of this outcome is that even though a decrease in the pump width usually entails a decrease of spatial correlation between signal and idler, the use of an ultra-thin crystal guarantees that the degree of spatial correlations remains high even for a pump width equal to the largest wavelength of the photon pair. Therefore, this shows that the diffraction-limited resolution can also be achieved in common experimental situations.

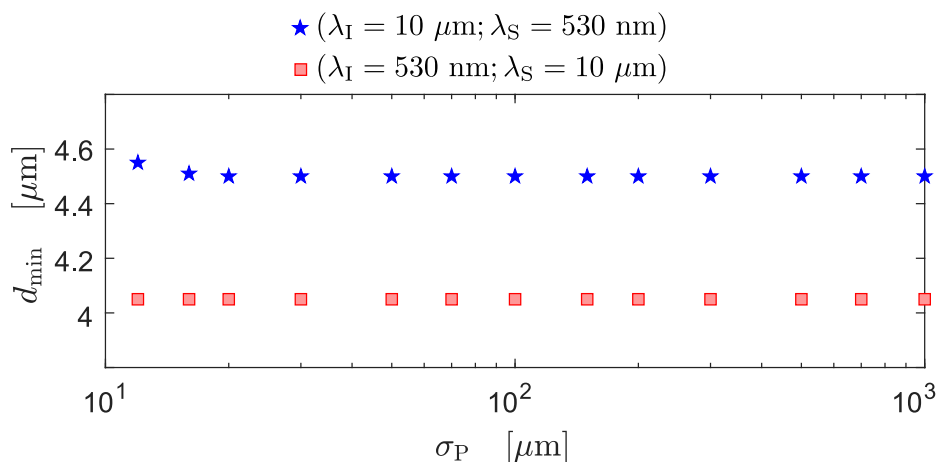


Figure 3.4. Minimum resolvable distance d_{\min} with respect to the pump width σ_P for a crystal thickness of $L = 100 \text{ nm}$.

In both Fig. 3.3 and Fig. 3.4 there is a small difference in the minimum resolvable distance d_{\min} for the two non-degenerate cases in this ultra-thin-crystal regime. To explain this, we calculate d_{\min} for various signal (measured) and idler (undetected) wavelengths, maintaining a crystal thickness of $L = 100\text{nm}$ and a pump width of $\sigma_p = 100\mu\text{m}$, and illustrate the ratio $d_{\min}/\max(\lambda_s, \lambda_I)$ in Fig. 3.5(a). The plot shows the ratio of the minimum resolvable distance and the maximum of the two wavelengths for non-degenerate and degenerate wavelengths. Values have been assigned a color to facilitate visualization. Confirming the previous discussion, we observe in Fig. 3.5(a) that the fundamental minimum resolvable distance d_{\min} is certainly approximately proportional to the larger wavelength, that is, $\max(\lambda_s, \lambda_I)/2$. A more accurate dependence of the resolution on the wavelengths can be derived from Fig. 3.5(a), i.e.,

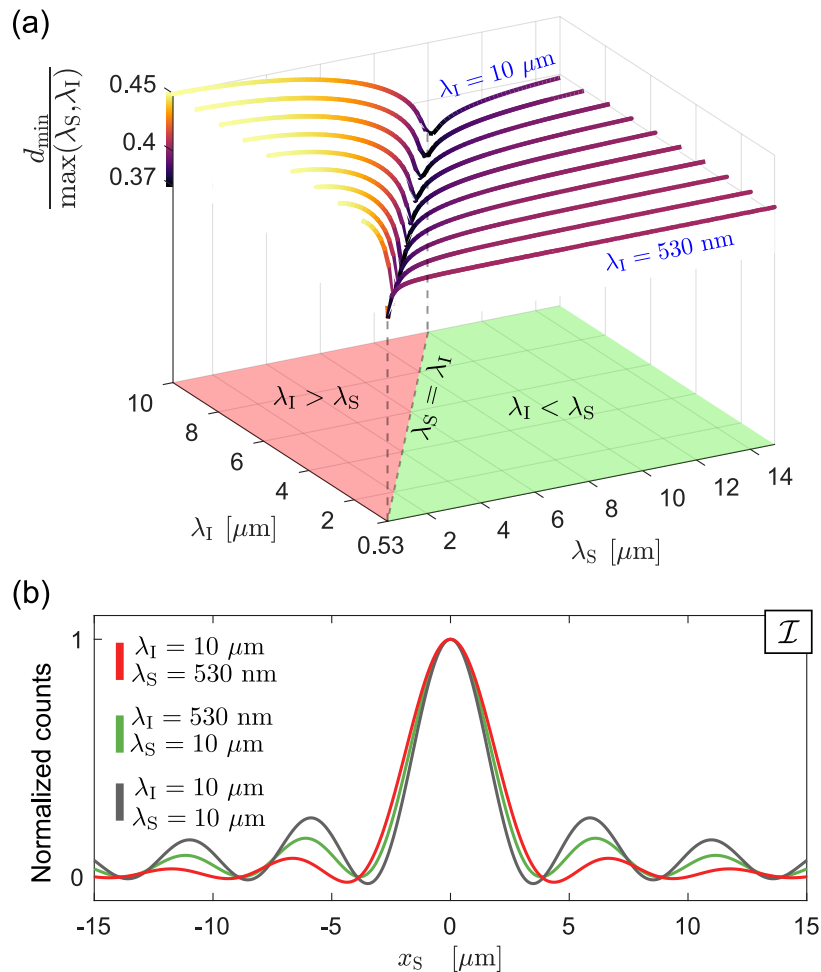


Figure 3.5. (a) Ratio of the minimum resolvable distance d_{\min} and the largest wavelength of the photon pair. Here, the pump width is $\sigma_p = 100 \mu\text{m}$ and the crystal thickness is $L = 100 \text{ nm}$. The minimum of $d_{\min}/\max(\lambda_s, \lambda_I)$ occurs in the degenerate case where $\lambda_s = \lambda_I$. (b) Point-spread-function (PSF) of QIUP with an ultra-thin crystal of $L = 100 \text{ nm}$ for three different wavelength combinations.

there are three relevant regimes of the resolution d_{\min}

$$\frac{d_{\min}}{\max(\lambda_s, \lambda_l)} \approx \begin{cases} 0.45 & \text{if } \lambda_l \gg \lambda_s \\ 0.40 & \text{if } \lambda_l \ll \lambda_s \\ 0.37 & \text{if } \lambda_l = \lambda_s \end{cases} \quad (3.30)$$

From this expression, d_{\min} has a minimum in the degenerate case $\lambda_s = \lambda_l$, where there is a slight enhanced resolution compared to the resolution in the non-degenerate cases. The reason for this difference in resolution can be understood by analyzing the respective point-spread-functions (PSF), which is slightly different depending on the choice of wavelengths. The PSF is found by taking a centered single slit with infinitesimal width as the object. Figure 3.5(b) displays the PSF for the three regimes showing that there is a slight difference in the width of the central lobes. In the case of $\lambda_l \gg \lambda_s$, the main lobe is broader and the side lobes are small, for $\lambda_l \ll \lambda_s$ the central lobe becomes narrower with higher side lobes, and for the degenerate case $\lambda_l = \lambda_s$, the main lobe is the narrowest but the side lobes are the most distinct of the three cases. Considering that the Rayleigh criterion is based only on the main lobe of the image to find the minimum resolvable distance between two point-like objects, the degenerate case does result in a smaller d_{\min} . However, a narrower central lobe in the image $\mathcal{I}_{\text{QIUP}}(x_s)$ comes at the expense of having undesirable taller side lobes. This effect of enhanced resolution by shaping a diffraction-limited PSF has also been studied in classical optics [187, 188], namely, called optical superoscillation. In this classical technique, the central and side lobes of the PSF are carefully designed to achieve resolution beyond the diffraction limit of $\lambda/2$. QIUP with ultra-thin crystal, as has been shown here, is characterized by a wavelength-dependent PSF that presents mild changes to the width and intensity of its central and side lobes; therefore, it shows a subtle improvement over the diffraction limit of $\max(\lambda_s, \lambda_l)/2$.

In summary, there are two main findings regarding the resolution of QIUP. First, the image of the QIUP scheme with ultra-thin crystals is limited in the q -space by the diffraction of the longer wavelength, namely $|q_s| \leq 2\pi \min(1/\lambda_s, 1/\lambda_l)$ as was shown in Eq. (3.21). Second, this fundamental limit in the q -space leads to a resolution of $d_{\min} \approx \max(\lambda_s, \lambda_l)/2$, where a more precise value depends on the combination of specific wavelengths, as shown in Eq. (3.30).

Resolution in the paraxial regime

The fundamental resolution d_{\min} was found numerically, since analytical expressions for the position correlations $\Phi_{B\tilde{T}}$, Φ_A , or the image $\mathcal{I}_{\text{QIUP}}$ cannot be readily calculated

using the complete non-paraxial model. Nonetheless, a closed-form expression for the resolution can be obtained for the regime where all the transverse momenta are small, i.e., in the so-called paraxial regime. As already discussed, thick crystals produce signal and idler photons with such small transverse momenta. Therefore, the state's correlation function of Eq. (2.21) and Eq. (3.20) can be considerably simplified to find an analytical expression for the minimum resolvable distance. The simplifications are the following: First, we make use of the paraxial approximation where $k_z = \sqrt{k^2 - q^2} \approx k - q^2/(2k)$. Second, the main lobe of the sinc-function is approximated to a Gaussian [167, 189] $\text{sinc}(x^2) \approx \exp(-4\gamma x^2)$, where $\gamma = 0.2$ ensures that the main lobe of the sinc and the Gaussian coincide at 0.1 in amplitude. Third, in the paraxial approximation, the terms $\kappa^{-1/2}$ and $k_z^{-1/2}$ become independent of the transverse momentum q [170], and the rectangular functions take an infinite width. Using all these simplifications, the convolution term in $\Phi_{B\tilde{T}}$ becomes

$$\begin{aligned} & [(k_{zI})^{1/2} \phi_B(q_S, q_I)] \otimes \widetilde{(T^*)}(q_I) \\ &= C_{\otimes} \cos\left[\frac{d}{2}(q_S + q_I)\right] \exp\left[-\gamma L_B(\lambda_S + \lambda_I) \frac{q_S^2}{2\pi}\right], \end{aligned} \quad (3.31)$$

Consequently, the position correlations of Eq. (3.15) are then approximated to

$$\begin{aligned} \Phi_{B\tilde{T}} &= C_{B\tilde{T}} \exp\left[-\pi \frac{(x_S + \frac{d}{2})^2}{2\gamma L_B(\lambda_S + \lambda_I)}\right] \delta\left(x_I + \frac{d}{2}\right) \\ &+ C_{B\tilde{T}} \exp\left[-\pi \frac{(x_S - \frac{d}{2})^2}{2\gamma L_B(\lambda_S + \lambda_I)}\right] \delta\left(x_I - \frac{d}{2}\right), \end{aligned} \quad (3.32a)$$

$$\Phi_A = C_A \exp\left[-\pi \frac{(x_S - x_I)^2}{2\gamma L_A(\lambda_S + \lambda_I)}\right], \quad (3.32b)$$

where C is a constant. Following the same treatment as in the non-paraxial case, the image \mathcal{I}_{QIUP} is found according to Eq. (3.17) and the minimum resolvable distance can then be analytically calculated considering that at $d_{\min}^{(\text{paraxial})}$, the image at $x_S = 0$ is $\mathcal{I}_{QIUP} = 0.8$, i.e., a 20% dip between the maxima. Thus,

$$d_{\min}^{(\text{paraxial})} \approx 0.7(\lambda_S + \lambda_I)^{1/2} \left(\frac{1}{L_A} + \frac{1}{L_B}\right)^{-1/2}. \quad (3.33)$$

This expression of the resolution in the paraxial regime depends on the crystals thickness and both signal and idler wavelengths. Therefore, this closed form of $d_{\min}^{(\text{paraxial})}$ gives a physical intuition for the resolution. Specifically, for the case of identical

sources with $L = L_A = L_B$, as found in Refs. [164, 165], $d_{\min} \propto [L(\lambda_s + \lambda_l)]^{1/2}$, showing not only that thinner crystals can improve the resolution, but also that the resolution is independent of whether the illuminating idler wavelength λ_l is larger than the detected signal wavelength λ_s , or vice versa, as described with the sum of the two wavelengths. It is important to emphasize that $d_{\min}^{(\text{paraxial})}$ incorrectly describes the transverse resolution with ultra-thin crystals. To illustrate this, the paraxial prediction of resolution is displayed with a yellow dashed line in Fig. 3.3. Essentially, the naive use of the paraxial expression for the regime with ultra-thin crystals leads to the erroneous conclusion of having ‘super-resolution’ beyond the diffraction limit. Thus, the paraxial expression gives insight only in the regime with thick crystals where $L \gtrsim \max(\lambda_s, \lambda_l)$.

As a final remark, Eq. (3.33) shows that distinguishable sources have an impact on the resolution $d_{\min}^{(\text{paraxial})}$. That is, when the crystals have different thicknesses $L_A \neq L_B$ the resolution is reduced. The reason for this reduction can be understood with an example. Consider that L_A has a fixed value $L_A = L$ and $L_B > L$, therefore, the term $(1/L_A + 1/L_B)^{-1/2}$ results in $(1/L + 1/L_B)^{-1/2}$, which is larger than $(2/L)^{-1/2}$ obtained when the crystals are identical $L_A = L_B = L$. The reduction of resolution can be attributed to the imperfect overlap of the position modes due to the distinguishability of the sources.

3.1.2. Discussion

The discussed fundamental resolution limit is, in essence, the consequence of free-space propagation, which limits the range of transverse momenta of the signal and idler photons. We showed that the largest range of transverse momenta of the image is set by the longer wavelength from the photon pair because of transverse momentum conservation. This was described by the term $\text{rect}[|q_s| \leq 2\pi \min(1/\lambda_s, 1/\lambda_l)]$ in Eq. (3.20). Moreover, we showed that the thickness of the crystals plays a prominent role in the resolution, since a thickness comparable or smaller than either of the signal and idler wavelengths allows one to reach the diffraction-limited resolution shown in Eq. (3.30). This is possible due to the lack of restriction from the phase-matching condition in a thin source, therefore, allowing one to generate the largest possible range of transverse wave-vectors, which consequently enables the resolution to reach the diffraction limit. Photon-pair generation in such ultra-thin sources has been demonstrated recently in ultra-thin nonlinear films [83, 84] and also in thin metasurfaces [86]. Recent work in our group has shown that a form of QIUP can be used to achieve resolution beyond the mentioned diffraction limit if the imaging process involves evanescent waves; see Refs. [172, 190]. In such a case, near-field

interactions of an absorptive particle at the idler wavelength are used to influence the field of its paired signal wavelength, which allows us to obtain a sub-diffraction image with undetected photons. Nevertheless, QIUP involving only far-field interactions is limited by the diffraction limit of the longer wavelength of the photon pair, as discussed in this chapter.

Although the presented analysis focuses on QIUP based on position correlations, we infer that it is likely that a similar fundamental resolution limit applies to the QIUP scheme based on momentum correlations, since the change of the optical elements cannot affect the limited range of transverse momenta of propagating photons. To this day, the minimum resolvable distance of the QIUP scheme based on momentum correlations has been treated only within the paraxial regime in other works [151, 163], this being $d_{\min}^{(\text{paraxial})} \propto \lambda_I/\sigma_p$, with σ_p as the transverse width of the pump. Therefore, the larger the pump, the better the resolution. The limit of the validity of this paraxial description can be found by analyzing the extreme case where the pump is a plane wave $\sigma_p \rightarrow \infty$, where signal and idler photons have a perfect correlation in momentum. In such a case, the paraxial expression of the resolution is $d_{\min}^{(\text{paraxial})} \rightarrow 0$. Such a perfect resolution is physically impossible, as has been shown in this chapter, due to the diffraction limit of the longer wavelength of the photon pair, which would then define a lower bound to the minimum resolvable distance. The paraxial approximation of the resolution of QIUP based on momentum correlations, which does not consider the diffraction limit, breaks down for pump widths that are much larger than the wavelengths.

Beyond QIUP, it was presented in chapter 2 that QGI relies also on the angular- and position correlations of signal and idler photons. These correlations should be similar to the ones depicted in Fig. 3.2, therefore, the fundamental resolution of QGI should be also similarly defined by the larger wavelength of the photon pair, as found for QIUP. This hypothesis is analyzed in the following section.

3.2. Quantum ghost imaging

Similar to the resolution investigation of the QIUP scheme, here we derive the fundamental transverse resolution of QGI. The scheme is illustrated in Fig. 3.6 and consists of a single nonlinear crystal. A pump beam impinges the crystal to produce signal and idler photons that are then spatially separated, e.g., with a dichroic mirror. The idler photons interact with the object and are then measured by a detector that collects all photons and lacks from spatial resolution, this is commonly called ‘bucket’ detector. The signal photons do not interact with the object and are measured by a spatially

3 Fundamental resolution limit of two-color quantum imaging

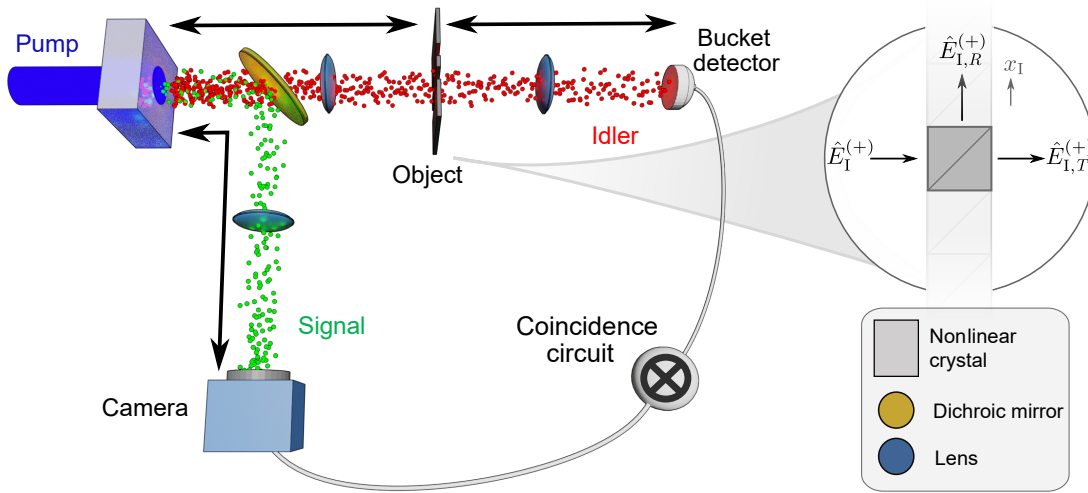


Figure 3.6. Sketch of quantum ghost imaging (QGI) based on position correlations. In the idler arm, the central plane of the crystal is imaged to the object plane by a system with magnification one (represented by the black arrow), then the object plane is imaged with the same system onto the plane of the bucket detector. In the signal arm, the central plane of the crystal is also imaged of the crystal to the plane of the camera. Inset: model of the object composed of a beamsplitter in each x_1 position.

resolving detector, i.e., a camera. Unlike the QIUP scheme, the information on the transverse profile of the object is found in the coincidence counts of the two detectors, while the detection of each detector alone does not reveal the transverse profile of the object. In this analysis, we exploit the position correlations of signal and idler photons. Consequently, in the idler arm, the central plane of the crystal is imaged onto the object with an optical system with magnification equal to one, denoted with the black double-sided arrow. Then the object plane is imaged onto the plane of the bucket detector by an equal optical system of magnification one. Finally, in the signal arm, the central plane of the crystal is imaged onto the camera in the same manner.

To derive the resolution, we start by modeling the QGI scheme. The two-photon state produced by the source, as discussed in chapter 2, is given by

$$|\psi\rangle = C_\psi \iint dq_s dq_I \phi(q_s; q_I) \hat{a}^\dagger(q_s) \hat{a}^\dagger(q_I) |0, 0\rangle. \quad (3.34)$$

As in the QIUP scheme, the object is modeled by a beamsplitter with transmission $T(x_1)$ and reflection $R(x_1)$ at each position x_1 . In the inset of Fig. 3.6 it is shown that one of the inputs of the beamsplitter is $\hat{E}_I^{(+)}(x_1)$, the transmitted output is $\hat{E}_{I,T}^{(+)}(x_1)$, and the reflected output is $\hat{E}_{I,R}^{(+)}(x_1)$. The input can be formulated in terms of the two outputs by [184]

$$\hat{E}_I^{(+)}(x_1) = T^*(x_1) \hat{E}_{I,T}^{(+)}(x_1) + R^*(x_1) \hat{E}_{I,R}^{(+)}(x_1). \quad (3.35)$$

Introducing the electric field of Eq. (3.4) and the Fourier transform of the transmission and reflection into Eq. (3.35), we find the relation between the idler modes to be

$$\begin{aligned} & \hat{a}_I(q_I)(k_{zI})^{-1/2} \text{rect}\left(|q_I| \leq \frac{2\pi}{\lambda_I}\right) \\ &= -\frac{1}{2\pi} \int dq'_I \left[\tilde{T}^*(-q_I + q'_I) \hat{a}_{I,T}(q'_I) + \tilde{R}^*(-q_I + q'_I) \hat{a}_{I,R}(q'_I) \right] (k'_{zI})^{-1/2} \text{rect}\left(|q'_I| \leq \frac{2\pi}{\lambda_I}\right). \end{aligned} \quad (3.36)$$

Introducing Eq. (3.36) into the two-photon quantum state, we obtain

$$\begin{aligned} |\psi\rangle &= C'_\psi \iint dq_S dq_I \left\{ \phi(q_S; q_I) (k_{zI})^{1/2} \right. \\ &\quad \times \left[\int dq'_I \tilde{T}(-q_I + q'_I) (k'_{zI})^{-1/2} \text{rect}\left(|q'_I| \leq \frac{2\pi}{\lambda_I}\right) \hat{a}_{I,T}^\dagger(q'_I) \right] \hat{a}_S^\dagger(q_S) |0, 0\rangle \left. \right\} \\ &+ C'_\psi \iint dq_S dq_I \left\{ \phi(q_S; q_I) (k_{zI})^{1/2} \right. \\ &\quad \times \left[\int dq'_I \tilde{R}(-q_I + q'_I) (k'_{zI})^{-1/2} \text{rect}\left(|q'_I| \leq \frac{2\pi}{\lambda_I}\right) \hat{a}_{I,R}^\dagger(q'_I) \right] \hat{a}_S^\dagger(q_S) |0, 0\rangle \left. \right\}. \end{aligned} \quad (3.37)$$

Then, rearranging the integrals of q_I and q'_I the state becomes

$$\begin{aligned} |\psi\rangle &= C''_\psi \iint dq_S dq'_I \left\{ (k'_{zI})^{-1/2} \left[\int dq_I (k_{zI})^{1/2} \phi(q_S; q_I) \tilde{T}(-q_I + q'_I) \right] \right. \\ &\quad \times \text{rect}\left(|q'_I| \leq \frac{2\pi}{\lambda_I}\right) \hat{a}_{I,T}^\dagger(q'_I) \hat{a}_S^\dagger(q_S) |0, 0\rangle \left. \right\} \\ &+ C''_\psi \iint dq_S dq'_I \left\{ (k'_{zI})^{-1/2} \left[\int dq_I (k_{zI})^{1/2} \phi(q_S; q_I) \tilde{R}(-q_I + q'_I) \right] \right. \\ &\quad \times \text{rect}\left(|q'_I| \leq \frac{2\pi}{\lambda_I}\right) \hat{a}_{I,R}^\dagger(q'_I) \hat{a}_S^\dagger(q_S) |0, 0\rangle \left. \right\}, \end{aligned} \quad (3.38)$$

where the terms within the square brackets are convolutions along q'_I . The term with the transmission is then

$$\left[(k'_{zI})^{1/2} \phi(q_S, q'_I) \right] \otimes \tilde{T}(q'_I) = \int dq_I (k_{zI})^{1/2} \phi(q_S; q_I) \tilde{T}(-q_I + q'_I), \quad (3.39)$$

and similarly for the term with the reflection.

Before finding the ghost image, we first assume that both detectors are spatially resolving and calculate the coincidence counting rate [185], which we will call here

the joint spatial probability (JSP), given by

$$\text{JSP}(x_S, x_I) \propto \langle \psi |_{\text{SPDC}} \hat{E}_{I,\text{det}}^{(-)} \hat{E}_{S,\text{det}}^{(-)} \hat{E}_{S,\text{det}}^{(+)} \hat{E}_{I,\text{det}}^{(+)} | \psi \rangle_{\text{SPDC}}, \quad (3.40)$$

where the SPDC state is $|\psi\rangle_{\text{SPDC}} = |0, 0\rangle + |\psi\rangle$, as shown in Eq. (2.1), which includes the two-photon state $|\psi\rangle$ of Eq. (3.38). Here, the electric field operators at the detectors are

$$\hat{E}_{S,\text{det}}^{(+)}(x_S) = C \int dq_S \exp(iq_S x_S) (k_{zS})^{-1/2} \text{rect}\left(|q_S| \leq \frac{2\pi}{\lambda_S}\right) \hat{a}_S(q_S), \quad (3.41a)$$

$$\hat{E}_{I,\text{det}}^{(+)}(x_I) = C \int dq'_I \exp(iq'_I x_I) (k'_{zI})^{-1/2} \text{rect}\left(|q'_I| \leq \frac{2\pi}{\lambda_I}\right) \hat{a}_{I,T}(q'_I). \quad (3.41b)$$

Thus, the JSP results in

$$\begin{aligned} \text{JSP}(x_S, x_I) = C_{\text{JSP}} & \left| \iint dq_I dq_S \exp(iq_S x_S + iq_I x_I) (k_{zS})^{-1/2} (k_{zI})^{-1} \right. \\ & \left. \times \text{conv}(q_S, q_I) \text{rect}\left(|q_I| \leq \frac{2\pi}{\lambda_I}\right) \text{rect}\left(|q_S| \leq \frac{2\pi}{\lambda_S}\right) \right|^2, \end{aligned} \quad (3.42)$$

with the convolution term that includes the transmission, namely,

$$\text{conv}(q_S, q_I) = [(k_{zI})^{1/2} \phi(q_S, q_I)] \otimes \tilde{T}(q_I). \quad (3.43)$$

Afterwards, the quantum ghost image \mathcal{I}_{QGI} is found taking into account that the bucket detector collects all incoming photons without spatial resolution, which is achieved by integrating the JSP over a large transverse range of x_I

$$\mathcal{I}_{\text{QGI}}(x_S) = C_{\text{JSP}} \int dx_I \text{JSP}(x_S, x_I). \quad (3.44)$$

3.2.1. Fundamental resolution of QGI

To illustrate that the object's transmission appears in the ghost image \mathcal{I}_{QGI} and later find its fundamental resolution limit, we show an example with two infinitely thin slits separated by a distance d , similar to the analysis for the QIUP scheme.

This double slit object has a transmission given by Eq. (3.18), which results in the convolution term $\text{conv}(q_S, q_I)$ inside the JSP being identical to the one derived in the context of QIUP, see Eqs. (3.19) and (3.20). Therefore, this important result confirms our hypothesis that the ghost image $\mathcal{I}_{\text{QGI}}(x_S)$ also exhibits a hard limit of the available transverse momenta set by the larger wavelength between signal and idler, which is given by $\text{rect}[|q_S| \leq 2\pi \min(1/\lambda_S, 1/\lambda_I)]$.

Finally, we proceed to find the minimum resolvable distance d_{\min} of QGI. To this end, the JSP of Eq. (3.42) needs to be written in the angular domain to avoid the terms $(k_{z_s})^{-1/2}(k_{z_l})^{-1}$ diverging when $q \rightarrow 2\pi/\lambda$. Using $q = (2\pi/\lambda)\sin(\theta)$, $k_z = (2\pi/\lambda)\cos(\theta)$ and $dq = k_z d\theta$, the JSP becomes

$$\text{JSP}(x_s, x_l) = C_{\text{JSP}} \left| \iint_{-\pi/2}^{+\pi/2} d\theta_l d\theta_s \varphi(\theta_s, \theta_l) \exp \left[i \frac{2\pi}{\lambda_s} \sin(\theta_s) x_s + i \frac{2\pi}{\lambda_l} \sin(\theta_l) x_l \right] \right|^2, \quad (3.45)$$

with $\varphi(\theta_s, \theta_l) = \text{conv}_\theta(\theta_s, \theta_l)$, where the conv_θ term was presented in Eq. (3.25d) in the analysis of QIUP. To further draw parallels between QGI and QIUP, a numerical example for QGI is illustrated in Fig. 3.7 under similar conditions as the numerical example of QIUP in Fig. 3.2. We use an ultra-thin photon-pair source of thickness $L = 100\text{nm}$, idler photons with a wavelength of $\lambda_l = 10\mu\text{m}$ signal photons of shorter wavelength $\lambda_s = 530\text{nm}$, pump width of $100\mu\text{m}$, and the object slits separated by a distance of $d = 4.12\mu\text{m}$. Figure 3.7(a) portrays the angular correlation given by $\varphi(\theta_s, \theta_l)$ using Eq. (3.25d). Subsequently, the $\text{JSP}(x_s, x_l)$ is found using φ in Eq. (3.45), see Fig. 3.7(b). Lastly, assuming that the bucket detector collects all idler photons, the ghost image \mathcal{I}_{QGI} is derived from the JSP using Eq. (3.44), see Fig. 3.7(c). The angular correlation φ of Fig. 3.7(a) shows that the angular range of idler photons is $|\theta_l| \leq 90^\circ$ while the signal photons are restricted by the found relation $|\sin(\theta_s)| \leq \min(1, \lambda_s/\lambda_l) = 530\text{nm}/10\mu\text{m}$, which results in $\theta_s^{\max} \approx \pm 3^\circ$. Additionally, we observe here a central lobe and partial side lobes of high correlation probability, which contain information to find the distance between the two slits. This is confirmed in the JSP of Fig. 3.7(b) as two distinctive spots can be observed which correspond to the presence of two slits. Finally, the ghost image \mathcal{I}_{QGI} in Fig. 3.7(c) shows that the transverse profile of the object's transmission can be obtained. Moreover, \mathcal{I}_{QGI} illustrates that the slits are at the resolution limit since there is a 20% dip from the maxima following the Rayleigh criterion.

Further numerical tests with other combinations of wavelengths for signal and idler, just as the ones carried out for QIUP, show that the minimum resolvable distance can be put in three cases given that the point spread functions vary with the combination of wavelengths, leading to

$$\frac{d_{\min}}{\max(\lambda_s, \lambda_l)} \approx \begin{cases} 0.41 & \text{if } \lambda_l \gg \lambda_s \\ 0.39 & \text{if } \lambda_l \ll \lambda_s \\ 0.37 & \text{if } \lambda_l = \lambda_s \end{cases}. \quad (3.46)$$

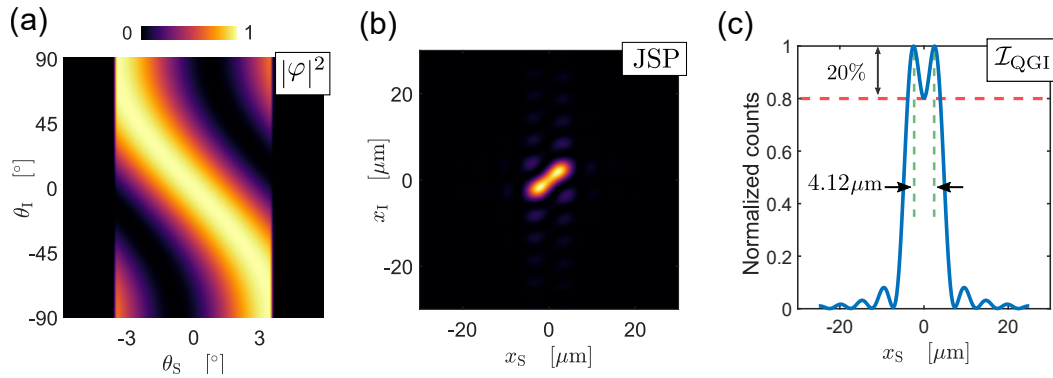


Figure 3.7. (a) Angular correlation $|\varphi|^2$, (b) joint spatial probability JSP and (c) image \mathcal{I}_{QGI} , assuming a crystal thickness $L = 100\text{nm}$, $\lambda_i = 10\mu\text{m}$, $\lambda_s = 530\text{nm}$, pump width $\sigma_p = 100\mu\text{m}$, and slits distance $d = 4.12\mu\text{m}$.

The minimum resolvable distance d_{min} of QGI is slightly smaller than the d_{min} found for QIUP; this difference can be understood from the angular correlations involved. For QIUP, the angular correlation $\varphi_{\text{B}\tilde{T}}$ shows a damping of idler modes for large angles as given by the term $[(2\pi/\lambda_i) \cos \theta_1]^{1/2}$ in Eq. (3.24) and seen in Fig. 3.2(b). However, for QGI, the mentioned term does not appear in the angular correlation φ , therefore, φ extends with high probability over the whole idler range, as can be seen in Fig. 3.7(a). Since modes with large angles are responsible for higher resolution, QGI shows slightly better d_{min} than QIUP.

3.2.2. Discussion

The main difference between QGI and QIUP is that QGI consists of only one source of photon pairs and the image is obtained in coincidences, whereas QIUP relies only on single-photon measurements. Here, we have shown that these quantum imaging schemes share the same fundamental transverse resolution limit, which is defined by the larger wavelength of the photon pair. This result disagrees with Ref. [191], which claims that QGI can have a resolution much smaller than the illuminating wavelength owed only to a very large non-degeneracy of photons. Lastly, since analogue classical schemes of ghost imaging [95, 97, 144, 192–194] and imaging with undetected light [195] are also restricted by free-space propagation, it can be concluded that their diffraction-limited resolution will also be limited by the longer wavelength.

3.3. Abstract and publication

A theoretical framework for QIUP and QGI based on position correlations was presented in this chapter. In particular, the schemes were modeled using a formalism

developed for treating the non-paraxial regime of operation. This non-paraxial approach was used to find the minimum resolvable distance d_{\min} of two infinitesimal slits in QIUP and QGI. The diffraction-limited resolution was found to be defined by the longer wavelength of the photon pair $d_{\min}^{(\text{limit})} \approx \max(\lambda_s, \lambda_l)/2$. This resolution can be achieved using crystals with thicknesses smaller than the longest wavelength.

The study and results of this chapter were presented at a conference [196] and also have been published in Physical Review Research [180] along with the non-paraxial quantum state of photon pairs, see chapter 2, that was derived by Elkin A. Santos.

4. Lensless quantum ghost imaging

Imaging becomes a cumbersome task to achieve at wavelength ranges where lenses are less available, for example, in the infrared and terahertz ranges, which are important in fields such as biology and material science [121]. In this case, alternative imaging schemes that do not rely on lenses need to be considered. Lensless classical imaging can be achieved, for example, using the principle of pinhole imaging [197, 198]. In a pinhole camera, the object is located on one side of an opaque screen with a small pinhole, whereas the detector is on the other side. The scheme does not need any lenses to capture the shadow of the object¹, which can be optimized by adapting the pinhole size [197]. The pinhole camera does not offer high resolution, but this type of lensless imaging has several advantages over imaging with lenses, i.e., a larger depth of field, a wide angular field of view [198], and its applicability in wavelength ranges for which high-quality lenses are less available [199, 200].

In quantum ghost imaging (QGI), lenses are usually placed in the path of the signal and/or idler [90, 106, 107] to form a ghost image or in the pump-beam path before the beam impinges onto the crystal [125]. The lenses introduce a parabolic phase front in either beam path, which results in the formation of a ghost image in the coincidences measurement. However, it has been shown that QGI can also be realized without lenses, which is advantageous for down-converted photons in the terahertz range [201], by adding a parabolic phase front by engineering the nonlinearity profile of the nonlinear crystal, for example, using a nonlinear photonic crystal [202]. Additionally, since ghost imaging can be also realized with classical light [95, 97, 144, 192–194], which has the inherent property of acting as a phase-conjugated mirror [193], a ghost imaging scheme can also be used for lensless imaging [203, 204]. Moreover, a pinhole-based scheme for ghost imaging with thermal light has already been proposed [205], where the optimal lensless imaging condition depends on the size of the thermal source. However, in this chapter, we extend this approach of lensless imaging to the quantum regime with entangled photons. In our approach, a nonlinear crystal generating photon pairs is illuminated by a collimated pump beam and, contrary to ghost imaging with thermal light, we use a bucket detector that collects all the probing

¹ We will refer to this shadow as an image although strictly no imaging is taking place.

idler photons instead of a point detector behind the object, which just collects a small amount of idler photons.

We begin by presenting the original quantum ghost diffraction scheme; then, this will serve as a starting point to investigate the novel lensless QGI scheme that we name ‘pinhole QGI’. We perform numerical examples, and later we derive a simplified analytical model that generalizes the numerical observations and allows us to find a connection to a classical pinhole camera. We show that pinhole QGI can be realized for specific pump beam diameters in an optimum regime of operation, and we analyze its properties.

4.1. Quantum ghost diffraction

Based on the analysis presented in chapter 3, we model here a quantum ghost diffraction (QGD) scheme, which is used to obtain the diffraction pattern of an object instead of its image as shown previously. The QGD scheme is illustrated in Fig. 4.1. A collimated pump impinges on a nonlinear crystal producing photon pairs that are separated using a dichroic mirror. After a distance z_s , a spatially resolving detector, i.e., a camera, is used to measure signal photons. In the idler arm, an object is placed at a distance z_o from the crystal and then the idler photons propagate a distance $z_I - z_o$ until reaching a non-resolving detector of small transverse size. This scheme allows us to obtain the diffraction pattern of the object in the coincidence counts without the

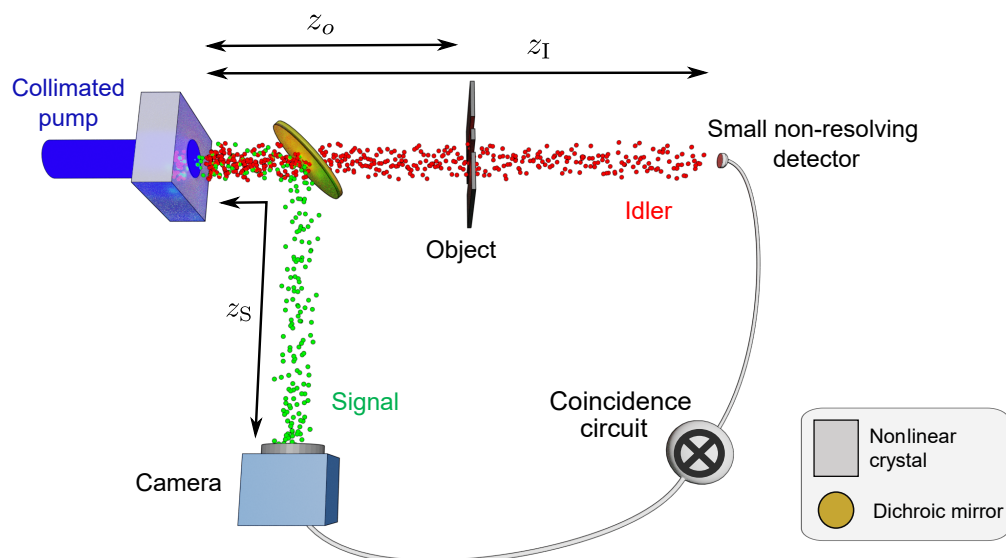


Figure 4.1. Sketch of a quantum ghost diffraction (QGD) scheme. The difference with QGI, presented in the previous chapters, is that there are no lenses in the down-converted arms and the non-resolving detector behind the object has a very small transverse size.

need of any lenses in the signal and idler arms, as just described.

We start by modeling the QGD scheme with the two-photon quantum state presented in the previous chapter in Eq. (3.34). Afterwards, the quantum state at different planes in the scheme can be found using classical propagation in the Fourier domain for both signal and idler photons [206]. In detail, the phase term $\exp(ik_{z_I}z_o)$ models the propagation of the idler photons from the crystal to the plane of the object and $\exp(ik_{z_S}z_S)$ represents the propagation of the signal photons from the crystal to the camera, leading to a state

$$|\psi\rangle = C_\psi \iint dq_S dq_I \phi(q_S; q_I) \exp(ik_{z_I}z_o) \exp(ik_{z_S}z_S) \hat{a}^\dagger(q_S) \hat{a}^\dagger(q_I) |0, 0\rangle, \quad (4.1)$$

where C_ψ denotes a constant. The object is modeled as a beamsplitter with a transmission $T(x_I)$ and a reflection $R(x_I)$ that connects the idler operator of the output with the inputs by Eqs. (3.35) and (3.36), resulting in the state

$$\begin{aligned} |\psi\rangle = & C'_\psi \iint dq_S dq_I \left\{ \phi(q_S; q_I) \exp(ik_{z_I}z_o) \exp(ik_{z_S}z_S) (k_{z_I})^{1/2} \right. \\ & \times \left[\int dq'_I \tilde{T}(-q_I + q'_I) (k'_{z_I})^{-1/2} \text{rect}\left(|q'_I| \leq \frac{2\pi}{\lambda_I}\right) \hat{a}^\dagger_{I,T}(q'_I) \right] \hat{a}^\dagger_S(q_S) |0, 0\rangle \left. \right\} \\ & + C'_\psi \iint dq_S dq_I \left\{ \phi(q_S; q_I) \exp(ik_{z_I}z_o) \exp(ik_{z_S}z_S) (k_{z_I})^{1/2} \right. \\ & \times \left[\int dq'_I \tilde{R}(-q_I + q'_I) (k'_{z_I})^{-1/2} \text{rect}\left(|q'_I| \leq \frac{2\pi}{\lambda_I}\right) \hat{a}^\dagger_{I,R}(q'_I) \right] \hat{a}^\dagger_S(q_S) |0, 0\rangle \left. \right\}. \end{aligned} \quad (4.2)$$

Next, the propagation of the idler photons from the plane of the object to the plane of the non-resolving detector is taken into account with the phase term $\exp[ik'_{z_I}(z_I - z_o)]$ into the state and the integrals of q_I and q'_I are reordered, leading to

$$\begin{aligned} |\psi\rangle = & C'_\psi \iint dq_S dq'_I \left\{ \exp(ik_{z_S}z_S) (k'_{z_I})^{-1/2} \left[\int dq_I (k_{z_I})^{1/2} \phi(q_S; q_I) \exp(ik_{z_I}z_o) \tilde{T}(-q_I + q'_I) \right] \right. \\ & \times \text{rect}\left(|q'_I| \leq \frac{2\pi}{\lambda_I}\right) \exp[ik'_{z_I}(z_I - z_o)] \hat{a}^\dagger_{I,T}(q'_I) \hat{a}^\dagger_S(q_S) |0, 0\rangle \left. \right\} \\ & + C'_\psi \iint dq_S dq'_I \left\{ \exp(ik_{z_S}z_S) (k'_{z_I})^{-1/2} \left[\int dq_I (k_{z_I})^{1/2} \phi(q_S; q_I) \exp(ik_{z_I}z_o) \tilde{R}(-q_I + q'_I) \right] \right. \\ & \times \text{rect}\left(|q'_I| \leq \frac{2\pi}{\lambda_I}\right) \hat{a}^\dagger_{I,R}(q'_I) \hat{a}^\dagger_S(q_S) |0, 0\rangle \left. \right\}. \end{aligned} \quad (4.3)$$

The terms within the square brackets are convolutions along q'_I , for the convolution including the transmission, then

$$[(k'_{zI})^{1/2} \phi(q_S, q'_I) \exp(ik_{zI}z_o)] \otimes \tilde{T}(q'_I) = \int dq_I (k_{zI})^{1/2} \phi(q_S; q_I) \exp(ik_{zI}z_o) \tilde{T}(-q_I + q'_I). \quad (4.4)$$

Assuming that both idler and signal detectors are spatially resolving, the joint spatial probability (JSP) can be found from the general expression of Eq. (3.40) using the electric field operators at the detectors of Eq. (3.41). The JSP results in

$$\begin{aligned} \text{JSP}(x_S, x_I) = C_{\text{JSP}} & \left| \iint dq_I dq_S \exp(iq_S x_S + iq_I x_I) (k_{zS})^{-1/2} (k_{zI})^{-1} \right. \\ & \times \text{conv}(q_S, q_I) \text{rect}\left(|q_I| \leq \frac{2\pi}{\lambda_I}\right) \text{rect}\left(|q_S| \leq \frac{2\pi}{\lambda_S}\right) \\ & \left. \times \exp(ik_{zS}z_S) \exp[ik_{zI}(z_I - z_o)] \right|^2, \end{aligned} \quad (4.5)$$

with the convolution term

$$\text{conv}(q_S, q_I) = [(k_{zI})^{1/2} \phi(q_S, q_I) \exp(ik_{zI}z_o)] \otimes \tilde{T}(q_I). \quad (4.6)$$

Lastly, the quantum ghost diffraction pattern $G(x_S)$ is found by integrating the JSP over the transverse size $\sigma_{I,\text{det}}$ of the non-resolving idler detector

$$G(x_S) = C_{\text{JSP}} \int_{-\sigma_{I,\text{det}}/2}^{+\sigma_{I,\text{det}}/2} dx_I \text{JSP}(x_S, x_I). \quad (4.7)$$

In this chapter, we focus on the scheme that uses a crystal with a thickness larger than the largest wavelength of the photon pair, which can be implemented with common off-the-shelf nonlinear crystals. Such a thick crystal produces photon pairs within small angular ranges along the propagation axis; see chapter 2, and consequently the analysis can be reduced to the paraxial regime. In this regime, the terms $(k_{zS})^{-1/2}$ and $(k_{zI})^{-1}$ become independent of the transverse momentum q [170], and the rectangular functions take an infinite width. Consequently, the convolution term $\text{conv}(q_S, q_I)$, including the joint transverse momentum amplitude $\phi(q_S, q_I)$ of Eq. (2.21), reduces to

$$\text{conv}(q_S, q_I) \approx C [E_P(q_S + q_I) \text{sinc}(\Delta k_z L/2) \exp(ik_{zI}z_o)] \otimes \tilde{T}(q_I), \quad (4.8)$$

where the constant C includes all the terms independent of q , $\Delta k_z = k_{zP} - k_{zS} - k_{zI}$, L is

the thickness of the crystal, and E_p is the transverse profile of the pump in momentum space. As a result of this approximation, the JSP can be written as

$$\begin{aligned} \text{JSP}(x_S, x_I) &\approx C \left| \iint dq_I dq_S \left\{ \exp(iq_S x_S + iq_I x_I) \right. \right. \\ &\quad \left. \left. \times \text{conv}(q_S, q_I) \exp(ik_{z_S} z_S) \exp[ik_{z_I}(z_I - z_o)] \right\} \right|^2 \\ &\approx C' \left| \mathcal{F}^{-1} \left\{ \text{conv}(q_S, q_I) \exp(ik_{z_S} z_S) \exp[ik_{z_I}(z_I - z_o)] \right\} \right|^2, \end{aligned} \quad (4.9)$$

where \mathcal{F}^{-1} is a two-dimensional inverse Fourier transform that can be easily implemented numerically using an FFT algorithm.

As a next step, it will be shown numerically in Fig. 4.2 that the diffraction pattern of a double slit can be obtained using the JSP of Eq. (4.9) and the ghost diffraction pattern G of Eq. (4.7). Afterwards, its features are discussed and finally the analysis of QGD is used as a starting point of the next section on pinhole QGI.

For this numerical example, we consider a pump beam with Gaussian transverse spatial spectrum and its waist is located at the center of the nonlinear crystal at the plane $z = 0$, that is, $E_p = \exp[-\sigma_p^2(q_S + q_I)^2/2]$, which features a flat wave front and a width σ_p in position space. In this example, $\sigma_p = 800\mu\text{m}$. The pump beam has a wavelength of $\lambda_p = 350\text{nm}$ and signal and idler photons have degenerate wavelengths $\lambda_S = \lambda_I = 700\text{nm}$. The nonlinear crystal thickness L is taken much larger than any of the wavelengths with $L = 3\text{mm}$ and the object is chosen to be a double slit with $d = 940\mu\text{m}$ slit separation with unity transmission in each slit of $50\mu\text{m}$ width and zero transmission elsewhere, located at $z_o = 30\text{cm}$. To portray the influence of the object in the JSP, we fix the position of the detector in the signal arm at $z_S = 1.5\text{m}$ and the idler detector at various positions z_I from the crystal, as seen in Fig. 4.2(a-d). In Fig. 4.2(a), the idler detector is located very close to the object at a distance $z_I = 1.1z_o = 33\text{cm}$ where the JSP clearly shows the presence of the two slits along x_I in the form of two distinctive thin lobes. As the idler detector is farther from the object, each of these lobes diffracts along x_I , which results in an increase in their widths. This leads to an overlap of the lobes that start to form interference fringes in the JSP, see Fig. 4.2(b). If the detector gets farther, as observed in Fig. 4.2(c,d), the detector plane approaches the far-field region with respect to the object plane. This results in a JSP pattern that changes only in size but not in overall shape upon moving farther away from the detectors. In Fig. 4.2(d), the distance between the object and the detector is

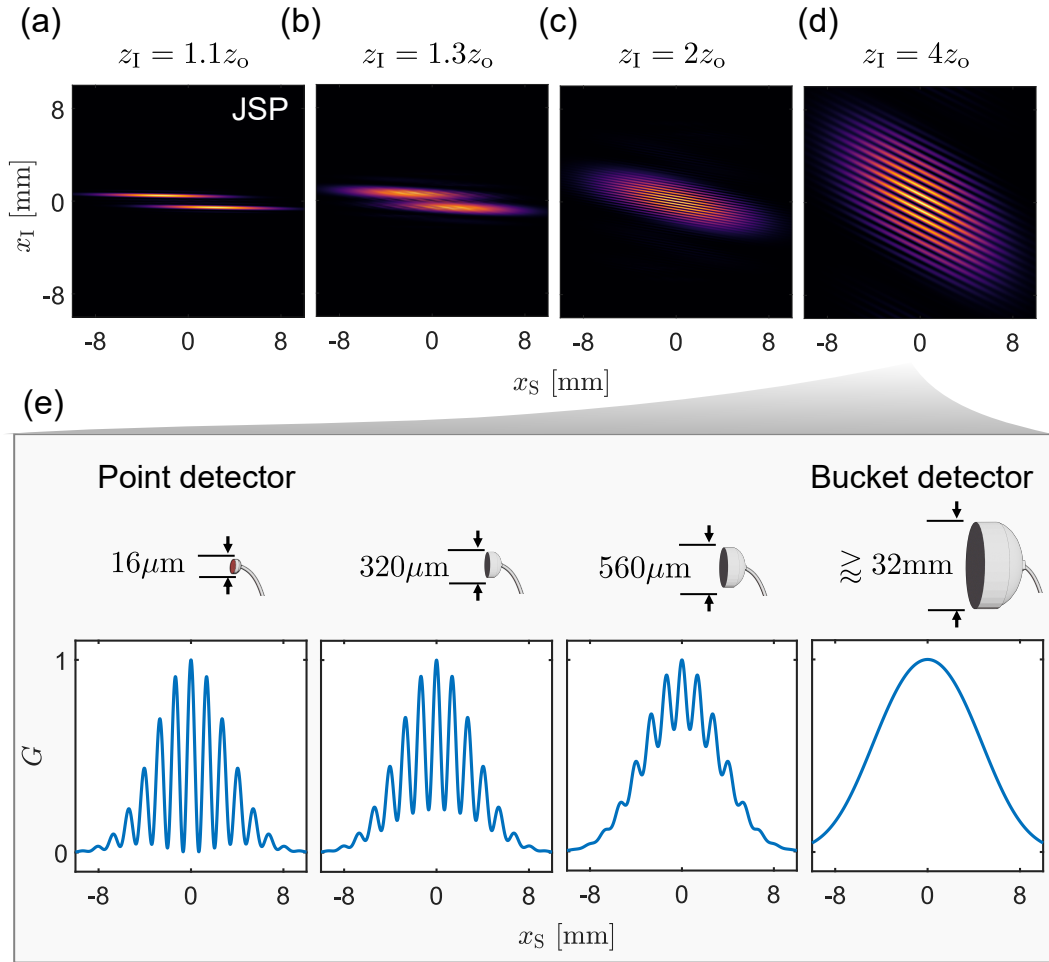


Figure 4.2. (a-d) $JSP(x_s, x_I)$ of a double slit for various distances z_I . The slit separation is $940\mu\text{m}$ and slit width is $50\mu\text{m}$, located at $z_o = 30\text{cm}$, and a pump width of $800\mu\text{m}$. (e) Quantum ghost diffraction pattern $G(x_s)$ obtained from the JSP with $z_I = 4z_o$ for different sizes of the non-resolving detector, from point detector to bucket detector.

$z_I - z_o = 90\text{cm}$, which is close to the far-field region, which occurs when [158]

$$z_I - z_o \gg \frac{d^2}{\lambda_I} = \frac{(940\mu\text{m})^2}{700\text{nm}} = 1.26\text{m}. \quad (4.10)$$

Furthermore, the ‘diagonal-like’ shape of the obtained JSP shows that there is spatial correlation between signal and idler. One can visually notice that the correlation can be exploited to reveal the well-known diffraction pattern of the double slit in coincidences, even though the detector in the idler arm is spatially insensitive. This is illustrated in the ghost diffraction patterns $G(x_s)$ in Fig. 4.2(e), obtained from the JSP of Fig. 4.2(d) using Eq. (4.7). Importantly, G with a high visibility is seen by using a point-like idler detector with transverse size of $\sigma_{I,\text{det}} = 16\mu\text{m}$. However, if the spatially non-resolving idler detector increases in size, the visibility of the diffraction pattern

reduces, until completely disappearing if the detector becomes a ‘bucket’ that collects all the incoming idler photons. In this particular example, a bucket detector is realized when $\sigma_{I,\text{det}} \gtrsim 32\text{mm}$.

We observe in Fig. 4.2(e), first, that an interference pattern of the double slit can be obtained in coincidences G by using a point-like detector behind the object, as was shown in Ref. [89]. Second, the contrast of the interference pattern depends on the transverse size of the idler detector, as seen in Fig. 4.2(e): the smaller the detector, the higher the contrast. On the one extreme, the contrast is maximum when using a point detector, which leads to $G(x_S) \propto \text{JSP}(x_S, 0)$. On the other extreme, where the idler detector is a large bucket detector that simply collects all idler photons and has no spatial resolution, then $G(x_S) \propto \int_{-\infty}^{+\infty} dx_I \text{JSP}(x_S, x_I)$. In this case, the use of a bucket detector washes out the interference pattern, and the information that the object is a double slit is lost.

Beyond QGD, Pittman et al. showed that the image of the object, instead of its diffraction pattern, can be obtained in coincidences, as was shown in chapter 3. To realize a ghost image, lenses are adequately introduced in the path of one down-converted photon, and the idler point detector is exchanged to a bucket detector. However, later on, the same author also demonstrated that if the phase front of the pump was *curved* inside the crystal, then the QGD scheme can produce images without the use of lenses in the arms of the signal and idler photons [125]. However, as will be shown below, a pump with a *flat* phase front can also be used for lensless imaging by using a pump width of the right size.

4.2. Pinhole quantum ghost imaging

In this section, we demonstrate how a QGD scheme can be turned into a ghost imaging scheme that does not use any lenses in the signal and idler paths and uses a pump with a flat phase front. The proposed scheme is illustrated in Fig. 4.3. We showed in the previous section that the QGD pattern disappears when the idler detector is a bucket, i.e., it simply collects all incoming idler photons and lacks spatial resolution. However, here we keep the bucket detector to demonstrate the influence of the pump width, as highlighted in the inset of Fig. 4.3. We fix the pump beam to have a flat phase front in the middle of the nonlinear crystal.

Figure 4.4(a-d) shows joint spatial probabilities JSPs for the pump widths σ_p of $58\mu\text{m}$, $102\mu\text{m}$, $167\mu\text{m}$, and $800\mu\text{m}$, respectively, together with the corresponding ghost patterns G in Fig. 4.4(e). The last value of σ_p was used in the previous section to find the QGD pattern. It is evident that the shape of the JSP changes drastically

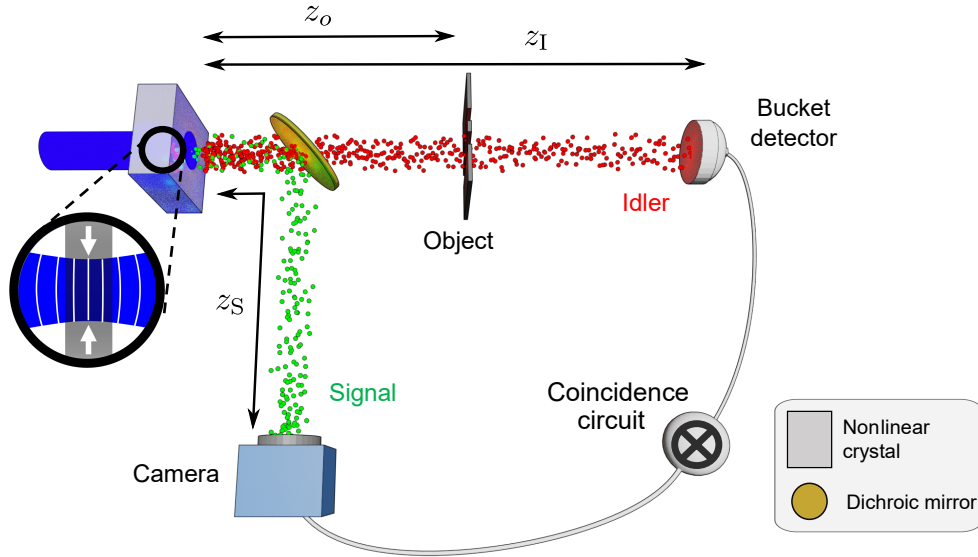


Figure 4.3. Sketch of the pinhole quantum ghost imaging scheme. The inset highlights that the pump width has to be optimized to achieve imaging, as explained in the main text.

with the reduction of the pump width. According to Fig. 4.4(c), the double-slit object seems to produce two spots whose centers are separated along x_S approximately five times more than the actual slit separation. Depending on the width of the pump beam, these spots in the JSP change their widths and, in general, overlap and interfere. The interference reaches a minimum in Fig. 4.4(c) with pump width $\sigma_p = 167\mu\text{m}$. In Fig. 4.4(e), we show the corresponding ghost patterns G , where the cases of (a-d) are labeled. Remarkably, in this numerical investigation we see that for a specific range of pump widths two separate maxima are visible in G , which seems to correspond to an image of the double slit.

To better understand the characteristics of the obtained pattern, we find an analytical expression that describes it in the next section.

4.2.1. Derivation of the ghost image in the paraxial regime

The obtained ghost patterns G point out that it is indeed possible to produce an image with a pump of the appropriate size. We derive an analytical model to understand the image properties and find the optimal conditions to obtain it. To find an expression of the ghost pattern G , the JSP has to be found first. The JSP is described in Eq. (4.9), and can be written as $\text{JSP}(x_S, x_I) \propto |\Psi|^2$, where

$$\Psi = \iint dq_S dq_I \Phi(q_S, q_I) \exp(iq_S x_S + iq_I x_I) \quad (4.11)$$

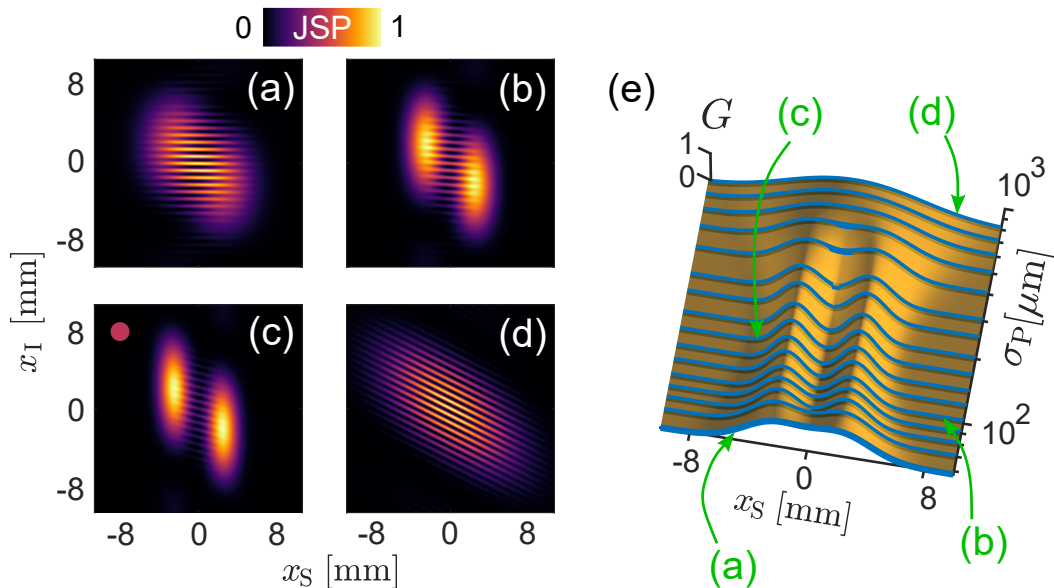


Figure 4.4. (a-d) $\text{JSP}(x_S, x_I)$ and corresponding (e) quantum ghost pattern $G(x_S)$ of a double slit, $940\mu\text{m}$ slit separation and $50\mu\text{m}$ slit width, located at $z_o = 30\text{cm}$ produced by a pump width σ_P of (a) $58\mu\text{m}$, (b) $102\mu\text{m}$, (c) $167\mu\text{m}$, and (d) $800\mu\text{m}$.

with

$$\Phi = \left\{ [E_p(q_S + q_I) \text{sinc}(\Delta k_z L/2) \exp(ik_{zI}z_o)] \otimes \tilde{T}(q_I) \right\} \exp(ik_{zS}z_S) \exp[ik_{zI}(z_I - z_o)], \quad (4.12)$$

where the term in curly brackets comes from the convolution $\text{conv}(\cdot)$ of Eq. (4.8). Next, we consider only one of the slits of the object and consider that it has an infinitesimal width and is located at $x_I = d/2$, which means that the transmission can be written as

$$T(x_I) = \delta\left(x_I - \frac{d}{2}\right) \quad (4.13)$$

and

$$\tilde{T}(q_I) = \exp\left[-i\left(\frac{d}{2}\right)q_I\right]. \quad (4.14)$$

Further assumptions must be made to find an analytic solution of Φ written in Eq. (4.12) to later find the JSP. First, we make use of the paraxial approximation where q_S and q_I are small, therefore k_z can be approximated to $k_z = \sqrt{k^2 - q^2} \approx k - q^2/(2k)$. Second, since we are working in the paraxial regime, the main lobe of the sinc function appearing in Φ can be approximated with a Gaussian function [167, 189] $\text{sinc}(x^2) \approx \exp(-4\gamma x^2)$ where $\gamma = 0.2$ ensures that the sinc and the Gaussian coin-

cide at 0.1. These two approximations were also used in Eq. (3.31) to find the paraxial resolution of quantum imaging with undetected photons. Consequently, under such two approximations, the term Φ becomes

$$\begin{aligned} \Phi = & C \exp \left\{ - \left(i \frac{z_1 - z_0}{2k_1} \right) q_1^2 - i \left(\frac{d}{2} \right) q_1 + \left[\left(\frac{1}{k_p} - \frac{1}{k_s} \right) \gamma L - \frac{\sigma_p^2}{2} - i \frac{z_s}{2k_s} \right] q_s^2 \right\} \\ & \times \int d\tilde{q}_1 \exp \left(\left[\left(\frac{1}{k_p} - \frac{1}{k_1} \right) \gamma L - \frac{\sigma_p^2}{2} - i \frac{d}{2k_1} \right] \tilde{q}_1^2 + \left\{ 2q_s \left[\left(\frac{1}{k_p} \right) \gamma L - \frac{\sigma_p^2}{2} \right] + i \frac{d}{2} \right\} \tilde{q}_1 \right), \end{aligned} \quad (4.15)$$

where C is a constant. This expression contains a one-dimensional Gaussian integral of the form [207],

$$\int d\tilde{q}_1 \exp \left(-\frac{1}{2} A \tilde{q}_1^2 + B \tilde{q}_1 \right) = \left(\frac{2\pi}{A} \right)^{1/2} \exp \left(\frac{B^2}{2A} \right), \quad (4.16)$$

where

$$A = -2 \left[\left(\frac{1}{k_p} - \frac{1}{k_1} \right) \gamma L - \frac{\sigma_p^2}{2} - i \frac{d}{2k_1} \right], \quad (4.17a)$$

$$B = 2q_s \left[\left(\frac{1}{k_p} \right) \gamma L - \frac{\sigma_p^2}{2} \right] + i \frac{d}{2}. \quad (4.17b)$$

This turns Φ into a simpler expression and we proceed and find Ψ using the inverse Fourier transform of Eq. (4.11). This has the form of a Gaussian integral in two dimensions of the form [207]

$$\begin{aligned} \Psi = & C \iint dq_s dq_1 \exp \left(-\frac{1}{2} C_1 q_s^2 - \frac{1}{2} \alpha_1 q_1^2 + D_1 q_s + D_2 q_1 \right) \\ = & C' \exp \left[\frac{1}{2 C_1 \alpha_1} (\alpha_1 D_1^2 + C_1 D_2^2) \right], \end{aligned} \quad (4.18)$$

with

$$C_1 = i \frac{z_1 - z_0}{k_1}, \quad (4.19a)$$

$$D_1 = i \left(x_1 - \frac{d}{2} \right), \quad (4.19b)$$

$$D_2 = i \left(x_s - \alpha_2 \frac{d}{2} \right), \quad (4.19c)$$

and

$$\alpha_1 = -2 \left[\left(\frac{1}{k_p} - \frac{1}{k_s} \right) \gamma L - \frac{\sigma_p^2}{2} - i \frac{z_s}{2k_s} \right] \quad (4.20a)$$

$$+ 2 \left[\left(\frac{1}{k_p} \right) \gamma L - \frac{\sigma_p^2}{2} \right]^2 \left[\left(\frac{1}{k_p} - \frac{1}{k_I} \right) \gamma L - \frac{\sigma_p^2}{2} - i \frac{z_o}{2k_I} \right]^{-1},$$

$$\alpha_2 = \left[\left(\frac{1}{k_p} \right) \gamma L - \frac{\sigma_p^2}{2} \right] \left[\left(\frac{1}{k_p} - \frac{1}{k_I} \right) \gamma L - \frac{\sigma_p^2}{2} - i \frac{z_o}{2k_I} \right]^{-1}. \quad (4.20b)$$

Since the joint spatial probability is $\text{JSP}(x_s, x_I) \propto |\Psi|^2$, then the ghost pattern, considering a bucket detector that collects all the idler photons, becomes

$$G(x_s) = C_{\text{JSP}} \int dx_I \text{JSP}(x_s, x_I) = C'_{\text{JSP}} \exp \left[-\frac{(x_s - x_0)^2}{2\sigma_G^2} \right]. \quad (4.21)$$

Here, the width σ_G and the maximum located at x_0 are given by

$$\sigma_G = \left[2 \text{Re} \left(\frac{1}{\alpha_1} \right) \right]^{-1/2}, \quad (4.22a)$$

$$x_0 = \frac{d}{2} \text{Re} \left(\frac{\alpha_2}{\alpha_1} \right) \left[\text{Re} \left(\frac{1}{\alpha_1} \right) \right]^{-1}, \quad (4.22b)$$

where the variables α_1 and α_2 can be written more compactly using $k = 2\pi/\lambda$,

$$\alpha_1 = \sigma_p^2 + \frac{\gamma L}{\pi} (\lambda_s - \lambda_p) + i \frac{\lambda_s z_s}{2\pi} - \left(\sigma_p^2 - \frac{\gamma L \lambda_p}{\pi} \right) \alpha_2, \quad (4.23a)$$

$$\alpha_2 = \left(\sigma_p^2 - \frac{\gamma L \lambda_p}{\pi} \right) \left[\sigma_p^2 + \frac{\gamma L}{\pi} (\lambda_I - \lambda_p) + i \frac{z_o \lambda_I}{2\pi} \right]^{-1}. \quad (4.23b)$$

Due to the presence of the bucket detector that collects all idler photons behind the object, the equations do not depend on z_I , the distance of the object to the bucket detector; however, the model does depend on the location of the resolving detector z_s . Figure 4.5(a) shows the width of the ghost pattern σ_G with respect to the width of the pump σ_p and the distance from the object to the crystal z_o . Additionally, Fig. 4.5(b) depicts the normalized position $x_0/(d/2)$ also as a function of σ_p and z_o . The distance to the signal detector remains $z_s = 1.5\text{m}$ throughout this chapter. We observe in Fig. 4.5(a) that, for each object position z_o , the width of the ghost pattern σ_G has a minimum at a certain pump width σ_p . This confirms the observations of the numerical example in Fig. 4.4 using $z_o = 30\text{cm}$, where the optimal case for imaging, marked with a dot in Fig. 4.4(c), leads to the narrowest ghost pattern for each of the slits. In the rest of the cases, the pattern of each slit is too wide, resulting in considerable overlap

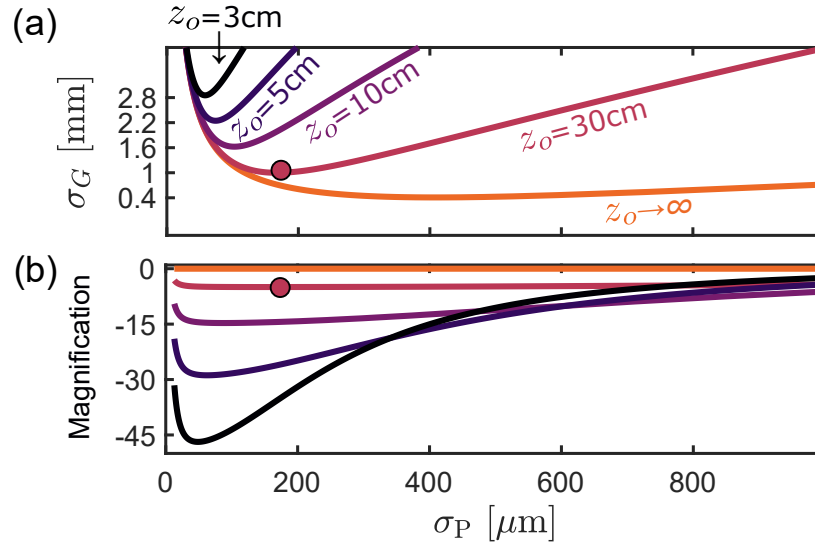


Figure 4.5. (a) Width of the ghost pattern σ_G and (b) position magnification $x_0/(d/2)$ of a infinitesimal slit at $x_1 = a$ with respect to the pump width σ_P at various distances z_0 from the slit to the crystal. The circle marks the parameters of the numerical example in Fig. 4.4(c).

and interference between the contribution of the double-slit object and hence the loss of visibility of the ghost pattern. If a second infinitesimal slit would be at $x_1 = -d/2$, the distance between the two maxima in the ghost patterns would be $2x_0$, therefore, $x_0/(d/2)$ represents the magnification. Figure 4.5(b) verifies that for the numerical example in Fig. 4.4, the magnification is approximately equal to five. It also shows that the magnification is negative, meaning that the ghost image G is inverted.

It is noteworthy that the lensless quantum imaging scheme found can be understood from a more familiar imaging configuration, namely the classical pinhole camera, as will be presented next.

4.2.2. Analogy to the classical pinhole camera

Here, a connection between the lensless QGI described and the well-known classical pinhole camera will be presented. This analogy is useful to have a more intuitive grasp of the underlying imaging mechanism and aids in the design of the proposed imaging scheme.

To start with the analogy, we notice that in our proposed lensless QGI scheme, the minimum width of the ghost pattern σ_G illustrated in Fig. 4.5(a) becomes smaller as the object is placed farther from the crystal. However, this value does not reach zero, instead the behavior of the curve of σ_G converges to the orange curve in the limit where the object is very distant from the crystal, $z_0 \rightarrow \infty$, therefore, σ_G becomes independent of z_0 for large z_0 . In this limit, the expression of σ_G in Eq. (4.22a) can

be reduced to

$$\sigma_G^2 = \sigma_0^2 + \frac{1}{\sigma_0^2} \left(\frac{z_S \lambda_S}{4\pi} \right)^2. \quad (4.24)$$

The width of the ghost pattern of an infinitesimal slit object with the spatially resolving detector placed right after the crystal, $\sigma_0 = \sigma_G(z_S = 0)$, is

$$\sigma_0 = \left[\frac{1}{2} \sigma_p^2 + \gamma \left(\frac{\lambda_S}{\lambda_I} \right) \left(\frac{\lambda_p L}{2\pi} \right) \right]^{1/2}. \quad (4.25)$$

This expression depends only on the parameters of the two-photon source. It is easy to see that the ghost pattern width σ_G has a minimum value, for a fixed value of $z_S \lambda_S$, namely $\sigma_G^{\min} = \sqrt{2} \sigma_0$, when

$$\sigma_0^2 = \frac{z_S \lambda_S}{4\pi}. \quad (4.26)$$

Remarkably, this result showing the optimal conditions to create a lensless ghost image is equivalent to the optimal pinhole size σ_{pinhole} in a classical pinhole camera that creates the smallest point image of a slit upon spatially incoherent illumination [197], i.e.,

$$\sigma_{\text{pinhole}}^2 \approx z \lambda, \quad (4.27)$$

where z is the distance from the detector to the pinhole. Consequently, in this analogy, σ_0 can be considered the ‘pinhole size’ of QGI and it depends not only on the width of the pump but also on the thickness of the crystal and the two-photon wavelengths. However, notice that for a pump with negligible diffraction inside the crystal $\sigma_p^2 \gg \lambda_p L / (2\pi)$, the deviation of the equivalent pinhole size σ_0 from the pump width σ_p is small. Moreover, we now analyze the magnification to draw more parallels between the proposed QGI scheme and the classical pinhole camera.

The magnification of the classical pinhole camera is given by geometric optics as $-z/z_o$, where z is the distance detector-pinhole and z_o is the distance object-pinhole. A similar relation can be found from the analytical model of the proposed ghost imaging scheme using Eq. (4.22b), under two conditions: First,

$$\sigma_p^2 \gg \frac{\gamma L}{\pi} [\max(\lambda_S, \lambda_I) - \lambda_p] \quad (4.28)$$

that ensures that the signal, idler, and pump waves have negligible diffraction inside the nonlinear crystal. In this case, σ_p defines the size of the generated signal and idler

beams inside the crystal, and hence their Rayleigh lengths are also much larger than the crystal thickness L , meaning that their phase fronts are approximately flat inside the crystal. Second,

$$\left\{ \frac{z_o \lambda_I}{2\pi}, \frac{z_s \lambda_S}{2\pi} \right\} \gg \sigma_p^2, \quad (4.29)$$

stating that both the object and the resolving detector are in the far-field of the two-photon source. Under these two conditions, we find the magnification from Eq. (4.22b) to be

$$\frac{x_0}{(d/2)} \approx -\left(\frac{z_s}{z_o}\right)\left(\frac{\lambda_s}{\lambda_I}\right). \quad (4.30)$$

This is similar to the magnification of the classical pinhole camera, but includes the two-photon wavelengths. From this expression, the magnification of the numerical example in Fig. 4.4 with $\lambda_s/\lambda_I = 1$ can be quickly found to be $-(1.5\text{m}/30\text{cm})(1) = -5$. Hence, the ghost image of the double slit with slit separation of $940\mu\text{m}$ should show two peaks separated by a distance of 4.7mm .

To portray the effect of the wavelengths in the magnification and confirm the derived expression of Eq. (4.30), we plot three numerical cases of the ghost pattern G along with its corresponding JSP, see Fig. 4.6, as was done at the beginning of the chapter in Fig. 4.4. The signal wavelength $\lambda_s = 700\text{nm}$ is fixed, and the separation between the slits is kept at $940\mu\text{m}$. We begin by again plotting the JSP and G corresponding to the degenerate case with $\lambda_s/\lambda_I = 1$ in Fig. 4.6(b), which is the same as Fig. 4.4(c). Here, G displays the image of the two slits separated by 4.7mm . Additionally, we illustrate the non-degenerate cases with $\lambda_s/\lambda_I = 1/2$ in Fig. 4.6(a) and $\lambda_s/\lambda_I = 2$ in Fig. 4.6(c). The slit separation in G is 2.35mm and 9.4mm , respectively. Thus, the numerical result shows that the magnifications are -2.5 for $\lambda_s/\lambda_I = 1/2$, -5 for $\lambda_s/\lambda_I = 1$, and -10 for $\lambda_s/\lambda_I = 2$. Therefore, the derived magnification expression of Eq. (4.30) correctly predicts all three cases with degenerate and non-degenerate wavelengths.

The analogy between lensless QGI and the classical pinhole camera aids to build a more familiar understanding of the proposed QI scheme, which becomes relevant when designing such scheme with correlated photons. In this analogy, the important found parameters are the ‘pinhole size’ of QGI given by σ_o of Eq. (4.25) and the magnification given by Eq. (4.30). It should be noted that our imaging scheme is not limited to the far-field domain. We only take the approximations which simplify the found expressions in order to make the analogy with the classical pinhole camera.

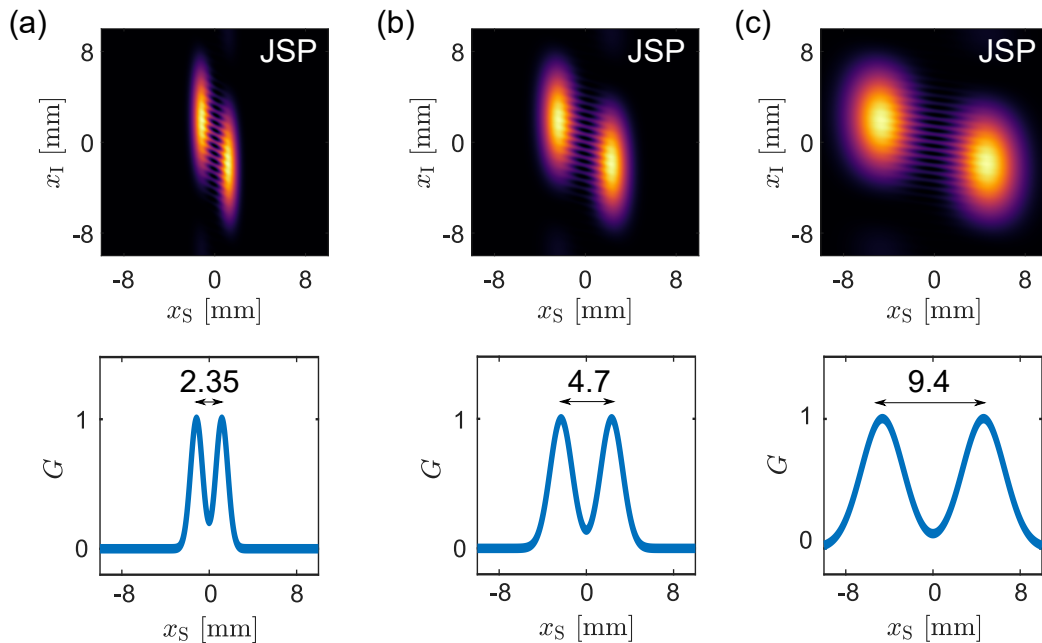


Figure 4.6. Magnification of the ghost image for photon pairs with degenerate and non-degenerate wavelengths. Top: JSP with $\lambda_s = 700\text{nm}$, (a) $\lambda_s/\lambda_I = 1/2$, (b) $\lambda_s/\lambda_I = 1$ [same as Fig. 4.4(c)], (c) $\lambda_s/\lambda_I = 2$. Bottom: Ghost images corresponding to their respective JSPs.

4.2.3. Transverse resolution and number of spatial modes within the paraxial regime

We further exploit the analytical model of the ghost pattern G of one slit given by Eqs. (4.21) and (4.22) to derive the transverse resolution and number of spatial modes of pinhole QGI within the paraxial regime considered.

In the following derivation, we use Rayleigh's resolution criterion, which is defined as the minimum distance between two point-like objects enabling one to distinguish them from one another [158]. To optimally resolve two objects, not only the ghost pattern width σ_G has to be taken into account, but also the magnification. Namely, a small width σ_G and also a large magnification $|x_0/(d/2)|$ are needed. To test this, we use the Gaussian ghost pattern derived from an infinitesimal slit A at $x_I = d/2$ of Eq. (4.21). For simplicity, we normalize its maximum to one, resulting in the ghost pattern $G_A = \exp[-(x_S - x_0)^2/(2\sigma_G^2)]$, where σ_G is given by Eq. (4.22a) and x_0 by Eq. (4.22b). If a second similar slit B is included, but at $x_I = -d/2$, the resulting ghost pattern is symmetric with respect to $x_S = 0$ and is given approximately by $G \approx G_A + G_B$, assuming negligible interference. It can be said, that the two slits can be distinguished from one another in G when the intensity at $x_S = 0$ between the two maxima is smaller than a certain threshold, here heuristically chosen to be 40% of the maximal intensity

at $x_s = \pm x_0$. Therefore, the approximate threshold condition² defines that

$$G(x_s = 0)_{\text{th}} \approx G_A(0) + G_B(0) = 2G_A(0) = 0.4. \quad (4.31)$$

Using the expression for G_A within $G(0)_{\text{th}}$, including σ_G from Eq. (4.22a), and x_0 from Eq. (4.22b), we have

$$\begin{aligned} G(0)_{\text{th}} &= 2 \exp\left(-\frac{x_0^2}{2\sigma_G^2}\right) \\ &= 2 \exp\left\{-\left(\frac{d_{\min}}{2}\right)^2 \left[\text{Re}\left(\frac{\alpha_2}{\alpha_1}\right)\right]^2 \left[\text{Re}\left(\frac{1}{\alpha_1}\right)\right]^{-2} \left|\text{Re}\left(\frac{1}{\alpha_1}\right)\right|\right\}, \end{aligned} \quad (4.32)$$

where d_{\min} is the minimum resolvable distance d between two identical infinitesimal slits, i.e., the transverse spatial resolution, which results in

$$d_{\min} = 2 \left\{ -\ln \left[\frac{1}{2} G(0)_{\text{th}} \right] \left| \text{Re}\left(\frac{1}{\alpha_1}\right) \right| \right\}^{1/2} \left| \text{Re}\left(\frac{\alpha_2}{\alpha_1}\right) \right|^{-1}. \quad (4.33)$$

Figure 4.7(a) displays the dependence of d_{\min} on the pump width σ_p at different object distances z_o . The thick green line connects the minima of several curves over a wider range of z_o to depict the trend. We showed before in Fig. 4.5(a) that the minimum width of the ghost pattern σ_G becomes smaller as the object is farther from the crystal. Hence, one could naively expect from σ_G that the resolution d_{\min} could improve as the object is farther; however, the tendency of Fig. 4.7(a) tells the opposite. The reason for this is that d_{\min} is enhanced by the large magnification that occurs at small object distances z_o , as showcased in Fig. 4.5(b). This is confirmed numerically by revisiting the case depicted in Fig. 4.4(b), which uses a pump width of $102\mu\text{m}$ and $z_o = 30\text{cm}$ where the ghost pattern had low visibility; however, now we change the position of the object to $z_o = 10\text{cm}$. The resulting JSP and the ghost pattern G are shown in Fig. 4.7(b). Compared to Fig. 4.4(b), the visibility of the image of the double slit increases due to the larger magnification. This originates from the fact that, for a fixed object distance z_o , the minimum ghost pattern width σ_G does not coincide with the largest magnification $x_0/(d/2)$, see Fig. 4.5. Therefore, the optimal pump width σ_p that results in the best resolution is not necessarily when σ_G is minimized, except for larger values of z_o where the magnification $x_0/(d/2)$ is almost independent of σ_p , as can be seen in Fig. 4.5(b).

It should be noted that the green tendency line in Fig. 4.7(a) shows that the closer

² The decision to take the resolution criterion to be 40% does not rely on any profound physical reason, it is only practical. Other works take less restrictive values around 80%, and we did too in chapter 3.

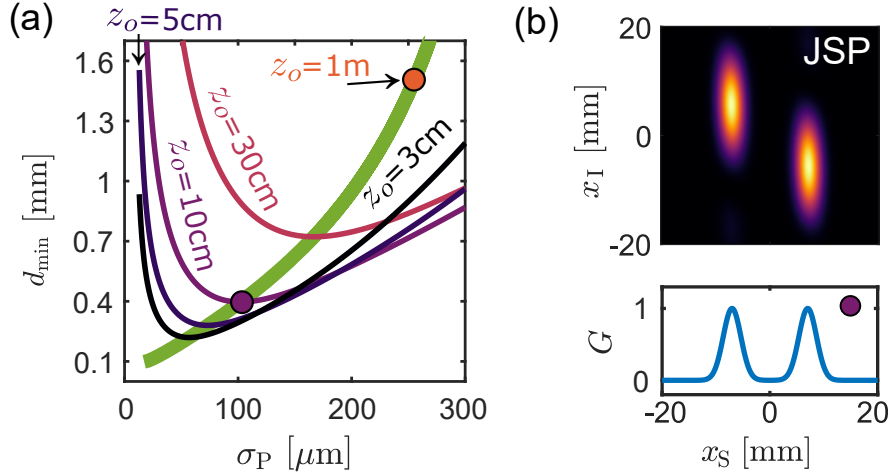


Figure 4.7. (a) Resolution d_{\min} with respect to the pump width σ_P . The green line connects the minima of curves of a wider range of object distances z_o . (b) Numerically, JSP (top) and G (bottom) of a double slit. The purple circle in (a) marks the parameters of (b).

the object is to the crystal and the smaller the pump width, the better the minimum resolvable distance d_{\min} . However, a smaller pump width has a broader spatial spectrum, which is a scenario where the paraxial approximation used does not hold. We observe in Fig. 4.7(a), that the resolution within the paraxial regime d_{\min} of pinhole QGI is much larger than the idler and signal wavelengths. As thoroughly analyzed in chapter 3, we can infer that the fundamental resolution limit of pinhole QGI is also dictated by the largest wavelength of the photon pair if an ultra-thin crystal was used. This is because the general expression of the JSP in pinhole QGI, before any paraxial approximation, given in Eq. (4.5) has the same form as the JSP of the QGI in Eq. (3.42), except from some phase terms corresponding to photon propagation. Furthermore, notice that the resolution d_{\min} in the paraxial regime of Fig. 4.7(a) tends to depend linearly on the object position z_o for large values of z_o . This is because in such case, as was mentioned earlier, the ghost pattern width σ_G is nearly independent of z_o , see Fig. 4.5(a), and the magnification is $|x_0/(d/2)| \propto 1/z_o$, as described in Eq. (4.30).

In addition to the resolution, it is also of great interest to describe the transverse extent of the idler illumination onto the object, which limits the object size that can be imaged. To find the illumination size on the object, we assume that the idler detector is located at the object position $z_I = z_o$ and the camera for the signal is at z_S . Then, the function Φ that contains the two-photon propagation becomes a simpler form of Eq. (4.12),

$$\begin{aligned} \Phi = C \exp & \left[-i \frac{z_S}{2k_S} q_S^2 - i \frac{z_o}{2k_I} q_I^2 - \frac{1}{2} \sigma_P^2 (q_S + q_I)^2 \right] \\ & \times \exp \left[-\frac{\gamma L}{k_S} q_S^2 - \frac{\gamma L}{k_I} q_I^2 + \frac{\gamma L}{k_P} (q_S + q_I)^2 \right]. \end{aligned} \quad (4.34)$$

This function, as shown previously, is used to calculate the joint spatial probability $\text{JSP} = \Phi^* \Phi$ leading to

$$\text{JSP}(x_S, x_I) = C_{\text{JSP}} \exp \left[-\text{Re} \left(\frac{A_{22}}{\det(A)} \right) x_I^2 - \text{Re} \left(\frac{A_{11}}{\det(A)} \right) x_S^2 + \text{Re} \left(\frac{A_{12} + A_{21}}{\det(A)} \right) x_S x_I \right], \quad (4.35)$$

with the 2x2 matrix A composed of

$$A_{11} = 2 \left(\frac{1}{k_I} - \frac{1}{k_P} \right) \gamma L + \sigma_P^2 + i \frac{z_o}{k_I}, \quad (4.36a)$$

$$A_{22} = 2 \left(\frac{1}{k_S} - \frac{1}{k_P} \right) \gamma L + \sigma_P^2 + i \frac{z_S}{k_S}, \quad (4.36b)$$

$$A_{12} + A_{21} = 2 \left(-\frac{\gamma L}{2k_P} + \sigma_P^2 \right). \quad (4.36c)$$

The illumination on the object is then the projection of the JSP on the idler axis x_I that results in a Gaussian transverse profile with width σ_{illum} . For an object and camera located in the far field, the illumination size is simplified to

$$\sigma_{\text{illum}} \approx \frac{z_o \lambda_I}{2\pi} \left\{ \frac{2 \left[(\lambda_S - \lambda_P) \frac{\gamma L}{\pi} + \sigma_P^2 \right]}{4 \left[(\lambda_I - \lambda_P) \frac{\gamma L}{\pi} + \sigma_P^2 \right] \left[(\lambda_S - \lambda_P) \frac{\gamma L}{\pi} + \sigma_P^2 \right] - \left[-\lambda_P \frac{\gamma L}{\pi} + \sigma_P^2 \right]^2} \right\}^{\frac{1}{2}} \quad (4.37)$$

This illumination size σ_{illum} increases linearly with the longitudinal position of the object z_o . Importantly, the ratio between the illumination size and the minimum resolvable distance d_{min} tells the maximum number of identical infinitesimal slits that can be resolved inside the illuminated region of the object;

$$N \equiv \frac{\sigma_{\text{illum}}}{d_{\text{min}}}, \quad (4.38)$$

i.e., describes the number of independent spatial modes in the object illumination [151]. The dependence of N on the crystal thickness L is displayed in Fig. 4.8 for various z_o , each at a pump width σ_P that minimizes the resolution as described by the green line in Fig. 4.7(a). This shows that to increase the number of spatial modes N , a thinner crystal can be used, as it allows a larger range of transverse wave-vectors,

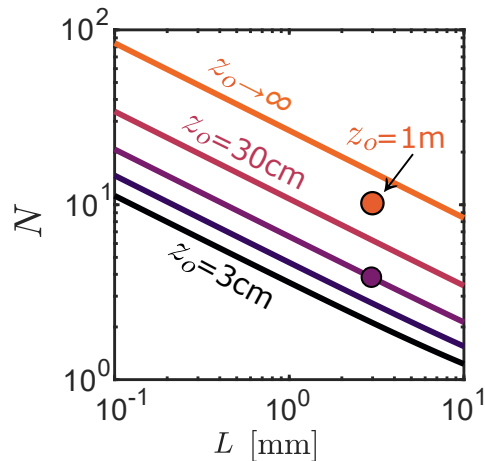


Figure 4.8. Number of spatial modes N with respect to the crystal thickness L at various z_o . The purple circle marks the parameters of Fig. 4.7(b).

this was shown in section 2.2.1. Also, N can increase if the object is placed farther away from the crystal; however, this has a limit due to the linear dependence of both σ_{illum} and d_{min} on z_o for very distant objects.

Lastly, we investigate the resolution and number of modes for the case where the photon pairs have non-degenerate wavelengths. The corresponding plots are shown in Fig. 4.9. Here, the idler wavelength is kept fixed at $\lambda_i = 700\text{nm}$ and the signal wavelength is changed. Figures 4.9(a,c) depict the case for $\lambda_s/\lambda_i = 1/4$, and Figs. 4.9(b,d) for $\lambda_s/\lambda_i = 4$. In Figs. 4.9(a,b), we observe that the minimum d_{min} for a given object position z_o varies more noticeably with the non-degenerate wavelengths only for large z_o . In such a specific scenario, the resolution slightly improves with larger λ_s/λ_i using a larger pump width. Finally, Figs. 4.9(c,d) show that the number of modes N also has a greater variation with the non-degenerate photons at larger z_o . The larger λ_s/λ_i is used, then the larger N is obtained. This is a consequence of the improved resolution under the same particular conditions, as just mentioned before.

4.3. Abstract and publication

Quantum ghost diffraction and imaging have been comprehensively presented in this chapter. Using the basis of QGD, we put forward the concept of a QGI scheme that is analogous to the classical pinhole camera. The scheme relies on choosing a pump beam with a flat wave front and the right width dependent on the rest of the parameters of the scheme. Pinhole QGI is ideal for applications that use wavelengths where lenses are less available and a high transverse resolution is not needed. This work was presented at two conferences [208, 209] and was published in Applied Physics Letters [210].

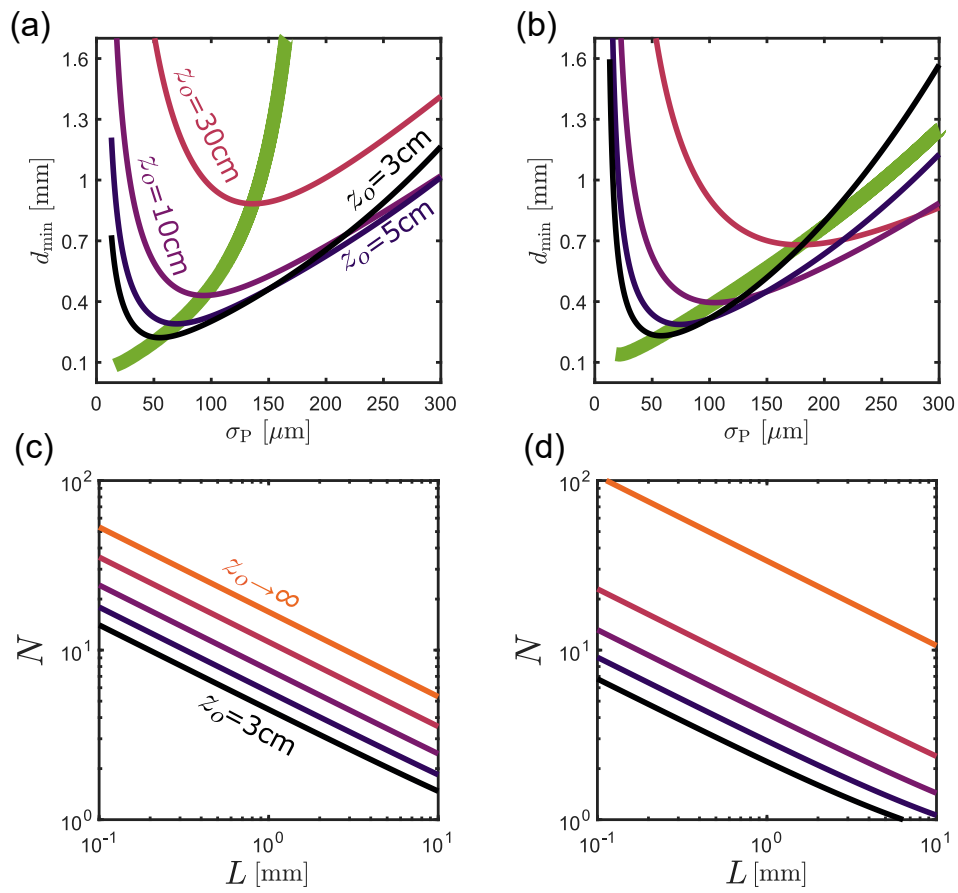


Figure 4.9. (a,b) Resolution d_{\min} with respect to the pump width σ_P and (c,d) number of modes N with respect to crystal thickness L for object distances $d = 3\text{cm}, 5\text{cm}, 10\text{cm}, 30\text{cm}$ using photon pairs with non-degenerate wavelengths with $\lambda_l = 700\text{nm}$: (a,c) $\lambda_s/\lambda_l = 1/4$, (b,d) $\lambda_s/\lambda_l = 4$.

5. Metasurface-assisted quantum ghost polarimetry

We have shown in the previous chapters that entangled signal and idler photons, produced by spontaneous parametric down-conversion, can be used for imaging the transverse profile of an object by using a camera that measures photons that never interacted with the object. This is the case for quantum ghost imaging (QGI) and quantum imaging with undetected photons (QIUP). In this chapter, we present the theoretical treatment of quantum ghost polarimetry (QGP), which is a scheme similar to QGI with the difference that it uses exclusively the polarization degree of freedom of photon pairs. Importantly, just like QGI, QGP has additionally the advantage that signal and idler photons can be used at different wavelengths, which is relevant for applications in biosensing. Therefore, QGP allows us to find the polarization response of samples by probing them with low-light and a long wavelength, while the resolving measurement can be done in the visible range with a shorter wavelength, where most cameras are highly efficient. Moreover, a novel concept of metasurface-assisted QGP is presented in this chapter to discriminate polarization-sensitive objects.

This chapter is organized as follows. First, we discuss the basics of QGP. Second, we propose a protocol to discriminate polarization-sensitive objects using QGP. Third, we show that by placing specially designed metasurfaces before the polarization-insensitive photon detectors, one can perform real-time discrimination between fully or partially transparent polarization-sensitive objects within a defined set by using only a few parallel coincidence measurements. Lastly, we analyze the difference between using a source of photons with entanglement and a source with classical correlations.

5.1. Quantum ghost polarimetry

5.1.1. Two-photon state including the object

In contrast to QGI, which was presented in the previous chapters, QGP constitutes a much simpler scheme as it can be fully described with a two-mode polarization basis

for signal and idler photons. A simplified QGP scheme is illustrated in Fig. 5.1. It consists of a source of polarization-entangled photons, then the idler photons interact with an object, defined by the Jones matrix T_I , and the idler photons are then measured by a polarization-insensitive detector. Signal photons do not interact with T_I but do interact with the object T_S and are also measured later by a polarization-insensitive detector. The goal of QGP is to obtain the polarization information of the object T_I , by performing a measurement that resolves polarization in the signal arm. That is, the object T_S is designed so that it allows to resolve the polarization state of the signal photons. In contrast in QGI, a camera was used in the signal arm to resolve position.

The two-photon state of signal and idler photons that are entangled in polarization, as described in section 2.2.2, can be written as

$$|\psi\rangle = C [\hat{a}^\dagger(H_I)\hat{a}^\dagger(H_S) + \hat{a}^\dagger(V_I)\hat{a}^\dagger(V_S)]|0,0\rangle \quad (5.1)$$

where C is a constant, \hat{a}^\dagger is the creation operator and $|0,0\rangle$ is the vacuum state. Here, it is considered that the orthogonal basis of the polarization consists of horizontal (H) and vertical (V) polarizations.

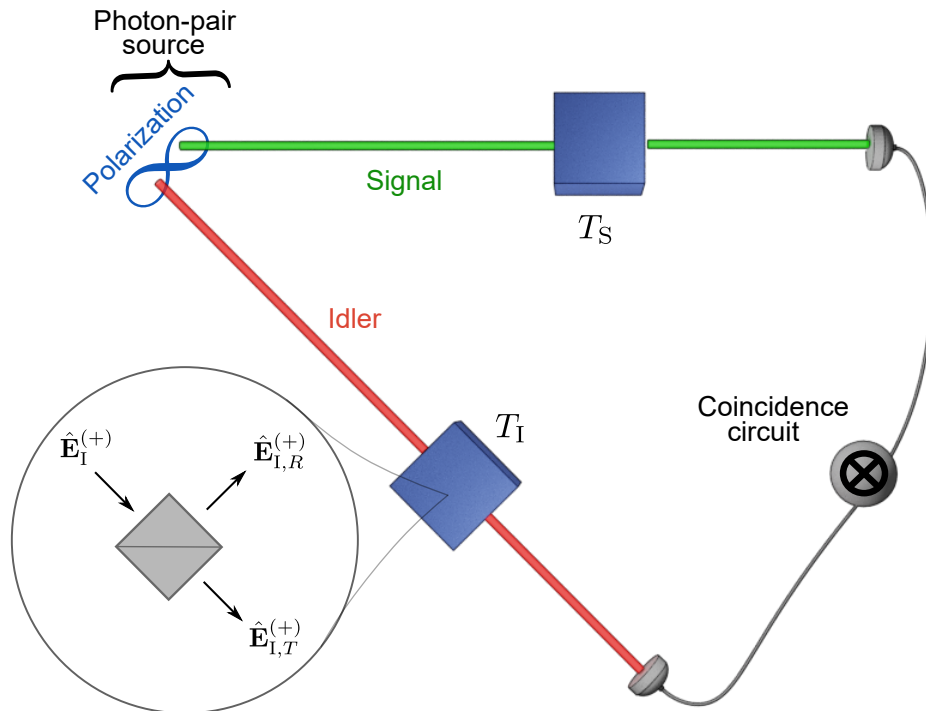


Figure 5.1. Sketch of a simplified quantum ghost polarimetry (QGP) scheme. Signal and idler photons are entangled in polarization, where the object, defined by the Jones matrix T_I , interacts with idler photons. The idler photons are then measured by a polarization-insensitive detector, while the signal photons, which do not interact with T_I , go through the object T_S that is designed to resolve polarization. The inset shows the model of the object as a beamsplitter.

As sketched in Fig. 5.1, an object in the idler arm of the scheme would act on the polarization state of the idler photons. As in the previous chapter, the object is modeled using a lossless beamsplitter with transmission T_I and reflection R_I , each of them is a 2×2 Jones matrix of the form

$$T_I = \begin{bmatrix} T_{HH} & T_{HV} \\ T_{VH} & T_{VV} \end{bmatrix}, \quad (5.2a)$$

$$R_I = \begin{bmatrix} R_{HH} & R_{HV} \\ R_{VH} & R_{VV} \end{bmatrix}. \quad (5.2b)$$

Here, we assume that the unit vectors corresponding to the horizontal and vertical polarizations are given by $\mathbf{e}(H) = [1 \ 0]^T$ and $\mathbf{e}(V) = [0 \ 1]^T$, respectively. Additionally, since the beamsplitter is lossless,

$$T_I T_I^* + R_I R_I^* = \mathbb{1}, \quad (5.3)$$

one of the inputs of the beamsplitter is $\hat{\mathbf{E}}_I^{(+)}$ and the other is the vacuum $\hat{\mathbf{E}}_0^{(+)}$. The input field operator $\hat{\mathbf{E}}_I^{(+)}$, which is collinear with the output $\hat{\mathbf{E}}_{I,T}^{(+)}$, can be expressed in terms of the output operators $\hat{\mathbf{E}}_{I,T}^{(+)}$ and $\hat{\mathbf{E}}_{I,R}^{(+)}$ by [184]

$$\hat{\mathbf{E}}_I^{(+)} = T_I^\dagger \hat{\mathbf{E}}_{I,T}^{(+)} + R_I^\dagger \hat{\mathbf{E}}_{I,R}^{(+)}, \quad (5.4)$$

where the electric field operator is obtained by simplifying Eq. (2.13), leaving the polarization degree of freedom by assuming that the spatial distribution can be approximated to just one plane wave as mentioned in section 2.2.2. This leads to an electric field operator

$$\hat{\mathbf{E}}^{(+)} = C' [\hat{a}(H_I)\mathbf{e}(H_I) + \hat{a}(V_I)\mathbf{e}(V_I)]. \quad (5.5)$$

Therefore, by introducing Eqs. (5.2) and (5.5) in Eq. (5.4), we obtain the relation of the input annihilation operators in terms of the output annihilation operators,

$$\hat{a}(H_I) = T_{HH}^* \hat{a}_T(H_I) + T_{VH}^* \hat{a}_T(V_I) + R_{HH}^* \hat{a}_R(H_I) + R_{VH}^* \hat{a}_R(V_I), \quad (5.6a)$$

$$\hat{a}(V_I) = T_{HV}^* \hat{a}_T(H_I) + T_{VV}^* \hat{a}_T(V_I) + R_{HV}^* \hat{a}_R(H_I) + R_{VV}^* \hat{a}_R(V_I). \quad (5.6b)$$

To simplify the notation from this point onward, we use

$$|H\rangle = \hat{a}^\dagger(H) |0\rangle, \quad (5.7a)$$

$$|V\rangle = \hat{a}^\dagger(V) |0\rangle, \quad (5.7b)$$

therefore, Eq. (5.6) becomes

$$|H_I\rangle = T_{HH}^* |H_{I,T}\rangle + T_{VH}^* |V_{I,T}\rangle + R_{HH}^* |H_{I,R}\rangle + R_{VH}^* |V_{I,R}\rangle, \quad (5.8a)$$

$$|V_I\rangle = T_{HV}^* |H_{I,T}\rangle + T_{VV}^* |V_{I,T}\rangle + R_{HV}^* |H_{I,R}\rangle + R_{VV}^* |V_{I,R}\rangle. \quad (5.8b)$$

Plugging Eq. (5.8) into the two-photon state of Eq. (5.1), we find

$$\begin{aligned} |\psi\rangle = & C \left[T_{HH} |H_{I,T}H_S\rangle + T_{VH} |V_{I,T}H_S\rangle + T_{HV} |H_{I,T}V_S\rangle + T_{VV} |V_{I,T}V_S\rangle \right] \\ & + C \left[R_{HH} |H_{I,R}H_S\rangle + R_{VH} |V_{I,R}H_S\rangle + R_{HV} |H_{I,R}V_S\rangle + R_{VV} |V_{I,R}V_S\rangle \right]. \end{aligned} \quad (5.9)$$

which is the general state of the system that includes an object T_I in the idler arm.

5.1.2. Reduced density matrix of the signal photon

Here, we build upon the previous section and resort to a more general approach to study the central characteristics of the QGP scheme, namely, by using the density matrix representation of the quantum state. The purpose of using the density matrix is twofold: First, the reduced density matrix of the signal photon after the idler photon is measured leads to a much more intuitive description and design of the QGP scheme. Second, the role of entanglement can be easily investigated.

If the idler photons are measured by a polarization-insensitive detector, then the state of the system is reduced to describing the state of only the signal photons. Importantly, due to the entanglement between signal and idler, the reduced state of the signal photons will also contain information about the idler arm. This is known as remote state preparation [211, 212]. The reduced state of the signal photon after the idler photon is measured becomes the central pillar for the forthcoming analysis of the QGP scheme. We begin by writing the input state of the photon pairs of SPDC $|\psi\rangle_{\text{SPDC}} = |0, 0\rangle + |\psi\rangle$ of Eq. (2.1) in terms of the density matrix, namely,

$$\begin{aligned} \rho_{\text{SPDC}} &= |\psi\rangle_{\text{SPDC}} \langle\psi|_{\text{SPDC}} \\ &= |0, 0\rangle \langle 0, 0| + \rho + |0, 0\rangle \langle\psi| + |\psi\rangle \langle 0, 0|, \end{aligned} \quad (5.10)$$

where the density matrix of the two-photon state ρ , considering Eq. (5.1), is

$$\begin{aligned} \rho &= |\psi\rangle \langle\psi| \\ &= |C|^2 \left[|H_I H_S\rangle \langle H_I H_S| + |V_I V_S\rangle \langle V_I V_S| + \kappa \left(|H_I H_S\rangle \langle V_I V_S| + |V_I V_S\rangle \langle H_I H_S| \right) \right]. \end{aligned} \quad (5.11)$$

At this point, it is appropriate to introduce the degree of entanglement, represented by κ , which lies between the range $0 \leq \kappa \leq 1$. The degree of entanglement weights

the role of the coherent term in the density matrix ρ . Therefore, κ allows us to model from the classical correlation $\kappa = 0$ to the maximal entanglement $\kappa = 1$. It should be noted that κ is equal to the entanglement measure called concurrence [213], which in turn is related to the Bell parameter [3] by $S = \sqrt{2}(1 + \kappa)$. The introduction of κ will allow us to dwell on the analysis of the role of entanglement in the QGP scheme, which is presented later in section 5.4.

After measuring the idler photon with a polarization-insensitive detector, the reduced state of the signal photon is determined according to the principle of remote state preparation [211] by

$$\rho'_S = \text{tr}_I(\rho_{\text{SPDC}}) = \langle H_{I,T} | \rho_{\text{SPDC}} | H_{I,T} \rangle + \langle V_{I,T} | \rho_{\text{SPDC}} | V_{I,T} \rangle \quad (5.12)$$

where $\text{tr}_I(\cdot)$ is the partial trace over the idler photon with ρ_{SPDC} containing the Jones matrices T_I and R_I of the object, following the treatment of the previous section. The projection is done on both horizontal and vertical polarizations to model a polarization-insensitive detector in the idler arm. This is achieved by the terms $|H_{I,T}\rangle$ and $|V_{I,T}\rangle$ that model the measurement only on the idler arm and leave the signal arm untouched. Consequently, the reduced state of the signal photon is

$$\begin{aligned} \rho'_S = & |C|^2 [(|T_{\text{HH}}|^2 + |T_{\text{VH}}|^2) |H_S\rangle \langle H_S| + (|T_{\text{HV}}|^2 + |T_{\text{VV}}|^2) |V_S\rangle \langle V_S|] \\ & + \kappa |C|^2 [(T_{\text{HH}} T_{\text{HV}}^* + T_{\text{VH}} T_{\text{VV}}^*) |H_S\rangle \langle V_S| + (T_{\text{HV}} T_{\text{HH}}^* + T_{\text{VV}} T_{\text{VH}}^*) |V_S\rangle \langle H_S|]. \end{aligned} \quad (5.13)$$

The normalized reduced state of the signal photon is then $\rho_S = \rho'_S / \text{tr}(\rho'_S)$.

The expression derived from the reduced state of the signal photon derived in Eq. (5.13) contains information of the transmission Jones matrix of the object T_I . However, the form of ρ'_S is involved when one tries to understand the actual characteristics of the object in the idler arm. Thus, we resort to a well-known geometrical representation of the two-level quantum state to gain more insight.

In general terms, the state ρ_0 of any two-level system can be represented in the Bloch sphere by

$$\rho_0 = \frac{1}{2} (1 + a_x X + a_y Y + a_z Z) \quad (5.14)$$

where $a_{x,y,z}$ are the components of the Bloch vector and X, Y, Z are the Pauli matrices. The Bloch vector is simply found by $\mathbf{a} = [\text{tr}(\rho_0 X), \text{tr}(\rho_0 Y), \text{tr}(\rho_0 Z)] = [a_x, a_y, a_z]$. In the scheme under study, the modes represent polarization and, therefore, the Bloch

sphere is replaced by the Poincaré sphere [214] with Poincaré vector

$$\mathbf{p} = [\text{tr}(\rho_0 Z), \text{tr}(\rho_0 X), -\text{tr}(\rho_0 Y)] = [p_H, p_D, p_C]. \quad (5.15)$$

In detail, p_H quantifies the degree of horizontal ($0 < p_H \leq 1$) or vertical polarization ($-1 \leq p_H < 0$), p_D represents the degree of diagonal $[(|H\rangle + |V\rangle)/\sqrt{2}]$ with $0 < p_D \leq 1$ or antidiagonal ($-1 \leq p_D < 0$) linear polarization at $\pm 45^\circ$, and p_C represents the degree of the right $[(|H\rangle - i|V\rangle)/\sqrt{2}]$ with $0 < p_C \leq 1$ or left ($-1 \leq p_C < 0$) circular polarization. The terms p_H, p_D, p_C correspond to the well-known Stokes parameters commonly denoted with s_1, s_2, s_3 [158], respectively.

Based on this geometric representation of the state in the Poincaré sphere, each reduced state of the signal photon ρ_S can be described by the vector $\mathbf{p} = [p_H, p_D, p_C]$. In particular, we found that if the object T_1 is treated with the matrices of its singular value decomposition, then each component of the vector \mathbf{p} can be expressed in a compact expression. In general terms, the singular value decomposition of a matrix T consists of three matrices $T = U\Sigma V^\dagger$, where the columns of U (V) are the left (right) singular vectors and Σ is a diagonal matrix that contains the singular values. Taking into account that T_1 is a 2×2 Jones matrix and that the matrices U and V are unitary, i.e., $U^\dagger U = 1$ and $V^\dagger V = 1$, then the matrices can be expressed in a general form as follows,

$$U = \begin{bmatrix} \cos(\alpha_1) \exp(i\alpha_2) & \sin(\alpha_1) \exp(i\alpha_3) \\ -\sin(\alpha_1) \exp(-i\alpha_3) & \cos(\alpha_1) \exp(-i\alpha_2) \end{bmatrix} \quad (5.16a)$$

$$\Sigma = \begin{bmatrix} \sigma_{11} & 0 \\ 0 & \sigma_{21} \end{bmatrix} \quad (5.16b)$$

$$V = \begin{bmatrix} \cos(\beta_1) \exp(i\beta_2) & \sin(\beta_1) \exp(i\beta_3) \\ -\sin(\beta_1) \exp(-i\beta_3) & \cos(\beta_1) \exp(-i\beta_2) \end{bmatrix} \quad (5.16c)$$

where $\alpha_{1,2,3}$ and $\beta_{1,2,3}$ are real numbers. Additionally, σ_{11} and σ_{21} stand for the singular values, which are non-negative numbers. Using $T_1 = U\Sigma V^\dagger$, then the components of the reduced state of the signal photon represented in the Poincaré sphere \mathbf{p} are

$$p_H = \text{tr}(\rho_S Z) = \cos(2\beta_1) \left(\frac{\sigma_{11}^2 - \sigma_{21}^2}{\sigma_{11}^2 + \sigma_{21}^2} \right), \quad (5.17a)$$

$$p_D = \text{tr}(\rho_S X) = -\kappa \sin(2\beta_1) \cos(\beta_2 + \beta_3) \left(\frac{\sigma_{11}^2 - \sigma_{21}^2}{\sigma_{11}^2 + \sigma_{21}^2} \right), \quad (5.17b)$$

$$p_C = -\text{tr}(\rho_S Y) = \kappa \sin(2\beta_1) \sin(\beta_2 + \beta_3) \left(\frac{\sigma_{11}^2 - \sigma_{21}^2}{\sigma_{11}^2 + \sigma_{21}^2} \right). \quad (5.17c)$$

Finally, the presence of the trigonometric terms of Eqs. (5.17a - 5.17c) suggests that there is a closed-form expression that relates the components of the Poincaré vector, namely we found that

$$p_H^2 + \frac{p_D^2 + p_C^2}{\kappa^2} = \eta^2 = \left(\frac{\sigma_{11}^2 - \sigma_{21}^2}{\sigma_{11}^2 + \sigma_{21}^2} \right)^2. \quad (5.18)$$

This compact relation describes an ellipsoid of revolution of long axis η and short axis $\kappa\eta$, where $0 \leq \eta \leq 1$ and κ is the degree of entanglement. In other words, Eq. (5.18) indicates that the reduced state of the signal photon ρ_S obtained from the family of matrices T_1 that have the same η , will lie on the same ellipsoid of revolution inside or on the Poincaré sphere. Notice that this ellipsoid reduces to a point, $p_H = p_D = p_C = 0$, when $\sigma_{11} = \sigma_{21}$. Additionally, the ellipsoid is largest for a fixed κ that lies within $0 \leq \kappa \leq 1$, when one of the singular values is zero, resulting in $\eta = 1$. Equation (5.18) will play a major role in the understanding and design of QGP as will be discussed later.

5.1.3. Coincidence counting rate

As already mentioned, the measurement protocol of QGP requires one to measure the coincidence counting rate of the signal and idler photons to reveal the information of the object. In the previous section, the reduced state of the signal was found after idler photons were measured. In this section, we analyze the details of the remaining measurement of the signal photons to extract the characteristics of the polarization-sensitive object.

It has been shown that four projective measurements are sufficient to fully determine the polarization state of a photon [87]; however, depending on the example, one could perform fewer projective measurements; therefore, an appropriate design of the projective measurements can alleviate the experimental workload. As an example, consider a photon that is linearly polarized, then by using a common polarizing beamsplitter one could measure the degree of horizontal and vertical polarization of such incoming photon and find the orientation of its linear polarization. However, if the polarization is elliptical, then the mentioned projective basis of the polarizing beamsplitter would not allow us to reconstruct the complete incoming polarization because information about the relative phase is missing. The needed phase can indeed be obtained by adding more components into the measurement, these then realize a more adequate projective basis than a common polarizing beamsplitter. In the next analysis in this section, we focus on describing a model of the scheme with general projective bases. Later, in a dedicated section, an actual implementation of such found

bases using dielectric metasurfaces is discussed.

In the previous section, we only mentioned the singular values of the transmission T_I acting on the quantum state as these values appeared naturally in the derivation; however, the singular vectors of T_I become also relevant for the rest of the analysis. If an object defined by the Jones matrix T acts on a quantum state described by a density matrix ρ_0 , then the expectation value of the measurement I can be found by [184]

$$I = \text{tr}(T\rho_0T^\dagger) = \text{tr}[(\Sigma V^\dagger)\rho_0(V\Sigma)], \quad (5.19)$$

where we have used the cyclic property of the trace $\text{tr}(ABC) = \text{tr}(BCA)$ and the fact that U is unitary, $U^\dagger U = 1$. This shows that the expectation value I does not depend on the left singular vectors of T and can be written as

$$\begin{aligned} I &= \frac{\sigma_1^2}{2}(1 + \mathbf{a} \cdot \mathbf{A}_1) + \frac{\sigma_2^2}{2}(1 + \mathbf{a} \cdot \mathbf{A}_2) \\ &= \frac{1}{2}(\sigma_1^2 + \sigma_2^2) + \frac{1}{2}(\mathbf{a} \cdot \mathbf{A}_1)(\sigma_1^2 - \sigma_2^2), \end{aligned} \quad (5.20)$$

where $\mathbf{A} = [A_x, A_y, A_z]$ is the representation of a right singular vector in the Bloch sphere and \mathbf{a} is the Bloch vector mentioned previously. The vector \mathbf{A}_1 is given by

$$A_{x1} = \text{tr} \left[\left(\begin{bmatrix} 1 & 0 \\ 0 & 0 \end{bmatrix} V^\dagger \right) X \left(V \begin{bmatrix} 1 & 0 \\ 0 & 0 \end{bmatrix} \right) \right], \quad (5.21a)$$

$$A_{y1} = \text{tr} \left[\left(\begin{bmatrix} 1 & 0 \\ 0 & 0 \end{bmatrix} V^\dagger \right) Y \left(V \begin{bmatrix} 1 & 0 \\ 0 & 0 \end{bmatrix} \right) \right], \quad (5.21b)$$

$$A_{z1} = \text{tr} \left[\left(\begin{bmatrix} 1 & 0 \\ 0 & 0 \end{bmatrix} V^\dagger \right) Z \left(V \begin{bmatrix} 1 & 0 \\ 0 & 0 \end{bmatrix} \right) \right]. \quad (5.21c)$$

To arrive to the final expression of Eq. (5.20), we used the fact that the singular vectors form an orthonormal basis, i.e., $\mathbf{A}_2 = -\mathbf{A}_1$. Furthermore, as mentioned earlier, since QGP works with the state of light polarization, we translate the representation of the Bloch sphere to the Poincaré sphere with $\mathbf{p} = [a_z, a_x, -a_y]$ and therefore the right singular vector represented in the Poincaré sphere is $\mathbf{m} = [A_z, A_x, -A_y]$.

Now, consider the Jones matrix T_S in the signal arm of the QGP scheme, as shown in Fig. 5.1. Then, the expectation value of the reduced state ρ_s after interacting with T_S corresponds to the expectation value of the coincidence counting rate between signal and idler, denoted here by Γ . The reason for this correspondence is that the reduced state ρ_s , represented in the Poincaré sphere with \mathbf{p} , includes the fact that the idler was

already measured. Therefore, the coincidence counting rate in QGP is

$$\Gamma = \frac{1}{2}(\sigma_{1s}^2 + \sigma_{2s}^2) + \frac{1}{2}(\mathbf{p} \cdot \mathbf{m}_{1s})(\sigma_{1s}^2 - \sigma_{2s}^2), \quad (5.22)$$

where σ_s stands for a singular value of the Jones matrix T_s , and \mathbf{m}_s is its right singular vector represented in the Poincaré sphere.

The basic building blocks of QGP are essentially the reduced density matrix of the signal represented in the Poincaré sphere of Eq. (5.18) and the coincidence rate of Eq. (5.22). The way we expressed these equations constitutes a more amiable form to understand and design the QGP scheme in a graphical geometrical way, as will be clear in the next section, where we discuss the discrimination of polarization-sensitive objects in a QGP scheme.

5.2. Discrimination of polarization-sensitive objects

The task of discriminating objects from a given known set, based on their respective polarization response, is relevant in many applications, for example in the fields of biology and medical diagnostics. The available information on the Jones matrix of each object T_i in the set allows us to design a QGP scheme with a minimal number of measurements, as will be shown in this section, by choosing objects with optimal Jones matrices in the idler and/or signal arm, in addition to T_i . Therefore, the coincidence counting rate, obtained when a specific object from the set is probed, is unique for such an object so it unequivocally identifies it from the rest.

The basis of the proposed discrimination method uses Eq. (5.18), which gives a strict mathematical, yet intuitive geometric understanding of the discrimination problem using the reduced state ρ_s represented in the Poincaré sphere, as will be shown. To realize the discrimination task, we require that each object produce a different reduced state, each ρ_s must occupy a unique position on or inside the Poincaré sphere, which can then later be identified in the coincidence measurements. The method will now be showcased with an example in which the aim is to discriminate three polarization-sensitive objects and also the rotation angle θ of each of these objects around the longitudinal axis. Importantly, we concentrate for the moment on a scheme with a source of photon pairs that have maximal entanglement $\kappa = 1$, where the ellipsoid of Eq. (5.18) is a sphere with radius η . As a last step, we design the Jones matrices in the signal arm so that coincidence rates [Eq. (5.22)] given by each object in the set and angle are unique.

The chosen set of objects is composed by the following Jones matrices

$$\Omega_a = \begin{bmatrix} 1 & 0 \\ 0 & \exp(i\pi/2) \end{bmatrix}, \quad (5.23a)$$

$$\Omega_b = \begin{bmatrix} 1 & 0 \\ 0 & \exp[i(\pi/2 + 0.7i)] \end{bmatrix}, \quad (5.23b)$$

$$\Omega_c = \begin{bmatrix} 1 & 0 \\ 0 & 0 \end{bmatrix}, \quad (5.23c)$$

which respectively correspond to a transparent object Ω_a (quarter-wave plate) with singular values $\sigma_{1\Omega} = \sigma_{2\Omega} = 1$, a partially transparent object Ω_b with $\sigma_{1\Omega} = 1$ and $\sigma_{2\Omega} = 0.5$, and a fully polarizing object Ω_c (horizontal polarizer) with $\sigma_{1\Omega} = 1$ and $\sigma_{2\Omega} = 0$. These definitions correspond to an object rotation angle $\theta = 0$, with respect to the horizontal polarization. Since rotation is a unitary transformation, the singular values of each object remain the same and the associated reduced states of the signal photons lie on a sphere with a radius defined by Eq. (5.18) for all object angles. Since the goal includes the identification of the rotation angle, it is expected that we obtain a continuous collection of reduced states ρ_s in the interval $0 \leq \theta < \pi$ given that the objects considered have a rotation symmetry of π .

In the top row of Fig. 5.2, we illustrate the reduced state of the signal photon in the Poincaré sphere for the three objects, each in a different column, and their rotations. The first row represents the scenario, where there is only free space between the object and the detector in the idler arm; therefore, $T_1 = \Omega$. In this case, a fully transparent wave-plate Ω_a produces reduced states that lie on a single point in the origin for all angles, in agreement with Eq. (5.18), given that $\sigma_1 = \sigma_2$ which is a characteristic of phase objects. Therefore, discrimination between transparent phase objects and their rotations cannot be achieved, unless one introduces an additional element in the idler arm with the purpose of acting on the polarization of the idler photon. On the other hand, the other objects in the given set, Ω_b and Ω_c , do produce distinctive reduced states for each rotation angle which result in circles with different radii in the Poincaré sphere, allowing us to discriminate these two objects.

A solution to the problem of distinguishing all three objects in the set and their rotations is to engineer the Jones matrix of an object, named here M_1 , and include it after the object and before the polarization-insensitive detector of the idler arm, leading to $T_1 = M_1\Omega$. A versatile platform to implement the appropriate M_1 will be discussed in the next section. In the left column of Fig. 5.2, we show in the Poincaré sphere the two orthonormal right singular vectors of M_1 , denoted by \mathbf{m}_{j1} with $j \in$

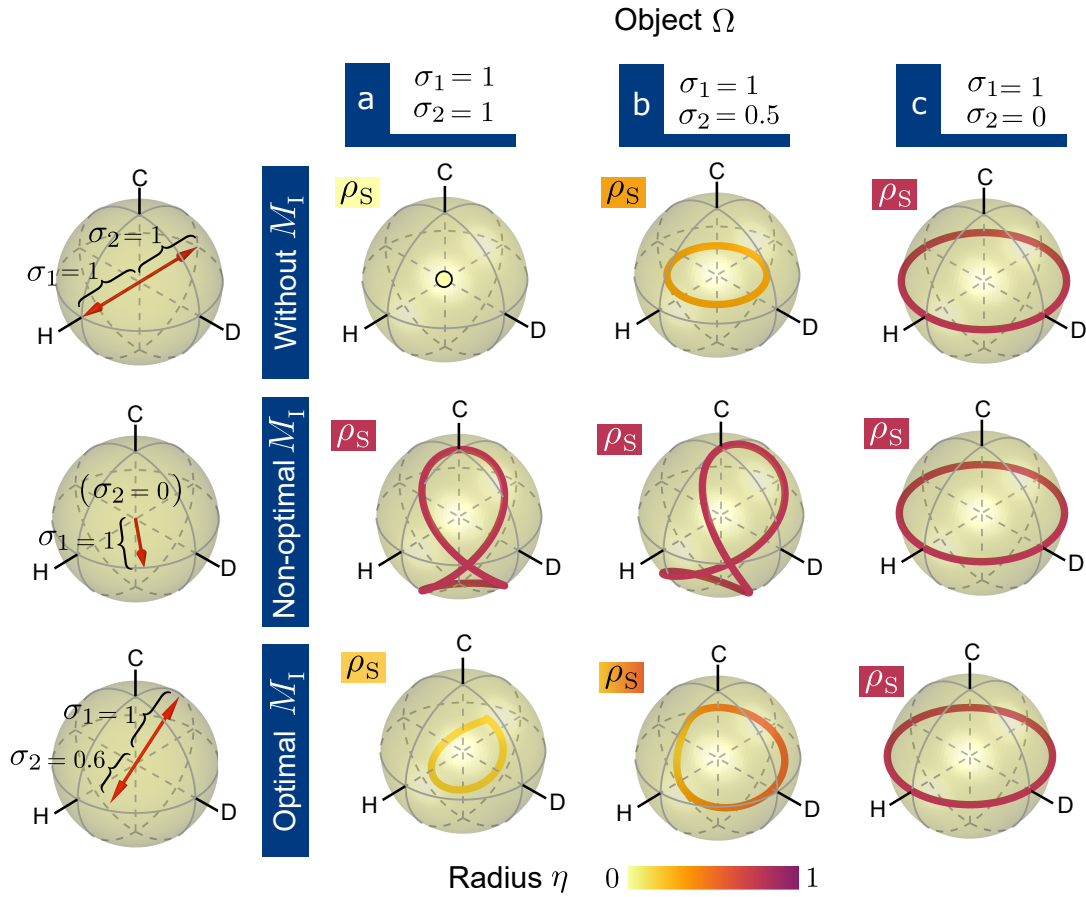


Figure 5.2. Jones matrix M_I enabling object discrimination. Left column: The singular eigenvectors of M_I , scaled by the corresponding singular values, represented in the Poincaré sphere for the cases of (upper row) without M_I , (middle row) fully polarizing object, (lower row) optimal partially polarizing case. The axes of the Poincaré sphere correspond to horizontal (H), diagonal (D) and right circular (C) polarizations. (a-c) Reduced states of the signal photon after measuring the idler photon ρ_S produced by a set of three objects $\Omega_{a,b,c}$, for different M_I in each row. The curves are formed from the points corresponding to different object rotation angles in the range $0 \leq \theta < \pi$.

$\{1,2\}$, as explained in the previous section, whose magnitude has been scaled with their corresponding singular value σ_{ji} . In the case explained before where M_I was absent, the free space between the object and the detector corresponds to $M_I = \mathbb{1}$ with $\sigma_1 = \sigma_2 = 1$.

In Fig. 5.2 (second row), we illustrate a case of a fully polarizing object M_I with $\sigma_{2p} = 0$, such that only one polarization is transmitted by a quantum projection measurement for the state \mathbf{m}_{1p} . Note that if an object Ω and/or M_I has one singular value equal to zero, then its product, $T_I = M_I \Omega$, also has one zero singular value. This causes, according to Eq. (5.18), the reduced state of the signal photon to lie on the surface of the Poincaré sphere. Consequently, not all objects and rotation angles can be distinguished since the closed loops formed by the objects' reduced states would cross. Thus, to enable the desired discrimination of the three objects in this given set, the ra-

tio of the smaller to larger singular values of M_I has to be in the range $0 < \sigma_2/\sigma_1 < 1$, i.e., M_I should realize a partially polarizing Jones matrix. Additionally, its largest singular value, according to convention σ_1 , should be close to one so that high photon counts are obtained, as shown by Eq. (5.20). The reduced states for a numerically optimized polarization basis¹ of M_I are shown in Fig. 5.2 (third row) which results in an object with partial polarization. The reduced states do not cross and, therefore, are distinguishable, confirming the above analysis of the needed ratio of singular values of M_I . The displayed elliptical polarization basis of M_I is formed by its two orthonormal right singular vectors, represented by arrows in the plot in the lower left corner.

Once the optimal M_I in the idler arm is found, then also an object with Jones matrix $T_S = M_S$ in the signal arm should be properly engineered to extract the polarization state of any reduced state of the signal photon. In the next section, we will discuss in more detail the optimal M_S taking into account the constraints of the platform where the Jones matrix will be realized.

5.3. Metasurface as a versatile platform

The QGP scheme, as discussed in the previous sections, consists of a detector in the idler arm that simply collects idler photons that interacted with the object and consequently does not allow us to recover the full polarization state of the idler photon. The information of the object can be retrieved in the coincidence counting rate between a *polarization-resolving measurement* in the non-interacting signal arm and the idler detector. Here, we will discuss a platform for realizing such resolving measurement.

What elements are necessary to resolve polarization? The well-known polarizing beamsplitter can be thought of as a fully polarizing optical element that has two outputs. It essentially projects the incoming polarization state into the horizontal and vertical polarizations, and delivers the two projections spatially separated. In case projections in more complex bases are needed, several bulk elements including beamsplitters and wave-plates need to be used. State-of-the-art technology has proven that photons can be easily manipulated with metasurfaces [134]. In particular, an all-dielectric metasurface is an integrated optical element that can produce several outputs realized by its diffraction orders; therefore, a metasurface is an alternative to aligning a collection of bulk elements. Importantly, each output of the metasurface can be designed so that it corresponds to a desired photon projective basis, in general, partial polarizers in arbitrary elliptical bases can be realized with a single metasur-

¹ The optimal object M_I was found by minimizing a cost function defined by the chosen set of objects in the example, that ensures that geometrically all the reduced states are apart in the Poincaré sphere. The minimization was performed using a simplex algorithm.

face [87]. Therefore, the implementation using this platform has the advantage that many projections can be performed in parallel.

As already mentioned, a complete tomographic reconstruction of a polarization state can be achieved with four projections [215]. Therefore, one can design a single metasurface that realizes four diffraction orders of the full tomographic basis, which leads to having four measurements to reconstruct the quantum state. However, in this particular case of study that requires to discriminate objects of a known set, less than four measurements could be optimized to identify an object, as we will demonstrate. The use of fewer outputs of the metasurface has the advantage of not only simplifying the experimental measurements but also improving signal-to-noise ratio since photon counts are concentrated in fewer outputs.

5.3.1. Modeling an all-dielectric metasurface

A metasurface is a flat optical element composed of a periodically repeated array of nano-resonators called meta-gratings, see Fig. 5.3, where, an input beam gets diffracted into several output diffraction orders based on the meta-grating design. Optimization is carried out on the phase retardances and orientations associated with each nano-resonator to realize the required Jones matrix that acts on the state of the input. Each dielectric nano-resonator located at position x of a metasurface can be represented as a rotated phase-retarder, within the Jones formalism, as

$$T(\theta, \phi_1, \phi_2; x) = \begin{bmatrix} \cos \theta & -\sin \theta \\ \sin \theta & \cos \theta \end{bmatrix} \begin{bmatrix} \exp(i\phi_1) & 0 \\ 0 & \exp(i\phi_2) \end{bmatrix} \begin{bmatrix} \cos \theta & \sin \theta \\ -\sin \theta & \cos \theta \end{bmatrix}, \quad (5.24)$$

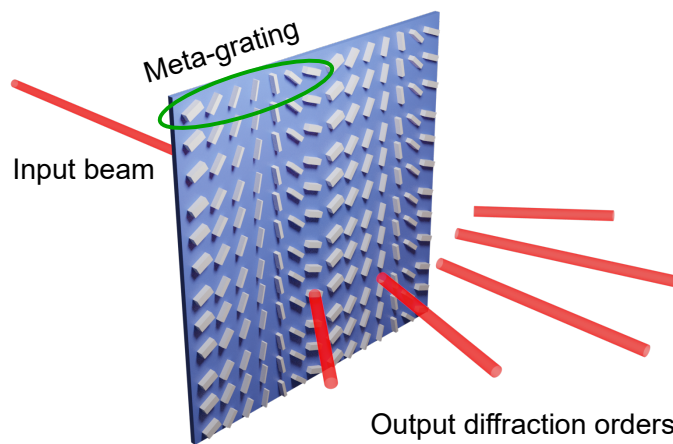


Figure 5.3. Schematic of an all-dielectric metasurface composed of periodically repeated meta-gratings. Output diffraction orders are produced upon the incidence of an input beam.

that results in a symmetric matrix, i.e., $T_{12} = T_{21}$. The collective behavior of the nano-resonators form diffraction orders in the far field, just like a conventional dielectric grating. The diffraction orders are found by taking the Fourier series \mathcal{F} of the ensemble $T(x)$ along x . The periodicity of the meta-gratings is automatically considered by calculating the Fourier series. Thus, each resulting diffraction order at position x' in the far field is defined by the symmetric transfer matrix

$$M(x') = \begin{bmatrix} \mathcal{F}(T_{11}) & \mathcal{F}(T_{12}) \\ \mathcal{F}(T_{21}) & \mathcal{F}(T_{22}) \end{bmatrix}. \quad (5.25)$$

Thus, the Jones matrix realized in each diffraction order depends on all the nano-resonators in the meta-grating, each defined by its own parameters θ, ϕ_1, ϕ_2 . To optimize the design of the metasurface, a numerical optimization algorithm finds the most adequate parameters for each nano-resonator so that each diffraction order M realizes a required polarization basis. Specifically, in the proposed QGP scheme, the metasurface for the idler arm is designed such that its zeroth diffraction order realizes M_I . In the same way, the metasurface in the signal arm M_S is optimized with the difference that M_S is polarization-resolving using several outputs corresponding to many diffraction orders, allowing us to have parallel projections that would otherwise be difficult to implement with bulk elements.

5.3.2. Engineering the metasurfaces for object discrimination

The complete QGP scheme for discrimination is illustrated in Fig. 5.4, which includes the photon-pair source, the object Ω and rotation angle θ , metasurfaces M_I and M_S , and polarization-insensitive detectors to measure coincidences. Several diffraction orders of M_S are measured, while just one diffraction order of M_I is measured.

We will show in the following that metasurfaces can be optimized to realize Jones matrices M_I in the idler arm and M_S in the signal arm so that every reduced state ρ_S produces a distinctive pattern formed by a collection of coincidence measurements, thereby allowing discrimination between the objects.

We begin by considering that the expectation values of the coincidence counts between the signal and idler detectors, which are located after the metasurfaces, is

$$\Gamma_n = \text{tr}[(M_{S,n})\rho_S(M_{S,n})^\dagger], \quad (5.26)$$

where n simply denotes the output of the signal metasurface. For the sake of easing the visualization later on, the output pattern in coincidences will be geometrically represented in a space \mathcal{D} such that each coincidence expectation value Γ_n corresponds

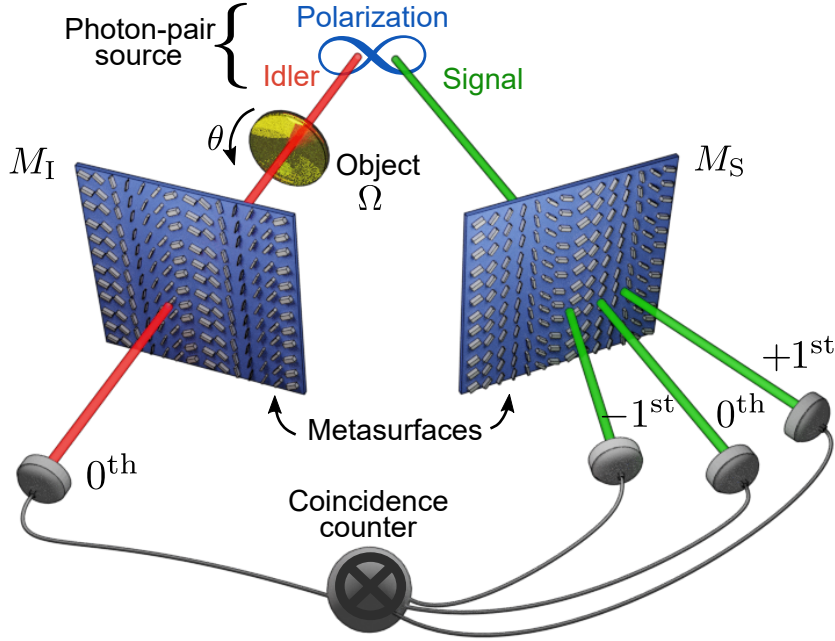


Figure 5.4. Complete metasurface-assisted QGP scheme for discrimination of polarization objects Ω and their orientation angles θ through coincidence measurements.

to a coordinate along the n -th dimension and each pattern in coincidences is mapped as a point in \mathcal{D} .

To achieve practically relevant solutions for the design of the metasurface in the signal arm, we impose two additional conditions: object identification must be achieved using a small number of outputs, and the total number of photon counts in all outputs should be larger than zero for any object. One approach to fulfill the requirement of non-zero photon counts consists of having equal singular values for all outputs of the metasurface M_S is that $\sigma_{1S,n} = \sigma_{1S}$ and $\sigma_{2S,n} = \sigma_{2S}$, and also that the sum of their right singular vectors to be equal to zero, $\sum_n \mathbf{m}_{1S,n} = 0$. Thus, using Eq. (5.22)

$$\sum_n \Gamma_n = \frac{1}{2} \sum_n (\sigma_{1S,n}^2 + \sigma_{2S,n}^2) = \frac{n}{2} (\sigma_{1S}^2 + \sigma_{2S}^2), \quad (5.27)$$

that is a constant different from zero, meaning that the photon counts will be non-zero. If we consider M_S with three outputs, the condition $\sum_n \mathbf{m}_{1S,n} = 0$ would indicate that each pair of right singular vectors in the Poincaré sphere \mathbf{m} encloses an angle of 120° and they would all lie in one plane in the Poincaré sphere. Then this plane has to be found numerically so that each object Ω has a unique pattern in the coincidences. To demonstrate this, we return to our example with objects $\Omega_{a,b,c}$ from section 5.2.

The reduced states ρ_S from the objects $\Omega(\theta)$ after including the optimal M_I discussed in Fig. 5.2 are depicted together in the Poincaré sphere of Fig. 5.5(a). A plane that contains the three vectors \mathbf{m} and allows for the separation of the projected re-

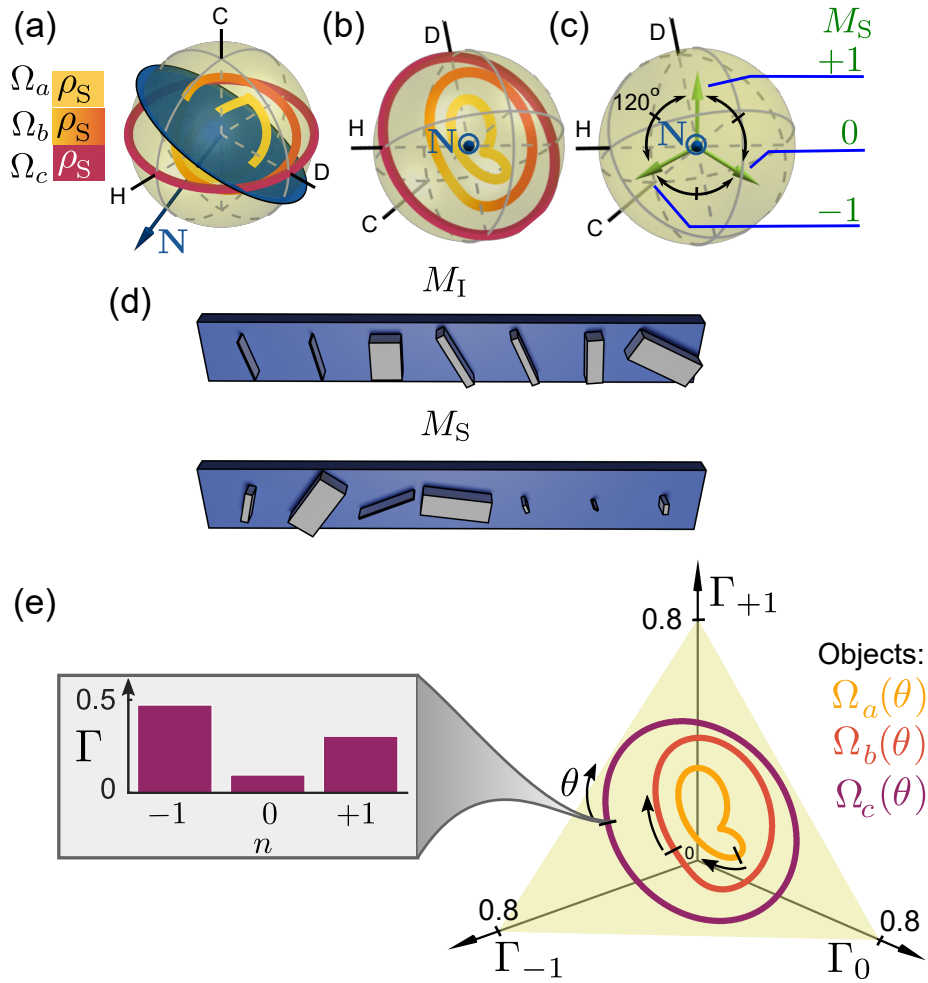


Figure 5.5. (a, b) Reduced state of the signal-photon ρ_S produced by a set of three objects $\Omega_{a,b,c}$ and an optimal metasurface M_I corresponding to Fig. 5.2(bottom row) from two different perspectives. The vector \mathbf{N} is normal to the blue plane where the optimal projection bases of the diffraction orders of the metasurface M_S are located; see (c). (d) Optimal meta-gratings in the idler M_I and signal M_S arms. (e) Coincidences at three diffraction orders Γ_{-1} , Γ_0 , Γ_{+1} , showing that the objects can be discerned from one another and their own rotation angle θ unambiguously identified ($\theta = 0$ is marked with ticks, the object rotation symmetry is π). The inset shows one of the coincidence patterns.

duced states is illustrated in blue along with its normal vector \mathbf{N} . The projections of all the reduced states ρ_S into this plane are shown in Fig. 5.5(b), which is the same as Fig. 5.5(a) but from the perspective of \mathbf{N} pointing to the reader, where it is clear that the projections are well separated. The reduced states can then be mapped into the space \mathcal{D} of the coincidences at the outputs using the three projection vectors of M_S depicted in Fig. 5.5(c). These three vectors \mathbf{m} sum up to zero to have high photon counts as described before. The direction of the optimal vector \mathbf{N} , and therefore the plane in which the vectors $\mathbf{m}_{1S,n}$ lie, has been found numerically using a simplex algorithm. As a next step, the optimal form of the meta-grating M_S based on the found vectors \mathbf{m} of the scheme is calculated numerically and displayed in Fig. 5.5(d), together with the meta-grating realizing the optimal M_I . The parameters found of the nano-resonators

Figure 5.5(d)						
Nano-resonator	M_I			M_S		
	$\theta[^\circ]$	ϕ_1	ϕ_2	$\theta[^\circ]$	ϕ_1	ϕ_2
1	104.22	1.73	0.06	-15.66	0.42	-1.91
2	100.75	1.71	-0.06	53.68	3.56	1.67
3	0.45	-1.18	1.66	22.60	3.45	-0.10
4	28.39	0.33	2.48	-7.55	3.95	1.35
5	24.42	-0.28	2.23	24.24	0.21	0.53
6	5.05	-0.62	1.91	-31.76	-0.27	0.09
7	62.79	1.07	2.69	3.33	0.29	-0.68

Table 5.1. Numerically found parameters of the nano-resonators: the orientation angle θ and the phase delays for polarizations along the two axes $\phi_{1,2}$.

of the two metasurfaces are displayed in Table 5.1. Here, seven nano-resonators were used during the optimization process, which facilitate the optimization process to realize the three optimal projections in the three central diffraction orders of M_S and the optimal projection in the central diffraction order of M_I .

Finally, for the set of objects investigated here, the result of the numerical optimization shows that at least three outputs are needed to successfully achieve discrimination. The coincidence patterns are presented in the space \mathcal{D} in Fig. 5.5(e), where a unique pattern corresponds to a specific object and rotation. The inset shows the complete coincidence pattern for the case of object Ω_c at rotation $\theta = 0$.

Lastly, we note that the polarization Jones matrices in principle can also be realized with a collection of bulk optical elements; however, at the expense of complex designs sensitive to alignment. Nanostructured dielectric metasurfaces can effectively act as partial polarizers in arbitrary elliptical bases with any required extinction ratio [87, 215]. However, if the optimal polarization basis to achieve discrimination is found to be the basis of a simple polarizing beamsplitter or a common linear polarizer, then it is unquestionably more convenient to use such simpler element in an experiment.

5.4. Entanglement versus classical correlations

5.4.1. Role of the degree of entanglement

After demonstrating that objects and their rotation angles can be discriminated using entangled states of light, next we show that the degree of entanglement between signal and idler photons of the source is relevant when distinguishing specific classes of objects. To this end, we explore the effect of reducing the entanglement until reaching only classical correlations of the type of Eq. (5.11) with $\kappa = 0$. We consider a different

set of polarization-sensitive objects that contains only generalized retarders

$$\Omega = \begin{bmatrix} 1 & 0 \\ 0 & \exp(i\phi) \end{bmatrix}, \quad (5.28)$$

each with its own phase difference ϕ between the horizontal and vertical polarization. Here, we do not seek to identify the rotation of each of them, but just discern them based on their phase ϕ . We choose this set of objects since it is a more challenging case for discrimination compared to the set of three objects discussed in the previous section.

Following the treatment presented before, we find that the optimal M_I necessary to discern these phase objects for any value of κ is a diagonal polarizer. Notice here that this element can be implemented simply using a conventional polarizer instead of a metasurface. The corresponding reduced states ρ_S of this set of phase objects are shown in Fig. 5.6(a) for different levels of entanglement κ . As can be seen, this chosen set of phase objects is quite peculiar because their reduced states have the same p_H Poincaré vector component [see Eq. (5.17a)], as p_H does not depend on the phase ϕ . Furthermore, Eqs. (5.17b) and (5.17c) show, that the lower the degree of entanglement, the smaller p_D and p_C become, as illustrated in Fig. 5.6(a) with a shrinking ellipsoid according to Eq. (5.18). In the case of only classical correlation between photons with $\kappa = 0$, we have $p_D = p_C = 0$, such that all reduced states are in the same position and the different objects cannot be discriminated.

It is noteworthy that if these phase objects given by Eq. (5.28) are rotated by an angle θ and an optimal M_I in the idler arm is chosen, then the p_H component of the product $T_I = M_I \Omega$ can depend on the phase ϕ [this can be easily derived from Eqs. (5.17a-5.17c)]. Therefore, such phase objects can be told apart if a source with photon pairs that are classically correlated, $\kappa = 0$, is used. Figure 5.6(b) illustrates an example with phase objects that are rotated 45° along with a horizontal polarizer as M_I . In this case, a horizontal polarizer is the optimal design of M_I following the first stage of the design described in section 5.2. In contrast to Fig. 5.6(b), Fig. 5.6(a) illustrates that if the phase objects given by Eq. (5.28) are not rotated, then they cannot be identified when using a source with only classical correlations with $\kappa = 0$. However, notice that although the introduced rotation allows for discrimination when $\kappa = 0$, the reduced states are much closer to each other than when using entangled photons $\kappa = 1$. Thus, in the scenario with only classical correlations, it is more complicated to achieve discrimination than when using entanglement since the smaller the separation between the reduced states, the harder it becomes to identify each from the rest. Furthermore, from the implementation perspective, notice that the compo-

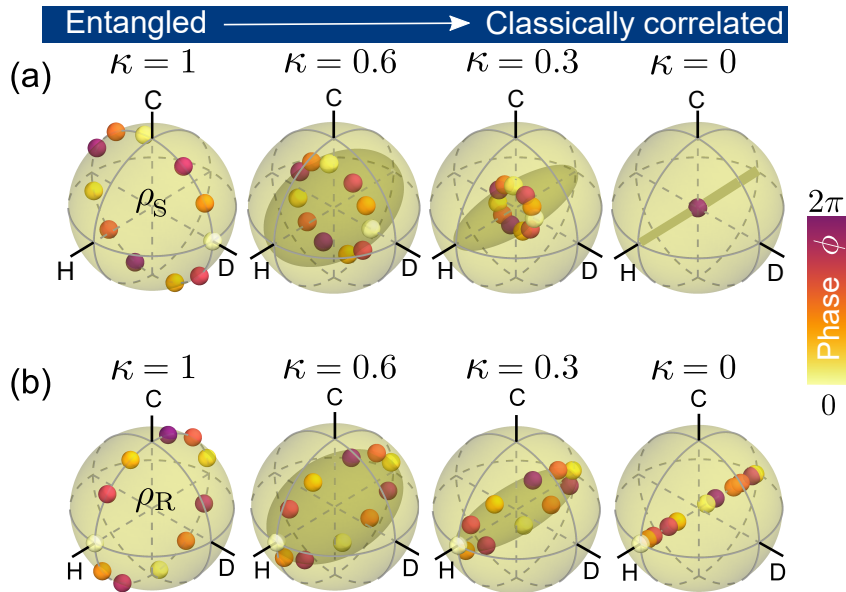


Figure 5.6. Reduced state of the signal photon after measuring the idler photon ρ_S at different levels of entanglement. Here, the idler photon interacts with a set of different fully transmissive phase objects (phase ϕ shown in the color scale), one at a time. (a) Not rotated $\theta = 0$ with optimal M_I that acts as a diagonal polarizer. (b) Rotated $\theta = 45^\circ$ with the corresponding optimal M_I which is a horizontal polarizer.

nents $p_D = p_C = 0$ when $\kappa = 0$; thus, the simplest element that can be used as M_S in the signal arm to discriminate the phase objects of the example in Fig. 5.6(b) is a conventional polarizing beamsplitter, which has two outputs, horizontal and vertical polarization.

In summary, objects in the idler arm T_I that lead to reduced states with the same p_H component can only be discriminated if the photon-pair source has a high level of entanglement. Our conclusion on the advantage of the entangled source over the considered classical source with $\kappa = 0$ generally agrees with the results of Ref. [133], where images of polarization-dependent patterns imprinted with a metasurface had higher visibility across different orientation angles for larger Bell parameter values.

Continuing with the discrimination procedure, a metasurface with four diffraction outputs has been demonstrated to facilitate the full characterization of a single-photon polarization state [87], thus allowing object discrimination based on the different signal photon states ρ_S . However, discrimination between particular sets of objects may be performed with a smaller set of outputs. For the set of three objects in Fig. 5.5, three outputs were necessary. On the other hand, we show now that two outputs of M_S can also be used to identify objects, and we demonstrate it by using the example of phase objects of Fig. 5.6(a). Figure 5.7 illustrates the resulting diffraction patterns in coincidences by using two different metasurfaces M_S which produce three and two diffraction orders, respectively. The right singular vectors of these metasurfaces are

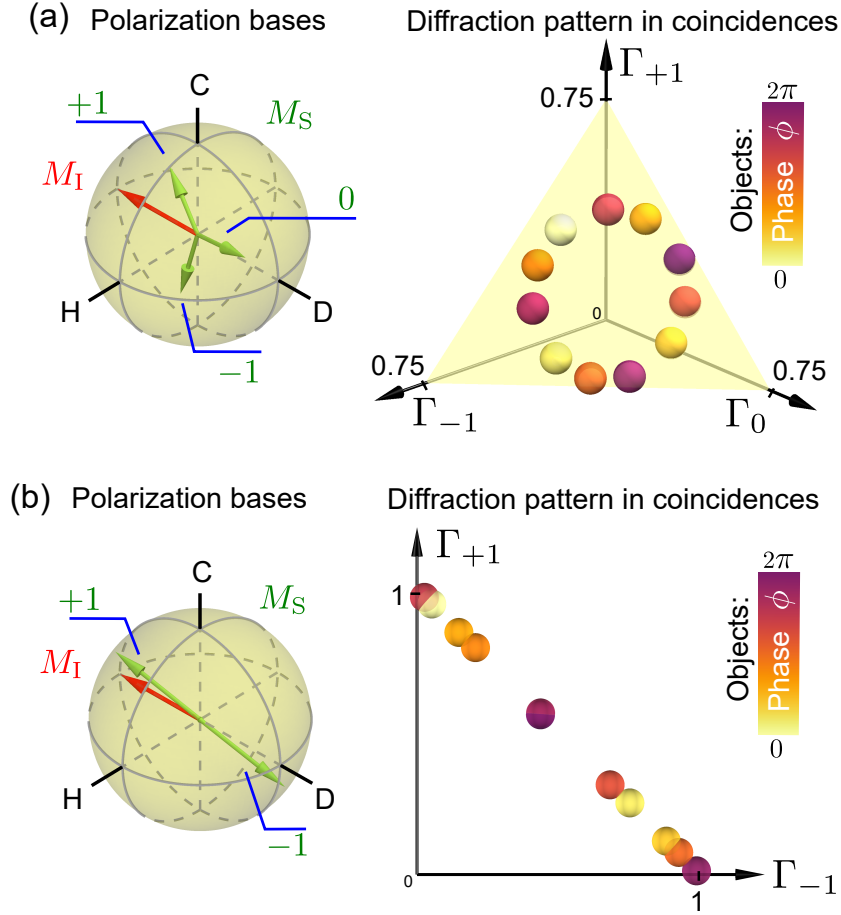


Figure 5.7. Polarization bases of a metasurface M_S with (a) three and (b) two outputs along with the resulting diffraction patterns in coincidences. The set consists of phase objects and a diagonal polarizer M_I used in Fig. 5.6(a).

shown in the left column of Fig. 5.7. Each metasurface is optimized separately using the criteria explained in the second stage of the design in section 5.3 and the parameters of their nano-resonators are summarized in Table 5.2.

Although in both cases of Fig. 5.7 a unique diffraction pattern corresponds to each object of the set, constraints of the photon measurements can define the minimum number of outputs required. For example, in Fig. 5.7(b), where the values of the coincidence counts are closer than in Fig. 5.7(a), the presence of noise in the measurements could impede discrimination, indicating that more outputs are needed.

5.4.2. Thermal source

We demonstrated in the last section that using a full entangled source $\rho(\kappa = 1)$ shows advantages in the identification of objects compared to the same scheme using a source with classical correlations of the type $\rho(\kappa = 0)$. At first, this seems to point out that there is a quantum advantage; however, there is another type of classical source that

Nano-resonator	Figure 5.7(a)			Figure 5.7(b)		
	M_S			M_S		
	$\theta[^\circ]$	ϕ_1	ϕ_2	$\theta[^\circ]$	ϕ_1	ϕ_2
1	87.36	1.59	3.84	7.37	2.96	2.21
2	-76.03	0.95	4.50	-31.41	3.49	1.69
3	136.21	0.07	-0.60	138.29	-1.94	0.90
4	-16.02	0.17	-1.24	-148.62	-0.34	-1.32
5	7.30	1.09	-1.39	-10.53	0.02	5.14
6	25.92	1.65	-2.56	-126.71	-1.95	-5.46
7	237.32	0.13	3.43	36.09	3.44	1.78

Table 5.2. Numerically found parameters of the nano-resonators for the metasurfaces M_S described in Fig. 5.7: the orientation angle θ and the phase delays for polarizations along the two axes $\phi_{1,2}$.

can lead to almost equal results obtained by the entangled source, namely a thermal source. In this section, we demonstrate this by obtaining closed-form expressions of, first, the coincidence counts of a QGP using entangled photons and second, the intensity correlations of a ghost polarimetry scheme with a thermal source.

We start by considering a maximally entangled two-photon state, similar to the one showcased in Eq. (5.11) for $\kappa = 1$; however, we do not restrict ourselves to the horizontal and vertical polarizations as before. In this manner, we present a more general expression of the coincidence rate, which will be compared later with the intensity correlations of the scheme with a thermal source. We represent this more general normalized two-photon state as $|\psi\rangle = (1/\sqrt{2})(|\mathbf{v}_{1I}\mathbf{v}_{1I}\rangle + |\mathbf{v}_{2I}\mathbf{v}_{2I}\rangle)$, where \mathbf{v} is a right singular vector of a Jones matrix V of size 2×2 . Note that \mathbf{v}_{1I} and \mathbf{v}_{2I} are orthogonal unitary vectors. Then, the two-photon coincidence counts can be found to be

$$\Gamma_n^{(\text{two-photon})} = \frac{1}{2} \sum_{q_I, q_S=1}^2 |\mathbf{v}_{q_I I} \cdot \mathbf{v}_{q_S S, n}|^2 \sigma_{q_I I}^2 \sigma_{q_S S, n}^2, \quad (5.29)$$

where σ are the singular values of the Jones matrices characterizing the objects located between the source to the detectors in the idler and signal arms, and we choose an order $\sigma_1 \geq \sigma_2$. Additionally, we note the following properties of unit vectors

$$|\mathbf{v}_{1I} \cdot \mathbf{v}_{2S, n}|^2 + |\mathbf{v}_{2I} \cdot \mathbf{v}_{2S, n}|^2 = 1, \quad (5.30a)$$

$$|\mathbf{v}_{1I} \cdot \mathbf{v}_{1S, n}|^2 + |\mathbf{v}_{2I} \cdot \mathbf{v}_{1S, n}|^2 = 1, \quad (5.30b)$$

$$|\mathbf{v}_{1I} \cdot \mathbf{v}_{1S, n}|^2 + |\mathbf{v}_{1I} \cdot \mathbf{v}_{2S, n}|^2 = 1. \quad (5.30c)$$

Therefore, we obtain the coincidence counting rate for QGP using entangled photons

$$\begin{aligned} \Gamma_n^{(\text{two-photon})} &= \frac{1}{4}(\sigma_{11}^2 + \sigma_{21}^2)(\sigma_{1S,n}^2 + \sigma_{2S,n}^2) \\ &\quad + \frac{1}{2}(\sigma_{11}^2 - \sigma_{21}^2)(\sigma_{1S,n}^2 - \sigma_{2S,n}^2) \left(|\mathbf{v}_{11} \cdot \mathbf{v}_{1S,n}|^2 - \frac{1}{2} \right). \end{aligned} \quad (5.31)$$

For comparison, we now consider a thermal source which has a classical polarization state, denoted by $|\Psi_{\text{th}}\rangle$, that randomly changes in time. The same source's polarization state can be found in both the idler and in the signal arm at any fixed time, for example, after interacting with a 50:50 beamsplitter. Then, the total intensity after interaction with an object in the idler arm described by a Jones matrix V is

$$I = \sigma_1^2 |\mathbf{v}_1 \cdot \Psi_{\text{th}}|^2 + \sigma_2^2 |\mathbf{v}_2 \cdot \Psi_{\text{th}}|^2. \quad (5.32)$$

Additionally, due to the orthogonality $\mathbf{v}_1 \cdot \mathbf{v}_2 = 0$ and $|\mathbf{v}_2 \cdot \Psi_{\text{th}}|^2 + |\mathbf{v}_1 \cdot \Psi_{\text{th}}|^2 = 1$, hence

$$I = (\sigma_1^2 - \sigma_2^2) |\mathbf{v}_1 \cdot \Psi_{\text{th}}|^2 + \sigma_2^2. \quad (5.33)$$

Considering that the input state, assuming that its norm is unity, can be represented as $\Psi_{\text{th}} = \cos(\frac{\theta}{2})\mathbf{v}_{11} + \sin(\frac{\theta}{2})e^{i\varphi}\mathbf{v}_{21}$, and using the property $|\mathbf{v}_{11} \cdot \mathbf{v}_{1S,n}|^2 + |\mathbf{v}_{21} \cdot \mathbf{v}_{1S,n}|^2 = 1$, we can write the intensities of the idler and signal arms as

$$I_1 = (\sigma_{11}^2 - \sigma_{21}^2) \cos^2(\theta/2) + \sigma_{21}^2, \quad (5.34a)$$

$$\begin{aligned} I_{S,n} &= (\sigma_{1S,n}^2 - \sigma_{2S,n}^2) \left[|\mathbf{v}_{1S,n} \cdot \mathbf{v}_{11}|^2 \cos(\theta) + \sin^2(\theta/2) \right. \\ &\quad \left. + \sin(\theta) \operatorname{Re}[e^{-i\varphi}(\mathbf{v}_{1S} \cdot \mathbf{v}_{11})(\mathbf{v}_{1S} \cdot \mathbf{v}_{21})^*] \right] + \sigma_{2S,n}^2. \end{aligned} \quad (5.34b)$$

Moreover, since the state Ψ_{th} can be represented with the density matrix $\rho_{\text{th}} = |\Psi_{\text{th}}\rangle \langle \Psi_{\text{th}}|$ whose Bloch vector is $\mathbf{a} = [\sin \theta \cos \phi, \sin \theta \sin \phi, \cos \theta]$, where $0 \leq \theta \leq \pi$ and $0 \leq \phi < 2\pi$ just like in a spherical coordinate system, the intensity correlation after averaging over these ranges of angles is

$$\begin{aligned} \langle I_1 I_{S,n} \rangle &= \frac{1}{2\pi} \int_0^{2\pi} d\varphi \frac{1}{\pi} \int_0^\pi d\theta I_1 I_{S,n} \\ &= \frac{1}{4}(\sigma_{11}^2 + \sigma_{21}^2)(\sigma_{1S,n}^2 + \sigma_{2S,n}^2) \\ &\quad + \frac{1}{4}(\sigma_{11}^2 - \sigma_{21}^2)(\sigma_{1S,n}^2 - \sigma_{2S,n}^2) \left(|\mathbf{v}_{11} \cdot \mathbf{v}_{1S,n}|^2 - \frac{1}{2} \right). \end{aligned} \quad (5.35)$$

Importantly, the first term constitutes the background contribution that is given by the product of the independent intensity fluctuations of each arm, $\langle I_1 \rangle = (\sigma_{11}^2 + \sigma_{21}^2)/2$

and $\langle I_{S,n} \rangle = (\sigma_{1S,n}^2 + \sigma_{2S,n}^2)/2$, while the second term shows the intensity correlation between the two arms.

The results obtained show that the correlations for a two-photon entangled source in Eq. (5.31) and a thermal source in Eq. (5.35) have the same form except for a factor of two difference in their corresponding second terms that represent correlations, which are above a background given by the first term. This means that the thermal source can be used to obtain the polarization information from the object in a manner similar to that of an entangled source. However, from the difference of the coefficients of the correlation terms, we conclude that the entangled case will show better contrast than the thermal source. That is, the ratio between the correlation term and the background term has a prefactor equal to two for the two-photon entangled source, whereas this ratio prefactor is equal to one for the thermal source. This feature is also seen in the imaging version of QGP, as mentioned in chapter 1. Furthermore, a two-photon source can allow precise measurements with much smaller photon fluxes, which is an important capability for various applications [216].

5.5. Abstract and publication

In this chapter, we put forward the working principles of a QGP scheme to detect polarization-sensitive objects. The scheme was presented using reduced density matrices which aid in the understanding and design of the scheme. Additionally, we demonstrated that QGP can be implemented with dielectric metasurfaces that realize complex polarization bases and enable parallel measurements instead of using multiple time-consuming reconfigurations of bulk elements to determine all components of a general Jones matrix [141]. Therefore, metasurfaces are ideal components to achieve speed and compactness in this scheme. Furthermore, we presented examples showcasing that QGP discrimination of fully or partially transparent polarization elements and their arbitrary orientation angles can be achieved by performing less than four coincidence measurements. Consequently, object discrimination does not require full quantum state tomography. In contrast, other works have performed discrimination of only non-birefringent objects at fixed orientations [217]. Moreover, we proved that entanglement is not a requirement to achieve ghost polarimetry, since a classical thermal source can be used to obtain similar results. Nevertheless, the quantum scheme with entangled photons has an unparalleled advantage over the classical scheme when illumination with single photons is needed to probe sensitive samples.

The analysis and results of this chapter were first presented at the CLEO conference 2020 [218] and ultimately published in *Physical Review Applied* [219].

6. Summary and outlook

In this thesis, three gaps in the literature on quantum imaging and polarimetry with two-color photon pairs were addressed: **1.** the fundamental resolution of quantum imaging with undetected photons (QIUP) and quantum ghost imaging (QGI) was derived, **2.** an original lensless imaging setup was proposed in the form of pinhole QGI, and **3.** a solid theoretical foundation was presented to describe quantum ghost polarimetry (QGP). Here, a summary of the results and outlook is presented.

Summary

Two-photon quantum state

A theoretical formalism of photon-pair generation beyond the paraxial regime was presented in chapter 2. This set the basis for the discussion of the imaging and polarimetry schemes in subsequent chapters. The presented formalism started with the definition of the electric field operator in section 2.1, which takes into account the photon polarization and transverse-momentum modes. This definition was used to model the two-photon state from spontaneous parametric down-conversion, see section 2.2. The obtained state of down-converted photon pairs was then simplified into two cases: First, a state that represents a source of photon pairs entangled in transverse momentum was derived, which was later used for quantum imaging in chapters 3 and 4. Second, a state of photon pairs that are only entangled in polarization was presented, which models the source of the QGP scheme discussed in chapter 5. Importantly, we thoroughly examined the non-paraxial case, where the formalism of the two-photon state needs to be treated in the angular domain to avoid the transverse-momentum singularities that hinder the mathematical treatment of the two-photon generation. Additionally, we showed that thick crystals lead to small ranges of angular generation of the down-converted photons, whereas ultra-thin crystals can be used to access the whole angular range since the longitudinal phase-matching is relaxed.

Fundamental resolution limit of two-color quantum imaging

As described in section 1.1.3, the effect of induced coherence without induced emission is at the heart of QIUP. The QIUP scheme consists of two nonlinear crystals that form a nonlinear interferometer, the idler photons are aligned to introduce indistinguishability of the sources, and the signal photons interfere at a beamsplitter. An object is located only in the path of the idler photons that remain undetected, whereas the signal photons are measured by a camera, revealing the transverse profile of the object's transmission. In section 3.1, the mathematical expression of the image was derived step by step for a QIUP scheme based on position correlations. The highlight of this derivation is that it is not restricted to the paraxial regime, as seen in other works, allowing us to derive a more general framework from which the fundamental transverse resolution of QIUP can be obtained.

In section 3.1.1, we used the Rayleigh criterion to investigate the minimum resolvable distance of QIUP. We proved analytically that in the paraxial regime, the resolution is given by $d_{\min}^{(\text{paraxial})} \propto (\lambda_S + \lambda_I)^{1/2} (1/L_A + 1/L_B)^{-1/2}$, which is valid for a QIUP scheme with crystals' thicknesses L larger than approximately $\max(\lambda_S, \lambda_I)$. This shows that the resolution can be improved by using thinner crystals. However, we also showed that crystals thinner than $\approx \max(\lambda_S, \lambda_I)$ allow one to achieve diffraction-limited resolution, which was numerically found to be $d_{\min}^{(\text{limit})} \approx \max(\lambda_S, \lambda_I)/2$, independent of L . Consequently, the longer wavelength of the photon pair defines the maximum achievable resolution. Moreover, we showed that the pump width does not have a noticeable effect on the resolution in a QIUP scheme with an ultra-thin crystal for common pump widths in experimental scenarios that are larger than the wavelengths of the down-converted photons. This feature is advantageous in achieving fundamental resolution under common experimental conditions where the pump has a limited transverse profile.

Lastly, we discussed the QGI scheme, which uses only one source of photon pairs, the idler photons that interact with the object are measured by a non-resolving bucket detector, and the signal photons that do not interact with the object are measured by a camera. In contrast to QIUP, the image of the object is found in the coincidence counts of signal and idler. In section 3.2, we used a similar analysis, as carried out for the QIUP scheme, to show that the fundamental limit of QGI based on position correlations is also limited by the longer wavelength of the photon pair. Furthermore, based on our analysis and results, we inferred that the fundamental resolution of other schemes, e.g., QIUP & QGI based on momentum correlations and their classical analogs, should be similarly limited by the longer wavelength.

Lensless quantum ghost imaging

As a preamble to discuss pinhole QGI, the basics of quantum ghost diffraction (QGD) are introduced in section 4.1. To obtain a ghost diffraction pattern of an object, we showed that a spatially resolving detector in the signal arm and a point detector in the interacting idler arm are needed. Lenses are not necessary to obtain the diffraction pattern in coincidences. Then in section 4.2, it was numerically proven that a QGI scheme without lenses in the signal and idler arms was possible by slightly modifying the QGD scheme, that is, taking a collimated pump with an optimal transverse size and changing the idler point detector into a large bucket detector. Thereafter, an analytical model was derived that indicated that such a QGI model was analogous to a classical pinhole camera. In this analogy, the ‘size of the pinhole’ is given by the photon-pair source; this means that it is defined by not only the pump width but also by the photon wavelengths, and the thickness of the nonlinear crystal. Additionally, like a classical pinhole camera, there is a relation between the pinhole size σ_0 and the other parameters that ensure the smallest point image of a slit, namely $\sigma_0^2 \propto z_s \lambda_s$, where z_s is the distance from the crystal to the signal detector and λ_s is the signal wavelength. Unlike the classical pinhole camera, we found that the magnification of the pinhole QGI also depends on the wavelengths of signal and idler, $-(z_s/z_o)(\lambda_s/\lambda_i)$ where z_o is the distance from the crystal to the object and λ_i is the idler wavelength.

Finally, a description of the minimum resolvable distance and the number of spatial modes was presented. Since throughout this chapter we focused only on the use of a thick crystal much larger than the signal and idler wavelengths, a paraxial description was sufficient. We showed that the resolution is improved by using a smaller pump width and also by locating the object closer to the crystal. Furthermore, the transverse resolution was found to be much larger than the signal and idler wavelengths and, therefore, far from the diffraction limit. Lastly, the number of spatial modes was shown to increase with the reduction of the crystal thickness; this is due to the increase in the range of transverse-momentum modes, as was discussed in section 2.2.

The pinhole QGI scheme is best suited for applications where lenses for the wavelengths of the down-converted photons are less available, for example, in the terahertz range, and a high transverse resolution is not required. For example, sensitive samples can be imaged by using terahertz idler photons, which are then simply measured by a single-photon bucket detector, while signal photons are measured by a camera with high efficiency in the visible range.

Metasurface-assisted quantum ghost polarimetry

In chapter 5, a comprehensive analysis of quantum ghost polarimetry (QGP) was presented. The chapter starts with the theoretical foundations of QGP in section 5.1. QGP uses a source of polarization-entangled photons, the idler photon interacts with a polarization-sensitive object, and then it is measured by a non-resolving detector, while the signal photon never interacts with the object, and it is measured through a polarization-resolving detection scheme. The analysis of the scheme was proposed using a two-stage approach. First, we discussed the reduced state of the signal photon after measuring the idler photon based on the principle of remote state preparation. Second, using this reduced state, we found the coincidence counting rate where the ghost polarization information of the object is found.

The geometrical representation of the reduced state in the Poincaré sphere became useful in portraying the state to later focus on the discrimination of polarization-sensitive objects; see section 5.2. The discrimination task focused on identifying three objects and their rotation angle. For the set of objects, we found that a complex partially polarizing transformation was needed to be realized and included in the idler arm. Given that in practice it is cumbersome to use a collection of bulk elements to realize such a transformation, we proposed using a metasurface to realize it. Section 5.3 starts by discussing the basic principles behind an all-dielectric metasurface, showcasing its versatility to realize tailored parallel photon-state transformations, which can be partially polarizing in an arbitrary elliptical basis. Moreover, each diffraction order of the metasurface can realize a different polarization basis; therefore, the polarization resolution in the signal arm can be implemented by just one metasurface. Next, we designed the appropriate meta-gratings for the metasurfaces that can be included in the signal and idler arm to achieve the discrimination of the mentioned three objects. Importantly, the optimal design of the metasurfaces will always depend on the chosen set of objects. For the discrimination problem, we showed that fewer than four coincidence measurements can be sufficient, since a full tomographic reconstruction of the state is unnecessary.

At the end of the chapter in section 5.4, we discussed the role of entanglement in QGP. The outcome of this analysis is that there are classical sources of correlated light that can be used to acquire almost the same results as when using an entangled source of photon pairs, as was proved with a thermal source. This has also been observed in the context of ghost imaging [97, 98, 144, 220]. The difference we found is that entangled photons allow one to have a smaller background in the coincidence measurements than when using classical light.

Outlook

In this thesis, we have considered only coherent pump beams to create the down-converted photons. It is of interest to study the effect of the level of transverse spatial coherence of the pump on the imaging formation in QIUP & QGI and also the effect on the resolution. This is motivated by the results of Refs. [221, 222] showing that, depending on the type of partially coherent pump beam, the level of entanglement of the down-converted photons can be reduced but also boosted with a highly spatially incoherent pump.

With regard to QGP, the results presented can certainly stimulate the development of efficient and integrated optical schemes for the characterization of polarization-sensitive objects over a broad spectral range. Specifically, QGP can benefit applications that demand accurate object discrimination, including biological samples with distinct birefringent and chiral features [223–225]. Furthermore, it has been shown that optimized metasurfaces can enable discrimination of multiple objects within a set. Thus, our approach paves the way for further research that focuses not only on the ultimate limit of the number of objects that can be discriminated but also on the possibility of facilitating the characterization of objects with spatially dependent polarization, e.g., by exploiting the momentum correlation and/or orbital angular momentum of a photon pair [226]. Furthermore, there is the potential to dynamically adapt the ghost polarimetry scheme for different target objects using tunable metasurfaces [227].

The strategy to devise a novel lenless quantum imaging scheme in chapter 4, that is, by optimizing a parameter of the scheme, could be extrapolated to discover new quantum imaging protocols beyond QIUP & QGI. A potential way to achieve this follows the lines of the work of Krenn et al. [228] that uses machine learning for quantum technologies. A quantum imaging scheme can be seen as a combination of defined basic building blocks, e.g., photon-pair sources, lenses, mirrors, free-space propagation, etc., each characterized by a finite number of parameters. Consequently, a machine learning algorithm that uses reinforcement learning can be given the task of searching for novel quantum imaging schemes by optimizing the large number of parameters that arise from the combination of these basic elements.

Finally, the results presented in this thesis have not yet been experimentally realized. However, all of these theoretical findings can be experimentally implemented with current state-of-the-art technology. While this thesis is written, the effect of the pump width on the resolution of QIUP based on position correlations is being experimentally tested [229] and a source with entangled photons in polarization and non-degenerate wavelengths for QGP is being built in our laboratory.

A. References

- [1] A. Einstein, B. Podolsky, and N. Rosen, »Can quantum-mechanical description of physical reality be considered complete?«, *Phys. Rev.* **47**, 777–780 (1935).
- [2] E. Schrödinger,
»Discussion of probability relations between separated systems«, *Mathematical Proceedings of the Cambridge Philosophical Society* **31**, 555–563 (1935).
- [3] A. Aspect, P. Grangier, and G. Roger,
»Experimental realization of Einstein-Podolsky-Rosen-Bohm Gedankenexperiment - a new violation of Bell inequalities«, *Phys. Rev. Lett.* **49**, 91–94 (1982).
- [4] J. F. Clauser, M. A. Horne, A. Shimony, and R. A. Holt,
»Proposed experiment to test local hidden-variable theories«, *Phys. Rev. Lett.* **23**, 880–884 (1969).
- [5] G. Weihs, T. Jennewein, C. Simon, H. Weinfurter, and A. Zeilinger,
»Violation of bell’s inequality under strict einstein locality conditions«, *Phys. Rev. Lett.* **81**, 5039–5043 (1998).
- [6] D. C. Burnham and D. L. Weinberg, »Observation of simultaneity in parametric production of optical photon pairs«, *Phys. Rev. Lett.* **25**, 84–87 (1970).
- [7] C. K. Hong and L. Mandel,
»Theory of parametric frequency down conversion of light«, *Phys. Rev. A* **31**, 2409–2418 (1985).
- [8] A. Kuzmich, W. P. Bowen, A. D. Boozer, A. Boca, C. W. Chou, L.-M. Duan, and H. J. Kimble, »Generation of nonclassical photon pairs for scalable quantum communication with atomic ensembles«, *Nature* **423**, 731–734 (2003).
- [9] M. Afsharnia, Z. Lyu, T. Pertsch, M. A. Schmidt, S. Saravi, and F. Setzpfandt,
»Spectral tailoring of photon pairs from microstructured suspended-core optical fibers with liquid-filled nanochannels«, *Opt. Express* **30**, 29680–29693.
- [10] M. O. Scully and K. Drühl,
»Quantum eraser: a proposed photon correlation experiment concerning observation and "delayed choice" in quantum mechanics«, *Phys. Rev. A* **25**, 2208–2213 (1982).
- [11] P. G. Kwiat, A. M. Steinberg, and R. Y. Chiao, »Observation of a “quantum eraser”’: a revival of coherence in a two-photon interference experiment«, *Phys. Rev. A* **45**, 7729–7739 (1992).

- [12] Y.-H. Kim, R. Yu, S. P. Kulik, Y. Shih, and M. O. Scully, »Delayed “choice” quantum eraser«, *Phys. Rev. Lett.* **84**, 1–5 (2000).
- [13] S. P. Walborn, M. O. Terra Cunha, S. Pádua, and C. H. Monken, »Double-slit quantum eraser«, *Phys. Rev. A* **65**, 033818 (2002).
- [14] C. H. Bennett, G. Brassard, C. Crépeau, R. Jozsa, A. Peres, and W. K. Wootters, »Teleporting an unknown quantum state via dual classical and einstein-podolsky-rosen channels«, *Phys. Rev. Lett.* **70**, 1895–1899 (1993).
- [15] D. Boschi, S. Branca, F. De Martini, L. Hardy, and S. Popescu, »Experimental realization of teleporting an unknown pure quantum state via dual classical and einstein-podolsky-rosen channels«, *Phys. Rev. Lett.* **80**, 1121–1125 (1998).
- [16] D. Bouwmeester, J.-W. Pan, K. Mattle, M. Eibl, H. Weinfurter, and A. Zeilinger, »Experimental quantum teleportation«, *Nature* **390**, 575–579 (1997).
- [17] M. Żukowski, A. Zeilinger, M. A. Horne, and A. K. Ekert, »“event-ready-detectors” bell experiment via entanglement swapping«, *Phys. Rev. Lett.* **71**, 4287–4290 (1993).
- [18] J.-W. Pan, D. Bouwmeester, H. Weinfurter, and A. Zeilinger, »Experimental entanglement swapping: entangling photons that never interacted«, *Phys. Rev. Lett.* **80**, 3891–3894 (1998).
- [19] T. Jennewein, G. Weihs, J.-W. Pan, and A. Zeilinger, »Experimental nonlocality proof of quantum teleportation and entanglement swapping«, *Phys. Rev. Lett.* **88**, 017903 (2001).
- [20] H. de Riedmatten, I. Marcikic, J. A. W. van Houwelingen, W. Tittel, H. Zbinden, and N. Gisin, »Long-distance entanglement swapping with photons from separated sources«, *Phys. Rev. A* **71**, 050302 (2005).
- [21] T. Yang, Q. Zhang, T.-Y. Chen, S. Lu, J. Yin, J.-W. Pan, Z.-Y. Wei, J.-R. Tian, and J. Zhang, »Experimental synchronization of independent entangled photon sources«, *Phys. Rev. Lett.* **96**, 110501 (2006).
- [22] M. Halder, A. Beveratos, N. Gisin, V. Scarani, C. Simon, and H. Zbinden, »Entangling independent photons by time measurement«, *Nature Physics* **3**, 692–695 (2007).
- [23] S. Slussarenko and G. J. Pryde, »Photonic quantum information processing: a concise review«, *Appl. Phys. Rev.* **6**, 041303 (2019).
- [24] N. Gisin and R. Thew, »Quantum communication«, *Nat. Photon.* **1**, 165–171 (2007).
- [25] V. Giovannetti, S. Lloyd, and L. Maccone, »Advances in quantum metrology«, *Nat. Photon.* **5**, 222–229 (2011).

- [26] L. Pezze, A. Smerzi, M. K. Oberthaler, R. Schmied, and P. Treutlein, »Quantum metrology with nonclassical states of atomic ensembles«, *Rev. Mod. Phys.* **90**, 035005 (2018).
- [27] M. Gilaberte Basset, F. Setzpfandt, F. Steinlechner, E. Beckert, T. Pertsch, and M. Gräfe, »Perspectives for applications of quantum imaging«, *Laser & Photonics Reviews* **13**, 1900097 (2019).
- [28] M. D'Angelo and Y. H. Shih, »Quantum imaging«, *Laser Physics Letters* **2**, 567 (2005).
- [29] J. H. Shapiro and R. W. Boyd, »The physics of ghost imaging«, *Quantum Information Processing* **11**, 949–993 (2012).
- [30] M. J. Padgett and R. W. Boyd, »An introduction to ghost imaging: quantum and classical«, *Philosophical Transactions of the Royal Society A: Mathematical, Physical and Engineering Sciences* **375**, 20160233 (2017).
- [31] M. Genovese, »Real applications of quantum imaging«, *Journal of Optics* **18**, 073002 (2016).
- [32] S. Mukamel et al., »Roadmap on quantum light spectroscopy«, *Journal of Physics B: Atomic, Molecular and Optical Physics* **53**, 072002 (2020).
- [33] M. D'Angelo, A. Garuccio, and V. Tamma, »Toward real maximally path-entangled N -photon-state sources«, *Phys. Rev. A* **77**, 063826 (2008).
- [34] T. Ono, R. Okamoto, and S. Takeuchi, »An entanglement-enhanced microscope«, *Nature Communications* **4**, 2426 (2013).
- [35] N. Samantaray, I. Ruo-Berchera, A. Meda, and M. Genovese, »Realization of the first sub-shot-noise wide field microscope«, *Light: Science & Applications* **6**, e17005–e17005 (2017).
- [36] V. F. Gili, C. Piccinini, M. Safari Arabi, P. Kumar, V. Besaga, E. Brambila, M. Gräfe, T. Pertsch, and F. Setzpfandt, »Experimental realization of scanning quantum microscopy«, *Applied Physics Letters* **121**, 104002 (2022).
- [37] M. Malik, O. S. Magaña-Loaiza, and R. W. Boyd, »Quantum-secured imaging«, *Applied Physics Letters* **101**, 241103 (2012).
- [38] C. Abbattista et al., »Towards quantum 3d imaging devices«, *Applied Sciences* **11**, 10.3390/app11146414 (2021).
- [39] F. V. Pepe, F. Di Lena, A. Garuccio, G. Scarcelli, and M. D'Angelo, »Correlation plenoptic imaging with entangled photons«, *Technologies* **4**, 10.3390/technologies4020017 (2016).

- [40] F. V. Pepe, A. Scagliola, A. Garuccio, and M. D'Angelo, »Quantum imaging for space objects«, in *Igarss 2020 - 2020 IEEE International Geoscience and Remote Sensing Symposium (2020)*, pp. 3700–3702.
- [41] C. A. Casacio, L. S. Madsen, A. Terrasson, M. Waleed, K. Barnscheidt, B. Hage, M. A. Taylor, and W. P. Bowen, »Quantum-enhanced nonlinear microscopy«, *Nature* **594**, 201–206 (2021).
- [42] C. W. S. Chang, A. M. Vadiraj, J. Bourassa, B. Balaji, and C. M. Wilson, »Quantum-enhanced noise radar«, *Applied Physics Letters* **114**, 112601 (2019).
- [43] L. Cohen, E. S. Matekole, Y. Sher, D. Istrati, H. S. Eisenberg, and J. P. Dowling, »Thresholded quantum lidar: exploiting photon-number-resolving detection«, *Phys. Rev. Lett.* **123**, 203601 (2019).
- [44] S. Oppel, T. Büttner, P. Kok, and J. von Zanthier, »Superresolving multiphoton interferences with independent light sources«, *Phys. Rev. Lett.* **109**, 233603 (2012).
- [45] A. Classen, F. Waldmann, S. Giebel, R. Schneider, D. Bhatti, T. Mehringer, and J. von Zanthier, »Superresolving imaging of arbitrary one-dimensional arrays of thermal light sources using multiphoton interference«, *Phys. Rev. Lett.* **117**, 253601 (2016).
- [46] C. Thiel, T. Bastin, J. von Zanthier, and G. S. Agarwal, »Sub-rayleigh quantum imaging using single-photon sources«, *Phys. Rev. A* **80**, 013820 (2009).
- [47] C. Thiel, T. Bastin, J. von Zanthier, and G. S. Agarwal, »Sub-rayleigh quantum imaging using single-photon sources«, *Phys. Rev. A* **80**, 013820 (2009).
- [48] C. Thiel, T. Bastin, J. Martin, E. Solano, J. von Zanthier, and G. S. Agarwal, »Quantum imaging with incoherent photons«, *Phys. Rev. Lett.* **99**, 133603 (2007).
- [49] R. Schneider et al., »Quantum imaging with incoherently scattered light from a free-electron laser«, *Nature Physics* **14**, 126–129 (2018).
- [50] A. N. Boto, P. Kok, D. S. Abrams, S. L. Braunstein, C. P. Williams, and J. P. Dowling, »Quantum interferometric optical lithography: exploiting entanglement to beat the diffraction limit«, *Phys. Rev. Lett.* **85**, 2733–2736 (2000).
- [51] U. W. Rathe and M. O. Scully, »Theoretical basis for a new subnatural spectroscopy via correlation interferometry«, *Letters in Mathematical Physics* **34**, 297–307 (1995).
- [52] M. D'Angelo, M. V. Chekhova, and Y. Shih, »Two-photon diffraction and quantum lithography«, *Phys. Rev. Lett.* **87**, 013602 (2001).

- [53] R. W. Boyd and J. P. Dowling, »Quantum lithography: status of the field«, *Quantum Information Processing* **11**, 891–901 (2012).
- [54] D. A. Kalashnikov, A. V. Paterova, S. P. Kulik, and L. A. Krivitsky, »Infrared spectroscopy with visible light«, *Nature Photonics* **10**, 98–101 (2016).
- [55] C. Lindner, J. Kunz, S. J. Herr, S. Wolf, J. Kießling, and F. Kühnemann, »Nonlinear interferometer for fourier-transform mid-infrared gas spectroscopy using near-infrared detection«, *Opt. Express* **29**, 4035–4047 (2021).
- [56] M. Kutas, B. Haase, P. Bickert, F. Riexinger, D. Molter, and G. von Freymann, »Terahertz quantum sensing«, *Science Advances* **6**, 10.1126/sciadv.aaz8065 (2020).
- [57] M. Kutas, B. Haase, J. Klier, D. Molter, and G. von Freymann, »Quantum-inspired terahertz spectroscopy with visible photons«, *Optica* **8**, 438–441 (2021).
- [58] A. Vanselow, P. Kaufmann, I. Zorin, B. Heise, H. M. Chrzanowski, and S. Ramelow, »Frequency-domain optical coherence tomography with undetected mid-infrared photons«, *Optica* **7**, 1729–1736 (2020).
- [59] P. Kumar, S. Saravi, T. Pertsch, and F. Setzpfandt, »Integrated induced-coherence spectroscopy in a single nonlinear waveguide«, *Phys. Rev. A* **101**, 053860 (2020).
- [60] R. Whittaker, C. Erven, A. Neville, M. Berry, J. L. O’Brien, H. Cable, and J. C. F. Matthews, »Absorption spectroscopy at the ultimate quantum limit from single-photon states«, *New Journal of Physics* **19**, 023013 (2017).
- [61] P.-A. Moreau, J. Sabines-Chesterking, R. Whittaker, S. K. Joshi, P. M. Birchall, A. McMillan, J. G. Rarity, and J. C. F. Matthews, »Demonstrating an absolute quantum advantage in direct absorption measurement«, *Scientific Reports* **7**, 6256 (2017).
- [62] P. G. Kwiat, W. A. Vareka, C. K. Hong, H. Nathel, and R. Y. Chiao, »Correlated two-photon interference in a dual-beam michelson interferometer«, *Phys. Rev. A* **41**, 2910–2913 (1990).
- [63] P. G. Kwiat and R. Y. Chiao, »Observation of a nonclassical berry’s phase for the photon«, *Phys. Rev. Lett.* **66**, 588–591 (1991).
- [64] A. M. Steinberg, P. G. Kwiat, and R. Y. Chiao, »Dispersion cancellation in a measurement of the single-photon propagation velocity in glass«, *Phys. Rev. Lett.* **68**, 2421–2424 (1992).
- [65] P. G. Kwiat, A. M. Steinberg, and R. Y. Chiao, »High-visibility interference in a bell-inequality experiment for energy and time«, *Phys. Rev. A* **47**, R2472–R2475 (1993).
- [66] A. O. C. Davis, V. Thiel, and B. J. Smith, »Measuring the quantum state of a photon pair entangled in frequency and time«, *Optica* **7**, 1317–1322 (2020).

- [67] P. G. Kwiat, K. Mattle, H. Weinfurter, A. Zeilinger, A. V. Sergienko, and Y. Shih, »New high-intensity source of polarization-entangled photon pairs«, *Phys. Rev. Lett.* **75**, 4337–4341 (1995).
- [68] P. G. Kwiat, E. Waks, A. G. White, I. Appelbaum, and P. H. Eberhard, »Ultrabright source of polarization-entangled photons«, *Phys. Rev. A* **60**, R773–R776 (1999).
- [69] Y.-H. Kim, S. P. Kulik, and Y. Shih, »High-intensity pulsed source of space-time and polarization double-entangled photon pairs«, *Phys. Rev. A* **62**, 011802 (2000).
- [70] T. Yamamoto, M. Koashi, Ş. K. Özdemir, and N. Imoto, »Experimental extraction of an entangled photon pair from two identically decohered pairs«, *Nature* **421**, 343–346 (2003).
- [71] X.-L. Wang et al., »Experimental ten-photon entanglement«, *Phys. Rev. Lett.* **117**, 210502 (2016).
- [72] H.-S. Zhong et al., »12-photon entanglement and scalable scattershot boson sampling with optimal entangled-photon pairs from parametric down-conversion«, *Phys. Rev. Lett.* **121**, 250505 (2018).
- [73] M. Pelton, P. Marsden, D. Ljunggren, M. Tengner, A. Karlsson, A. Fragemann, C. Canalias, and F. Laurell, »Bright, single-spatial-mode source of frequency non-degenerate, polarization-entangled photon pairs using periodically poled ktp«, *Opt. Express* **12**, 3573–3580 (2004).
- [74] M. Fiorentino, S. M. Spillane, R. G. Beausoleil, T. D. Roberts, P. Battle, and M. W. Munro, »Spontaneous parametric down-conversion in periodically poled ktp waveguides and bulk crystals«, *Opt. Express* **15**, 7479–7488 (2007).
- [75] F. Laudenbach, S. Kalista, M. Hentschel, P. Walther, and H. Hübel, »A novel single-crystal & single-pass source for polarisation- and colour-entangled photon pairs«, *Scientific Reports* **7**, 7235 (2017).
- [76] A. Vanselow, P. Kaufmann, H. M. Chrzanowski, and S. Ramelow, »Ultra-broadband spdc for spectrally far separated photon pairs«, *Opt. Lett.* **44**, 4638–4641 (2019).
- [77] S. Slussarenko, M. M. Weston, L. K. Shalm, V. B. Verma, S.-W. Nam, S. Kocsis, T. C. Ralph, and G. J. Pryde, »Quantum channel correction outperforming direct transmission«, *Nature Communications* **13**, 1832 (2022).
- [78] S. Saravi, T. Pertsch, and F. Setzpfandt, »Generation of counterpropagating path-entangled photon pairs in a single periodic waveguide«, *Phys. Rev. Lett.* **118**, 183603 (2017).

- [79] A. S. Solntsev, T. Liu, A. Boes, T. G. Nguyen, C. W. Wu, F. Setzpfandt, A. Mitchell, D. N. Neshev, and A. A. Sukhorukov, »Towards on-chip photon-pair bell tests: spatial pump filtering in a linbo3 adiabatic coupler«, *Applied Physics Letters* **111**, 261108 (2017).
- [80] P. R. Sharapova, K. H. Luo, H. Herrmann, M. Reichelt, T. Meier, and C. Silberhorn, »Toolbox for the design of linbo₃-based passive and active integrated quantum circuits«, *New Journal of Physics* **19**, 123009 (2017).
- [81] A. S. Solntsev, P. Kumar, T. Pertsch, A. A. Sukhorukov, and F. Setzpfandt, »Linbo3 waveguides for integrated spdc spectroscopy«, *APL Photonics* **3**, 021301 (2018).
- [83] C. Okoth, A. Cavanna, T. Santiago-Cruz, and M. V. Chekhova, »Microscale generation of entangled photons without momentum conservation«, *Phys. Rev. Lett.* **123**, 263602 (2019).
- [84] T. Santiago-Cruz, V. Sultanov, H. Zhang, L. A. Krivitsky, and M. V. Chekhova, »Entangled photons from subwavelength nonlinear films«, *Opt. Lett.* **46**, 653–656 (2021).
- [85] A. S. Solntsev et al., »Generation of nonclassical biphoton states through cascaded quantum walks on a nonlinear chip«, *Phys. Rev. X* **4**, 031007 (2014).
- [86] T. Santiago-Cruz, A. Fedotova, V. Sultanov, M. A. Weissflog, D. Arslan, M. Younesi, T. Pertsch, I. Staude, F. Setzpfandt, and M. Chekhova, »Photon pairs from resonant metasurfaces«, *Nano Letters* **21**, PMID: 33971095, 4423–4429 (2021).
- [87] K. Wang, J. G. Titchener, S. S. Kruk, L. Xu, H. P. Chung, M. Parry, I. I. Kravchenko, Y. H. Chen, A. S. Solntsev, Y. S. Kivshar, D. N. Neshev, and A. A. Sukhorukov, »Quantum metasurface for multiphoton interference and state reconstruction«, *Science* **361**, 1104–1107 (2018).
- [88] T. Santiago-Cruz, S. D. Gennaro, O. Mitrofanov, S. Addamane, J. Reno, I. Brener, and M. V. Chekhova, »Resonant metasurfaces for generating complex quantum states«, *Science* **377**, 991–995 (2022).
- [89] D. V. Strekalov, A. V. Sergienko, D. N. Klyshko, and Y. H. Shih, »Observation of two-photon “ghost” interference and diffraction«, *Phys. Rev. Lett.* **74**, 3600–3603 (1995).
- [90] T. B. Pittman, Y. H. Shih, D. V. Strekalov, and A. V. Sergienko, »Optical imaging by means of two-photon quantum entanglement«, *Phys. Rev. A* **52**, R3429–R3432 (1995).
- [91] D. N. Klyshko, »A simple method of preparing pure states of an optical field, of implementing the einstein–podolsky–rosen experiment, and of demonstrating the complementarity principle«, *Soviet Physics Uspekhi* **31**, 74–85 (1988).

- [92] R. S. Bennink, S. J. Bentley, R. W. Boyd, and J. C. Howell, »Quantum and classical coincidence imaging«, *Phys. Rev. Lett.* **92**, 033601 (2004).
- [93] F. Ferri, D. Magatti, A. Gatti, M. Bache, E. Brambilla, and L. A. Lugiato, »High-resolution ghost image and ghost diffraction experiments with thermal light«, *Phys. Rev. Lett.* **94**, 183602 (2005).
- [94] M. D'Angelo, Y.-H. Kim, S. P. Kulik, and Y. Shih, »Identifying entanglement using quantum ghost interference and imaging«, *Phys. Rev. Lett.* **92**, 233601 (2004).
- [95] A. F. Abouraddy, B. E. A. Saleh, A. V. Sergienko, and M. C. Teich, »Role of entanglement in two-photon imaging«, *Phys. Rev. Lett.* **87**, 123602 (2001).
- [96] A. Gatti, E. Brambilla, and L. A. Lugiato, »Entangled imaging and wave-particle duality: from the microscopic to the macroscopic realm«, *Phys. Rev. Lett.* **90**, 133603 (2003).
- [97] R. S. Bennink, S. J. Bentley, and R. W. Boyd, »"two-photon" coincidence imaging with a classical source«, *Phys. Rev. Lett.* **89**, 113601–4 (2002).
- [98] A. Gatti, E. Brambilla, M. Bache, and L. A. Lugiato, »Ghost imaging with thermal light: comparing entanglement and classical correlation«, *Phys. Rev. Lett.* **93**, 093602 (2004).
- [99] J. Cheng and S. Han, »Incoherent coincidence imaging and its applicability in x-ray diffraction«, *Phys. Rev. Lett.* **92**, 093903 (2004).
- [100] J. H. Shapiro, »Computational ghost imaging«, *Phys. Rev. A* **78**, 061802 (2008).
- [101] B. Sun, M. P. Edgar, R. Bowman, L. E. Vittert, S. Welsh, A. Bowman, and M. J. Padgett, »3d computational imaging with single-pixel detectors«, *Science* **340**, 844–847 (2013).
- [102] N. Radwell, K. J. Mitchell, G. M. Gibson, M. P. Edgar, R. Bowman, and M. J. Padgett, »Single-pixel infrared and visible microscope«, *Optica* **1**, 285–289 (2014).
- [103] M. Braasch, V. F. Gili, T. Pertsch, and F. Setzpfandt, »Classical ghost imaging: a comparative study of algorithmic performances for image reconstruction in prospect of plenoptic imaging«, *IEEE Photonics Journal* **13**, 1–14 (2021).
- [104] Y. Y. Kim et al., »Ghost imaging at an xuv free-electron laser«, *Phys. Rev. A* **101**, 013820 (2020).
- [105] M. N. O'Sullivan, K. W. C. Chan, and R. W. Boyd, »Comparison of the signal-to-noise characteristics of quantum versus thermal ghost imaging«, *Phys. Rev. A* **82**, 053803 (2010).

- [106] G. Brida, M. Genovese, and I. Ruo Berchera, »Experimental realization of sub-shot-noise quantum imaging«, *Nature Photonics* **4**, 227–230 (2010).
- [107] P. A. Morris, R. S. Aspden, J. E. C. Bell, R. W. Boyd, and M. J. Padgett, »Imaging with a small number of photons«, *Nat. Commun.* **6**, 5913–6 (2015).
- [108] K. W. C. Chan, M. N. O’Sullivan, and R. W. Boyd, »Two-color ghost imaging«, *Phys. Rev. A* **79**, 033808 (2009).
- [109] S. Karmakar and Y. H. Shih, »Two-color ghost imaging with enhanced angular resolving power«, *Phys. Rev. A* **81**, 033845 (2010).
- [110] R. S. Aspden, N. R. Gemmell, P. A. Morris, D. S. Tasca, L. Mertens, M. G. Tanner, R. A. Kirkwood, A. Ruggeri, A. Tosi, R. W. Boyd, G. S. Buller, R. H. Hadfield, and M. J. Padgett, »Photon-sparse microscopy: visible light imaging using infrared illumination«, *Optica* **2**, 1049–1052 (2015).
- [111] R. S. Aspden, D. S. Tasca, R. W. Boyd, and M. J. Padgett, »EPR-based ghost imaging using a single-photon-sensitive camera«, *New Journal of Physics* **15**, 073032 (2013).
- [112] P.-A. Moreau, F. Devaux, and E. Lantz, »Einstein-podolsky-rosen paradox in twin images«, *Phys. Rev. Lett.* **113**, 160401 (2014).
- [114] B. Ndagano, H. Defienne, D. Branford, Y. D. Shah, A. Lyons, N. Westerberg, E. M. Gauger, and D. Faccio, »Quantum microscopy based on hong–ou–mandel interference«, *Nature Photonics* **16**, 384–389 (2022).
- [115] X. Gao, Y. Zhang, A. D’Errico, K. Heshami, and E. Karimi, »High-speed imaging of spatiotemporal correlations in hong-ou-mandel interference«, *Opt. Express* **30**, 19456–19464 (2022).
- [116] C. Pitsch, D. Walter, S. Grosse, W. Brockherde, H. Bürsing, and M. Eichhorn, »Quantum ghost imaging using asynchronous detection«, *Appl. Opt.* **60**, F66–F70 (2021).
- [117] M. Zarghami, L. Gasparini, L. Parmesan, M. Moreno-Garcia, A. Stefanov, B. Bessire, M. Unternährer, and M. Perenzoni, »A 32×32 -pixel cmos imager for quantum optics with per-spaxial tdc, 19.48% fill-factor in a $44.64\mu\text{m}$ pitch reaching 1 mhz observation rate«, *IEEE Journal of Solid-State Circuits* **55**, 2819–2830 (2020).
- [118] A. Nomerotski, »Imaging and time stamping of photons with nanosecond resolution in timepix based optical cameras«, *Nuclear Instruments and Methods in Physics Research Section A: Accelerators, Spectrometers, Detectors and Associated Equipment* **937**, 26–30 (2019).
- [119] V. B. Verma et al., »Single-photon detection in the mid-infrared up to $10\mu\text{m}$ wavelength using tungsten silicide superconducting nanowire detectors«, *APL Photonics* **6**, 056101 (2021).

- [120] M. Kutas, B. E. Haase, F. Riexinger, J. Hennig, P. Bickert, T. Pfeiffer, M. Bortz, D. Molter, and G. von Freymann, »Quantum sensing with extreme light«, *Advanced Quantum Technologies* **5**, 2100164 (2022).
- [121] A. E. Yachmenev, R. A. Khabibullin, and D. S. Ponomarev, »Recent advances in thz detectors based on semiconductor structures with quantum confinement: a review«, *Journal of Physics D: Applied Physics* **55**, 193001 (2022).
- [122] D. Molter, M. Kolano, and G. von Freymann, »Terahertz cross-correlation spectroscopy driven by incoherent light from a superluminescent diode«, *Opt. Express* **27**, 12659–12665 (2019).
- [123] T. Pfeiffer, S. Weber, J. Klier, S. Bachtler, D. Molter, J. Jonuscheit, and G. V. Freymann, »Terahertz thickness determination with interferometric vibration correction for industrial applications«, *Opt. Express* **26**, 12558–12568 (2018).
- [124] D. Molter, K.-S. Ellenberger, J. Klier, S. Duran, J. Jonuscheit, G. v. Freymann, N. Vieweg, and A. Deninger, »Multilayer terahertz imaging at kilohertz pixel rate«, in *2022 47th international conference on infrared, millimeter and terahertz waves (irmmw-thz)* (2022), pp. 1–2.
- [125] T. B. Pittman, D. V. Strekalov, D. N. Klyshko, M. H. Rubin, A. V. Sergienko, and Y. H. Shih, »Two-photon geometric optics«, *Phys. Rev. A* **53**, 2804–2815 (1996).
- [126] N.-J. Jan, J. L. Grimm, H. Tran, K. L. Lathrop, G. Wollstein, R. A. Bilonick, H. Ishikawa, L. Kagemann, J. S. Schuman, and I. A. Sigal, »Polarization microscopy for characterizing fiber orientation of ocular tissues«, *Biomed. Opt. Express* **6**, 4705–4718 (2015).
- [127] A. Puthukkudy, J. V. Martins, L. A. Remer, X. G. Xu, O. Dubovik, P. Litvinov, B. McBride, S. Burton, and H. M. J. Barbosa, »Retrieval of aerosol properties from airborne hyper-angular rainbow polarimeter (airharp) observations during acepol 2017«, *Atmos. Meas. Tech.* **13**, 5207–5236 (2020).
- [128] M. Chekhova and P. Banzer, *Polarization of Light In Classical, Quantum, and Nonlinear Optics* (De Gruyter, Berlin, 2021).
- [129] A. Martinez, »Polarimetry enabled by nanophotonics«, *Science* **362**, 750–751 (2018).
- [130] N. A. Rubin, G. D’Aversa, P. Chevalier, Z. J. Shi, W. T. Chen, and F. Capasso, »Matrix Fourier optics enables a compact full-Stokes polarization camera«, *Science* **365**, eaax1839 (2019).
- [131] T. Stav, A. Faerman, E. Maguid, D. Oren, V. Kleiner, E. Hasman, and M. Segev, »Quantum entanglement of the spin and orbital angular momentum of photons using metamaterials«, *Science* **361**, 1101–1103 (2018).

- [132] P. Georgi, M. Massaro, K. H. Luo, B. Sain, N. Montaut, H. Herrmann, T. Weiss, G. X. Li, C. Silberhorn, and T. Zentgraf, »Metasurface interferometry toward quantum sensors«, *Light Sci. Appl.* **8**, 70 (2019).
- [133] C. Altuzarra, A. Lyons, G. H. Yuan, C. Simpson, T. Roger, J. S. Ben-Benjamin, and D. Faccio, »Imaging of polarization-sensitive metasurfaces with quantum entanglement«, *Phys. Rev. A* **99**, 020101 (2019).
- [134] A. S. Solntsev, G. S. Agarwal, and Y. S. Kivshar, »Metasurfaces for Quantum Photonics«, *Nat. Photon.* **15**, 327–336 (2021).
- [135] H. Kellock, T. Setälä, A. T. Friberg, and T. Shirai, »Polarimetry by classical ghost diffraction«, *J. Opt.* **16**, 055702 (2014).
- [136] A. Hännönen, A. T. Friberg, and T. Setälä, »Classical spectral ghost ellipsometry«, *Opt. Lett.* **41**, 4943–4946 (2016).
- [137] A. Hännönen, A. T. Friberg, and T. Setälä, »Classical ghost-imaging spectral ellipsometer«, *J. Opt. Soc. Am. A* **34**, 1360–1368 (2017).
- [138] P. Janassek, S. Blumenstein, and W. Elsasser, »Recovering a hidden polarization by ghost polarimetry«, *Opt. Lett.* **43**, 883–886 (2018).
- [139] D. F. Shi, J. M. Zhang, J. Huang, Y. J. Wang, K. Yuan, K. F. Cao, C. B. Xie, D. Liu, and W. Y. Zhu, »Polarization-multiplexing ghost imaging«, *Opt. Lasers Eng.* **102**, 100–105 (2018).
- [140] A. S. Chirkin, P. P. Gostev, D. P. Agapov, and S. A. Magnitskiy, »Ghost polarimetry: ghost imaging of polarization-sensitive objects«, *Laser Phys. Lett.* **15**, 115404 (2018).
- [141] A. Hännönen, B. J. Hoenders, W. Elsasser, A. T. Friberg, and T. Setälä, »Ghost polarimetry using Stokes correlations«, *J. Opt. Soc. Am. A* **37**, 714–719 (2020).
- [142] M. Roskopf, T. Mohr, and W. Elsasser, »Ghost polarization communication«, *Phys. Rev. Appl.* **13**, 034062 (2020).
- [143] S. Magnitskiy, D. Agapov, and A. Chirkin, »Ghost polarimetry with unpolarized pseudo-thermal light«, *Opt. Lett.* **45**, 3641–3644 (2020).
- [144] A. Valencia, G. Scarcelli, M. D’Angelo, and Y. Shih, »Two-photon imaging with thermal light«, *Phys. Rev. Lett.* **94**, 063601 (2005).
- [145] B. I. Erkmen and J. H. Shapiro, »Ghost imaging: from quantum to classical to computational«, *Adv. Opt. Photon.* **2**, 405–450 (2010).

- [146] H. C. Liu, B. A. Yang, Q. H. Guo, J. H. Shi, C. Y. Guan, G. X. Zheng, H. Muhlenbernd, G. X. Li, T. Zentgraf, and S. Zhang, »Single-pixel computational ghost imaging with helicity-dependent metasurface hologram«, *Sci. Adv.* **3**, e1701477 (2017).
- [147] G. B. Lemos, V. Borish, G. D. Cole, S. Ramelow, R. Lapkiewicz, and A. Zeilinger, »Quantum imaging with undetected photons«, *Nature* **512**, 409–U382 (2014).
- [148] M. Lahiri, R. Lapkiewicz, G. B. Lemos, and A. Zeilinger, »Theory of quantum imaging with undetected photons«, *Phys. Rev. A* **92**, 013832 (2015).
- [149] X. Y. Zou, L. J. Wang, and L. Mandel, »Induced coherence and indistinguishability in optical interference«, *Phys. Rev. Lett.* **67**, 318–321 (1991).
- [150] L. J. Wang, X. Y. Zou, and L. Mandel, »Induced coherence without induced emission«, *Phys. Rev. A* **44**, 4614–4622 (1991).
- [151] I. Kviatkovsky, H. M. Chrzanowski, E. G. Avery, H. Bartolomaeus, and S. Ramelow, »Microscopy with undetected photons in the mid-infrared«, *Science Advances* **6**, 10.1126/sciadv.abd0264 (2020).
- [152] M. Gilaberte Basset, A. Hochrainer, S. Töpfer, F. Rieinger, P. Bickert, J. R. León-Torres, F. Steinlechner, and M. Gräfe, »Video-rate imaging with undetected photons«, *Laser & Photonics Reviews* n/a, 2000327 (2021).
- [153] S. Töpfer, M. G. Basset, J. Fuenzalida, F. Steinlechner, J. P. Torres, and M. Gräfe, »Quantum holography with undetected light«, *Science Advances* **8**, eabl4301 (2022).
- [154] A. V. Paterova, S. M. Maniam, H. Yang, G. Grenci, and L. A. Krivitsky, »Hyperspectral infrared microscopy with visible light«, *Science Advances* **6**, eabd0460 (2020).
- [155] B. E. Haase, J. Hennig, M. Kutas, E. Waller, J. Hering, G. von Freymann, and D. Molter, »Phase-quadrature quantum imaging with undetected photons«, *Opt. Express* **31**, 143–152 (2023).
- [156] E. Abbe, »Beiträge zur theorie des mikroskops und der mikroskopischen wahrnehmung«, *Archiv für Mikroskopische Anatomie* **9**, 413–468 (1873).
- [157] L. Rayleigh, »Xxxi. investigations in optics, with special reference to the spectroscope«, *The London, Edinburgh, and Dublin Philosophical Magazine and Journal of Science* **8**, 261–274 (1879).
- [158] M. Born and E. Wolf, *Principles of Optics: Electromagnetic Theory of Propagation, Interference and Diffraction of Light*, 7th (Cambridge University Press, UK, 2020).

- [159] M. Knoll and E. Ruska, »Das elektronenmikroskop«, *Zeitschrift für Physik* **78**, 318–339 (1932).
- [160] M. D’Angelo, A. Valencia, M. H. Rubin, and Y. Shih, »Resolution of quantum and classical ghost imaging«, *Phys. Rev. A* **72**, 013810 (2005).
- [161] P.-A. Moreau, E. Toninelli, P. A. Morris, R. S. Aspden, T. Gregory, G. Spalding, R. W. Boyd, and M. J. Padgett, »Resolution limits of quantum ghost imaging«, *Opt. Express* **26**, 7528–7536 (2018).
- [162] P.-A. Moreau, P. A. Morris, E. Toninelli, T. Gregory, R. S. Aspden, G. Spalding, R. W. Boyd, and M. J. Padgett, »Experimental limits of ghost diffraction: popper’s thought experiment«, *Scientific Reports* **8**, 13183 (2018).
- [163] J. Fuenzalida, A. Hochrainer, G. B. Lemos, E. A. Ortega, R. Lapkiewicz, M. Lahiri, and A. Zeilinger, »Resolution of Quantum Imaging with Undetected Photons«, *Quantum* **6**, 646 (2022).
- [164] B. Viswanathan, G. B. Lemos, and M. Lahiri, »Resolution limit in quantum imaging with undetected photons using position correlations«, *Opt. Express* **29**, 38185–38198 (2021).
- [165] I. Kviatkovsky, H. M. Chrzanowski, and S. Ramelow, »Mid-infrared microscopy via position correlations of undetected photons«, *Opt. Express* **30**, 5916–5925 (2022).
- [166] C. H. Monken, P. H. S. Ribeiro, and S. Pádua, »Transfer of angular spectrum and image formation in spontaneous parametric down-conversion«, *Phys. Rev. A* **57**, 3123–3126 (1998).
- [167] J. Schneeloch and J. C. Howell, »Introduction to the transverse spatial correlations in spontaneous parametric down-conversion through the biphoton birth zone«, *Journal of Optics* **18**, 053501 (2016).
- [168] K. Y. Spasibko, T. S. Iskhakov, and M. V. Chekhova, »Spectral properties of high-gain parametric down-conversion«, *Opt. Express* **20**, 7507–7515 (2012).
- [169] P. R. Sharapova, G. Frascella, M. Riabinin, A. M. Pérez, O. V. Tikhonova, S. Lemieux, R. W. Boyd, G. Leuchs, and M. V. Chekhova, »Properties of bright squeezed vacuum at increasing brightness«, *Phys. Rev. Research* **2**, 013371 (2020).
- [170] M. Tsang, »Relationship between resolution enhancement and multiphoton absorption rate in quantum lithography«, *Phys. Rev. A* **75**, 043813 (2007).
- [171] S. Saravi, A. N. Poddubny, T. Pertsch, F. Setzpfandt, and A. A. Sukhorukov, »Atom-mediated spontaneous parametric down-conversion in periodic waveguides«, *Opt. Lett.* **42**, 4724–4727 (2017).

- [172] E. A. Santos, T. Pertsch, F. Setzpfandt, and S. Saravi, »Subdiffraction quantum imaging with undetected photons«, *Phys. Rev. Lett.* **128**, 173601 (2022).
- [173] A. V. Burlakov, M. V. Chekhova, D. N. Klyshko, S. P. Kulik, A. N. Penin, Y. H. Shih, and D. V. Strekalov, »Interference effects in spontaneous two-photon parametric scattering from two macroscopic regions«, *Phys. Rev. A* **56**, 3214–3225 (1997).
- [174] R. Butkus, S. Orlov, A. Piskarskas, V. Smilgevicius, and A. Stabinis, »Phase matching of optical x-waves in nonlinear crystals«, *Optics Communications* **244**, 411–421 (2005).
- [175] O. Jedrkiewicz, M. Clerici, A. Picozzi, D. Faccio, and P. Di Trapani, »X-shaped space-time coherence in optical parametric generation«, *Phys. Rev. A* **76**, 033823 (2007).
- [176] K. Y. Spasibko, D. A. Kopylov, T. V. Murzina, G. Leuchs, and M. V. Chekhova, »Ring-shaped spectra of parametric downconversion and entangled photons that never meet«, *Opt. Lett.* **41**, 2827–2830 (2016).
- [177] B.-S. Shi and A. Tomita, »Generation of a pulsed polarization entangled photon pair using a sagnac interferometer«, *Phys. Rev. A* **69**, 013803 (2004).
- [178] T. Kim, M. Fiorentino, and F. N. C. Wong, »Phase-stable source of polarization-entangled photons using a polarization sagnac interferometer«, *Phys. Rev. A* **73**, 012316 (2006).
- [179] M. A. Nielsen and I. L. Chuang, *Quantum computation and quantum information: 10th anniversary edition* (Cambridge University Press, 2010).
- [181] M. V. Chekhova and Z. Y. Ou, »Nonlinear interferometers in quantum optics«, *Adv. Opt. Photon.* **8**, 104–155 (2016).
- [182] B. Viswanathan, G. B. Lemos, and M. Lahiri, »Position correlation enabled quantum imaging with undetected photons«, *Opt. Lett.* **46**, 3496–3499 (2021).
- [183] M. Lahiri, A. Hochrainer, R. Lapkiewicz, G. B. Lemos, and A. Zeilinger, »Twin-photon correlations in single-photon interference«, *Phys. Rev. A* **96**, 013822 (2017).
- [184] R. Loudon, *The quantum theory of light*, Third (Clarendon Press, Oxford, 2000).
- [185] R. J. Glauber, »The quantum theory of optical coherence«, *Phys. Rev.* **130**, 2529–2539 (1963).
- [186] F. Just, A. Cavanna, M. V. Chekhova, and G. Leuchs, »Transverse entanglement of biphotons«, *New Journal of Physics* **15**, 083015 (2013).
- [187] K. S. Rogers, K. N. Bourdakos, G. H. Yuan, S. Mahajan, and E. T. F. Rogers, »Optimising superoscillatory spots for far-field super-resolution imaging«, *Opt. Express* **26**, 8095–8112 (2018).

- [188] G. Chen, Z.-Q. Wen, and C.-W. Qiu, »Superoscillation: from physics to optical applications«, *Light: Science & Applications* **8**, 56 (2019).
- [189] K. W. Chan, J. P. Torres, and J. H. Eberly, »Transverse entanglement migration in hilbert space«, *Phys. Rev. A* **75**, 050101 (2007).
- [191] Z. Li, N. Medvedev, H. N. Chapman, and Y. Shih, »Radiation damage free ghost diffraction with atomic resolution«, *Journal of Physics B: Atomic, Molecular and Optical Physics* **51**, 025503 (2017).
- [192] Y. Cai and S.-Y. Zhu, »Ghost imaging with incoherent and partially coherent light radiation«, *Phys. Rev. E* **71**, 056607 (2005).
- [193] D.-Z. Cao, J. Xiong, and K. Wang, »Geometrical optics in correlated imaging systems«, *Phys. Rev. A* **71**, 013801 (2005).
- [194] A. Gatti, E. Brambilla, M. Bache, and L. A. Lugiato, »Correlated imaging, quantum and classical«, *Phys. Rev. A* **70**, 013802 (2004).
- [195] A. C. Cardoso, L. P. Berruezo, D. F. Ávila, G. B. Lemos, W. M. Pimenta, C. H. Monken, P. L. Saldanha, and S. Pádua, »Classical imaging with undetected light«, *Phys. Rev. A* **97**, 033827 (2018).
- [197] M. Young, »Pinhole optics«, *Appl. Opt.* **10**, 2763–2767 (1971).
- [198] M. Young, »The pinhole camera: imaging without lenses or mirrors«, *The Physics Teacher* **27**, 648–655 (1989).
- [199] C. Thomas, G. Rehm, I. Martin, and R. Bartolini, »X-ray pinhole camera resolution and emittance measurement«, *Phys. Rev. ST Accel. Beams* **13**, 022805 (2010).
- [200] H. O. Anger, »Use of a gamma-ray pinhole camera for in vivo studies«, *Nature* **170**, 200–201 (1952).
- [201] B. Haase, M. Kutas, F. Riexinger, P. Bickert, A. Keil, D. Molter, M. Bortz, and G. von Freymann, »Spontaneous parametric down-conversion of photons at 660 nm to the terahertz and sub-terahertz frequency range«, *Opt. Express* **27**, 7458–7468 (2019).
- [202] P. Xu, H. Y. Leng, Z. H. Zhu, Y. F. Bai, H. Jin, Y. X. Gong, X. Q. Yu, Z. D. Xie, S. Y. Mu, and S. N. Zhu, »Lensless imaging by entangled photons from quadratic nonlinear photonic crystals«, *Phys. Rev. A* **86**, 013805 (2012).
- [203] G. Scarcelli, V. Berardi, and Y. Shih, »Phase-conjugate mirror via two-photon thermal light imaging«, *Applied Physics Letters* **88**, 061106 (2006).

- [204] X.-H. Chen, Q. Liu, K.-H. Luo, and L.-A. Wu, »Lensless ghost imaging with true thermal light«, *Opt. Lett.* **34**, 695–697 (2009).
- [205] W. Gong, P. Zhang, X. Shen, and S. Han, »Ghost “pinhole” imaging in fraunhofer region«, *Applied Physics Letters* **95**, 071110 (2009).
- [206] A. F. Abouraddy, B. E. A. Saleh, A. V. Sergienko, and M. C. Teich, »Entangled-photon fourier optics«, *J. Opt. Soc. Am. B* **19**, 1174–1184 (2002).
- [207] A. Zee, *Quantum field theory in a nutshell*, 2nd, Appendix A (Princeton University Press, 2010).
- [211] N. A. Peters, J. T. Barreiro, M. E. Goggin, T. C. Wei, and P. G. Kwiat, »Remote state preparation: arbitrary remote control of photon polarization«, *Phys. Rev. Lett.* **94**, 150502 (2005).
- [212] A. Zavatta, M. D’Angelo, V. Parigi, and M. Bellini, »Remote preparation of arbitrary time-encoded single-photon ebits«, *Phys. Rev. Lett.* **96**, 020502 (2006).
- [213] W. K. Wootters, »Entanglement of formation of an arbitrary state of two qubits«, *Phys. Rev. Lett.* **80**, 2245–2248 (1998).
- [214] A. Z. Goldberg, P. De La Hoz, G. Bjork, A. B. Klimov, M. Grassl, G. Leuchs, and L. L. Sanchez-Soro, »Quantum concepts in optical polarization«, *Adv. Opt. Photon.* **13**, 1–73 (2021).
- [215] S. Lung, K. Wang, K. Z. Kamali, J. H. Zhang, M. Rahmani, D. N. Neshev, and A. A. Sukhorukov, »Complex-birefringent dielectric metasurfaces for arbitrary polarization-pair transformations«, *ACS Photonics* **7**, 3015–3022 (2020).
- [216] P. A. Moreau, E. Toninelli, T. Gregory, and M. J. Padgett, »Imaging with quantum states of light«, *Nat. Rev. Phys.* **1**, 367–380 (2019).
- [217] M. Malik, H. Shin, M. O’Sullivan, P. Zerom, and R. W. Boyd, »Quantum ghost image identification with correlated photon pairs«, *Phys. Rev. Lett.* **104**, 163602 (2010).
- [220] J. H. Shapiro, D. Venkatraman, and F. N. C. Wong, »Classical imaging with undetected photons«, *Sci. Rep.* **5**, 10329 (2015).
- [221] W. Zhang, R. Fickler, E. Giese, L. Chen, and R. W. Boyd, »Influence of pump coherence on the generation of position-momentum entanglement in optical parametric down-conversion«, *Opt. Express* **27**, 20745–20753 (2019).
- [222] L. Hutter, G. Lima, and S. P. Walborn, »Boosting entanglement generation in down-conversion with incoherent illumination«, *Phys. Rev. Lett.* **125**, 193602 (2020).

A References

- [223] J. F. deBoer, T. E. Milner, M. J. C. vanGemert, and J. S. Nelson,
»Two-dimensional birefringence imaging in biological tissue by
polarization-sensitive optical coherence tomography«, *Opt. Lett.* **22**, 934–936
(1997).
- [224] V. V. Tuchin, L. V. Wang, and D. A. Zimnyakov,
Optical polarization in biomedical applications (Springer, Berlin, 2006).
- [225] P. Scott, X. Garcia-Santiago, D. Beutel, C. Rockstuhl, M. Wegener, and
I. Fernandez-Corbaton,
»On enhanced sensing of chiral molecules in optical cavities«,
April 7, 041413 (2020).
- [226] D. Bhatti, J. von Zanthier, and G. S. Agarwal,
»Entanglement of polarization and orbital angular momentum«,
Phys. Rev. A **91**, 062303 (2015).
- [227] C. U. Hail, A. K. U. Michel, D. Poulidakos, and H. Eghlidi,
»Optical metasurfaces: evolving from passive to adaptive«,
Adv. Opt. Mater. **7**, 1801786 (2019).
- [228] M. Krenn, J. Landgraf, T. Foesel, and F. Marquardt,
»Artificial intelligence and machine learning for quantum technologies«,
Phys. Rev. A **107**, 010101 (2023).

B. List of own contributions

Published articles

- [82] M. Kumar, P. Kumar, A. Vega, M. A. Weissflog, T. Pertsch, and F. Setzpfandt, »Mid-infrared photon pair generation in aggas2«, *Applied Physics Letters* **119**, 244001 (2021).
- [180] A. Vega, E. A. Santos, J. Fuenzalida, M. Gilaberte Basset, T. Pertsch, M. Gräfe, S. Saravi, and F. Setzpfandt, »Fundamental resolution limit of quantum imaging with undetected photons«, *Phys. Rev. Research* **4**, 033252 (2022).
- [210] A. Vega, S. Saravi, T. Pertsch, and F. Setzpfandt, »Pinhole quantum ghost imaging«, *Applied Physics Letters* **117**, 094003 (2020).
- [219] A. Vega, T. Pertsch, F. Setzpfandt, and A. A. Sukhorukov, »Metasurface-assisted quantum ghost discrimination of polarization objects«, *Phys. Rev. Applied* **16**, 064032 (2021).

Preprint

- [113] V. F. Gili, D. Dupish, A. Vega, M. Gandola, E. Manuzzato, M. Perenzoni, L. Gasparini, T. Pertsch, and F. Setzpfandt, »Sub-minute quantum ghost imaging in the infrared enabled by a "looking back" spad array«, [10.48550/ARXIV.2211.12913](https://arxiv.org/abs/10.48550/ARXIV.2211.12913) (2022).

Article in preparation

- [229] M. G. Basset, J. Fuenzalida, A. Vega, E. A. Santos, S. Saravi, F. Setzpfandt, and M. Gräfe, »Resolution of quantum imaging through position correlations with long crystals«, (2023).

Conference presentations/posters

- [190] E. Santos, S. Saravi, A. Vega, T. Pertsch, and F. Setzpfandt, »Sub-diffraction near-field imaging with undetected photons using thin sources of photon pairs«, in 2021 conference on lasers and electro-optics europe and european quantum electronics conference (2021), eb_p_7.

B List of own contributions

- [196] A. Vega, E. Santos, J. Fuenzalida, M. G. Basset, T. Pertsch, M. Gräfe, S. Saravi, and F. Setzpfandt, »Resolution of two-color quantum imaging with undetected photons«, in Quantum information and measurement vi 2021 (2021), Th4A.4.
- [208] A. Vega, E. Santos, S. Saravi, T. Pertsch, and F. Setzpfandt, »The role of detector position in quantum ghost diffraction«, in 2019 conference on lasers and electro-optics europe and european quantum electronics conference (2019), ea_p_18.
- [209] A. Vega, S. Saravi, T. Pertsch, and F. Setzpfandt, »Incoherence and lens-less imaging in quantum ghost diffraction«, in Quantum information and measurement (qim) v: quantum technologies (2019), T5A.64.
- [218] A. Vega, K. Wang, S. Lung, D. E. Jones, M. Brodsky, T. Pertsch, F. Setzpfandt, and A. A. Sukhorukov, »Discerning polarization objects using non-local measurements with metasurfaces«, in Conference on lasers and electro-optics (2020), FM1C.7.

C. List of abbreviations

AgGaS ₂	silver gallium sulfide
BBO	beta barium borate
CCD	charge coupled device
JSP	joint spatial probability
KDP	potassium dihydrogen phosphate
KTP	potassium titanyl phosphate
LiNbO ₃	lithium niobate
NA	numerical aperture
QGD	quantum ghost diffraction
QGI	quantum ghost imaging
QGP	quantum ghost polarimetry
QIUP	quantum imaging with undetected photons
SNR	signal-to-noise ratio
SPAD	single-photon avalanche diode
SPDC	spontaneous parametric down-conversion

D. Acknowledgement

I am very grateful to Prof. Thomas Pertsch and Dr. Frank Setzpfandt for the golden opportunity to pursue my doctoral studies in their group. Frank supervised my work from the beginning and I always admired his openness to discussions. I have learned a lot from him throughout these years and his unconditional support has played a vital role in the results presented in this thesis.

Since my work was mostly theoretical, my go-to expert for discussing any difficult matter I was struggling to understand was Dr. Sina Saravi. I am very grateful to Sina for all the valuable hours of discussion that we had in these years that contributed significantly to my work.

I was very fortunate to collaborate with Prof. Andrey Sukhorukov in the work regarding quantum ghost polarimetry. In particular, the short visit I made to his group in Australia was an eye-opener to see my work from a different and broader perspective.

Thanks to the experimental work carried out by Prof. Markus Gräfe, Jorge Fuenzalida, and Marta Gilaberte Basset of Fraunhofer IOF, literally in the building in front of my office, I got interested in investigating quantum imaging with undetected photons. I am grateful for all the numerous discussions we had and cherish the friendship that arose from this collaboration.

The PhD years have been deeply rewarding, not only for the research achievements, but also for the work along my colleagues: Dennis, Mina, Jan, Pawan, Najmeh, Anna, Reza, Franz, Max, Luosha, Tobias, Aleksa, Vira, Masoud, Omid, Katsuya, Thomas K., and Daniel R. But in particular, I am grateful to my office colleagues:

- Elkin Santos for the countless hours discussing about the work of ‘el abuelito’ and also for being the cofounder of the pop-rock band ‘Slice of Pi’.
- Mohit(o) Kumar for the always deep and entertaining ‘ghost’- and biryani-related conversations.
- Valerio Gili and Dupish for fun lab work with the SPAD array for the quantum ghost setup. We were lucky to have continued technical support from Daniel Füssel.

Last but definitely not least, I am deeply grateful to the love of my life Serena, who lights up my days with her smile, and to my loving and supportive family, Esther, Hernan, and Mauricio, who despite the distance have been by my side.

Gracias... totales

E. Zusammenfassung

Verschränkte Photonenpaare, gemeinhin als Signal- und Idler-Photonen bezeichnet, wurden als Grundlage für Quantum imaging with undetected photons (QIUP) und Quantum ghost imaging (QGI) verwendet. Mit QIUP können wir ein Objekt abbilden, indem wir nur die Signal-Photonen messen, die nie mit dem Objekt wechselwirken, während die Idler-Photonen, die das Objekt beleuchten, undetektiert bleiben. Bei QGI werden die beleuchtenden Idler-Photonen von einem räumlich nicht auflösenden Detektor gemessen, während die nicht wechselwirkenden Signal-Photonen von einer Kamera gemessen werden und das Bild dann nur aus den Koinzidenzen von Signal und Idler rekonstruiert wird. Nennenswert ist hier die Verwendung von zweifarbigem Photonenpaaren, welche es uns ermöglichen, Komplikationen bei der Bildgebung in Wellenlängenbereichen zu überwinden, in denen Kameras nur eine geringe Effizienz aufweisen. Daraus ergibt sich ein enormes Potenzial für die Biosensorik, bei der empfindliche Proben, die für Strahlungsschäden anfällig sind, mit herkömmlichen Einzelphotonen-Kameras abgebildet werden können, wie zum Beispiel im sichtbaren Spektralbereich, während die Probe von Photonen mit viel geringerer Energie beleuchtet wird.

In dieser Arbeit wurden drei Lücken in der Literatur zur Quantenbildgebung und Polarimetrie geschlossen:

1. Die transversale Auflösungsgrenze von QIUP und QGI, die zweifarbigem Photonenpaare verwenden, wurde diskutiert. Wir haben eine nicht-paraxiale Beschreibung der Erzeugung von Photonenpaaren hergeleitet, die als Grundlage für die Feststellung diente, dass die fundamentale Auflösung, basierend auf dem Rayleigh-Kriterium, durch die größere Wellenlänge des Photonenpaares begrenzt ist.
2. Ein linsenloses QGI-Verfahren wurde vorgestellt, das sich speziell für die Abbildung in Wellenlängenbereichen eignet, für die weniger Linsen zur Verfügung stehen, wie zum Beispiel im Terahertz-Bereich. Wir haben es Pinhole QGI genannt, da wir gezeigt haben, dass es analog zur klassischen Lochkamera ist.
3. Ein Quantum ghost polarimetry (QGP) Schema wurde vorgeschlagen, bei dem dielektrische Metaoberflächen verwendet werden können, um den Einsatz rekonfigurierbarer optischer Elemente zu vermeiden. QGP kann verwendet werden, um empfindliche Proben mit ausgeprägten doppelbrechenden und chiralen Eigenschaften zu messen. Wir haben das Potenzial von QGP anhand eines Beispiels für die Unterscheidung polarisationsempfindlicher Objekte aufgezeigt.

F. Ehrenwörtliche Erklärung

Ich erkläre hiermit ehrenwörtlich, dass ich die vorliegende Arbeit selbständig, ohne unzulässige Hilfe Dritter und ohne Benutzung anderer als der angegebenen Hilfsmittel und Literatur angefertigt habe. Die aus anderen Quellen direkt oder indirekt übernommenen Daten und Konzepte sind unter Angabe der Quelle gekennzeichnet.

Bei der Auswahl und Auswertung folgenden Materials haben mir die nachstehend aufgeführten Personen in der jeweils beschriebenen Weise unentgeltlich geholfen:

1. Die nicht-paraxiale Herleitung des Zwei-Photonen-Zustands wurde von Elkin A. Santos durchgeführt.

2. Die Initiative zur Verwendung von Metaoberflächen in der nichtlokalen Polarimetrie ging von Prof. Andrey Sukhorukov aus.

3. Die Experimente zu Quantum imaging with undetected photons von Marta Gilaberte Basset und Jorge Fuenzalida aus der Gruppe von Prof. Markus Gräfe (Fraunhofer IOF & TU Darmstadt) inspirierten unsere Arbeit bezüglich der fundamentalen Auflösungsgrenze dieses Schemas.

Weitere Personen waren an der inhaltlich-materiellen Erstellung der vorliegenden Arbeit nicht beteiligt. Insbesondere habe ich hierfür nicht die entgeltliche Hilfe von Vermittlungs- bzw. Beratungsdiensten (Promotionsberater oder andere Personen) in Anspruch genommen. Niemand hat von mir unmittelbar oder mittelbar geldwerte Leistungen für Arbeiten erhalten, die im Zusammenhang mit dem Inhalt der vorgelegten Dissertation stehen.

Die Arbeit wurde bisher weder im In- noch im Ausland in gleicher oder ähnlicher Form einer anderen Prüfungsbehörde vorgelegt.

Die geltende Promotionsordnung der Physikalisch-Astronomischen Fakultät ist mir bekannt.

Ich versichere ehrenwörtlich, dass ich nach bestem Wissen die reine Wahrheit gesagt und nichts verschwiegen habe.

Ort, Datum

Unterschrift d. Verfassers